AN EXPERIMENTAL INVESTIGATION OF TRANSONIC FLOW PAST TWO-DIMENSIONAL WEDGE AND CIRCULAR ARC SECTIONS USING A MACH-ZEHNDER INTERFEROMETER

Thesis by

Arthur Earl Bryson Jr.

In Partial Fulfillment of the Requirements

For the Degree of

Doctor of Philosophy

California Institute of Technology

Pasadena, California

1951

ACKNOWLEDGEMENTS

The author wishes to express his sincere thanks to Dr. Hans Wolfgang Liepmann for his valuable advice on this research and for his contagious enthusiasm which made the work most stimulating and enjoyable. The assistance of Harry Ashkenas, Satish Dhawan, George Solomon, and other members of the GALCIT Transonic Research Group in carrying out the tests and through valuable discussions was also very much appreciated. The author wishes to thank Mrs. Beverley Cottingham in particular for the excellent drawings contained herein and for the typing of the manuscript. He would like to thank Mr. William Sublette for his extremely skillful machining of the very small models used in these tests. He would also like to thank Mr. Walter G. Vincenti of the NACA Ames Laboratory and Dr. Julian D. Cole of GALCIT for making available to him the results of their theoretical investigations of transonic flow past wedge sections. Finally he would like to thank the California Institute of Technology and the Hughes Aircraft Company for financial assistance without which his studies here would have been impossible.

SUMMARY

Interferometer measurements are given of the flow fields near two-dimensional wedge and circular arc sections at zero angle of attack at high subsonic and low supersonic velocities. Both subsonic flow with local supersonic zone and supersonic flow with detached shock wave have been investigated. Pressure distributions and drag coefficients as functions of Mach number have been obtained. The wedge data are compared with the theoretical work on flow past wedge sections of Guderley and Yoshihara, Vincenti and Wagoner, and Cole.

It is shown that the local Mach number at any point on the surface of a finite three-dimensional body or an unswept two-dimensional body, moving through an infinite fluid, has a stationary value at Mach number one and, in fact, remains nearly constant for a range of speeds below and above Mach number one. On the basis of this concept and the experimental data, pressure distributions and drag coefficients for the wedge and circular arc sections are presented throughout the entire transonic range of velocities.

TABLE OF CONTENTS

Acknowledgements i

Summary ii

Table of Contents iii

Table of Figures vii

Symbols ix

I. Introduction 1

1. Difficulties of Theory and Experiment in the Transonic Range of Velocities 1

2. Existence of Potential Transonic Flows 2

3. Choice of Models 4

4. Transonic Theory and Experiments 5

II. Apparatus and Methods 7

1. Wind Tunnel 7

2. Models 7

3. Interferometer 8

4. Method of Evaluation of Interferograms 9

5. Interferometer Sensitivity 11

6. Side Wall Boundary Layer Effect on Approximating Two-Dimensional Flow 13

7. Side Wall Boundary Layer Effect on Interferogram Evaluations 14

8. Determination of Free Stream Mach Number 15

9. Wind Tunnel Choking 16

10. Reynolds Number 17

III. Theoretical Work on Transonic Flow 18

1. Relaxation Calculations 18

2. Transonic Perturbation Theory 20

3. Theoretical Studies of Transonic Flow Past Thin Wedge Sections 21

IV. Characteristic Features of Transonic Flow Past Wedge and Circular Arc Sections 26

1. Characteristic Free Stream Mach Numbers 26

2. Characteristic Values of the Local Mach Number 28

V. Pressure Distributions on Bodies Moving Through an Infinite Fluid at Speeds Near Mach Number One 30

1. Stationary Value of Local Mach Number at Free Stream Mach Number One 30

2. Slope of the Pressure and Drag Coefficient Curves at $M_\infty = 1$ 33

3. Slope of the Drag Coefficient Curve at $M_\infty = 1$ in Transonic Similarity Parameters 35

4. Other Data Showing the Slow Variation of Local Mach Number Near $M_\infty = 1$ 36

VI. On Comparing Theory and Experiment 38

VII. Experimental Results 40

1. Flow Field Near the 10° Wedge 40

2. Local Mach Number Distributions on the Three Thin Wedges 42

3. Pressure Coefficient Distributions on the Three Thin Wedges 42

4. Shock Detachment Distances for the Three Thin Wedges 43

5. Drag Coefficient Variation with Mach Number for the Three Thin Wedges 43

6. Flow Field for the 26.6° Wedge at $M_\infty = 1.44$ 45

7. Flow Field Near the 8.8% Circular Arc Section 45

8. Local Mach Number Distributions on the 8.8% Circular Arc Section 46

9. Pressure Coefficient Distributions on the 8.8% Circular Arc Section 47

10. Drag Coefficient Variation with Mach Number for the 8.8% Circular Arc Section 47

11. Local Mach Number Distributions on a 12% Biconvex Circular Arc Airfoil 48

12. Drag Coefficient Variation with Mach Number for a 12% Biconvex Circular Arc Airfoil 49

VIII. Conclusions 50

References 52

Appendices

1. Asymptotic Representation of Cole's Solution for Large Negative Values of Reduced Free Stream Mach Number 55

2. Linearized Subsonic and Supersonic Flow Past Wedge and Circular Arc Sections 59

3. Transonic Shock Polar 63

4. Variation of Reduced Mach Number at which Sonic Velocity Occurs Behind an Oblique Shock with Flow Deflection Angle 65

5. Variation of Reduced Mach Number Behind a Prandtl-Meyer Expansion from M = 1 Through an Angle θ, with θ 67

TABLE OF FIGURES

1. Geometry of Sections Tested

2. Typical Finite Fringe Interferogram

3. Typical Superimposed Finite Fringe Interferogram

4. Increment in Mach Number Per Fringe Contour Versus Local Mach Number for Air ($\gamma = 1.4$)

5. Theoretical Reduced Local Mach Number Distributions on a Wedge Near Mach Number One

6. Theoretical Reduced Local Mach Number Versus Reduced Free Stream Mach Number at Several Chordwise Stations on a Wedge

7. Theoretical Reduced Pressure Coefficient Distributions on a Wedge Near Mach Number One

8. Theoretical Reduced Drag Coefficient Versus Reduced Mach Number for a Wedge

9. through 15. Interferograms of the 10° Semi-Angle Wedge at Subsonic and Supersonic Speeds

16. Local Mach Number Versus x/c for Increasing Free Stream Mach Number - 10° Semi-Angle Wedge

17. Local Mach Number Versus x/c for Increasing Free Stream Mach Number - $7\ 1/2^{\circ}$ Semi-Angle Wedge

18. Local Mach Number Versus x/c for Increasing Free Stream Mach Number - $4\ 1/2^{\circ}$ Semi-Angle Wedge

19. Pressure Distributions - $7\ 1/2^{\circ}$ Semi-Angle Wedge - Subsonic

20. Pressure Distributions - $7\ 1/2^{\circ}$ Semi-Angle Wedge - Supersonic

21. Shock Detachment Distance Versus Reduced Mach Number for a Wedge

22. Experimental Reduced Drag Coefficient Versus Reduced Mach Number on a Wedge

23. Drag Coefficient Versus Mach Number for 4 1/2°, 7 1/2°, 10° Semi-Angle Wedges - Comparison of Theory with Experiment

24. Constant Mach Number Contours on the 26.6° Semi-Angle Wedge at $M_\infty = 1.44$ - Theoretical and Experimental

25. Pressure Distribution on a 26.6° Semi-Angle Wedge at $M_\infty = 1.44$ - Theoretical and Experimental

26. through 32. Interferograms of the 8.8% Circular Arc Section at Subsonic and Supersonic Speeds

33. Local Mach Number Versus x/c for Increasing Free Stream Mach Number - 8.8% Circular Arc Section

34. Reduced Local Mach Number Distributions - Variation with Reduced Free Stream Mach Number - 8.8% Circular Arc Section

35. Pressure Distributions on an 8.8% Circular Arc Section - Subsonic

36. Pressure Distributions on an 8.8% Circular Arc Section - Supersonic

37. Drag Coefficient Versus Mach Number for 8.8% Circular Arc Section

38. Local Mach Number Versus x/c for Increasing Free Stream Mach Number - 12% Biconvex Circular Arc Airfoil

39. Drag Coefficient Versus Mach Number for 12% Biconvex Circular Arc Airfoil

SYMBOLS

a	sound velocity
c	airfoil chord
C_D	pressure drag coefficient
$\tilde{C}_D$	reduced drag coefficient = $\frac{(\gamma+1)^{1/3} C_D}{(t/c)^{5/3}}$
C_p	pressure coefficient
$\tilde{C}_p$	reduced pressure coefficient = $\frac{(\gamma+1)^{1/3} C_p}{(t/c)^{2/3}}$
k	Gladstone-Dale constant
ℓ	model span
M	Mach number
n	index of refraction
p	pressure
q	dynamic pressure
t/c	airfoil thickness ratio
u	horizontal component perturbation velocity (perturbation from a^*)
v	vertical component perturbation velocity
x, y	Cartesian coordinates, origin at leading edge of profile
$\tilde{y}$	reduced vertical distance = $[(\gamma+1)\ t/c]^{1/3}\ y$
α	angle of attack
γ	ratio of specific heats (1.4 for air)
θ	semi-wedge angle
λ	wave length of monochromatic light used on interferometer
ξ	reduced Mach number
ρ	density

SYMBOLS (continued)

Subscripts and Superscripts

$( )_\infty$ conditions in free stream

$( )_o$ reservoir conditions

$( )_o'$ reservoir conditions behind a shock wave

$( )^*$ conditions at sonic velocity

$( )$ without subscript - local conditions

I. INTRODUCTION*

1. Difficulties of Theory and Experiment in the Transonic Range of Velocities

The difficulties inherent in studying transonic flow are well known. Theoretical analysis is made difficult by the non-linearity of the differential equations of compressible fluid motion. This non-linearity leads to a change-over in type of the differential equations from elliptic to hyperbolic when transition is made from subsonic to supersonic speeds. Since the essential feature of transonic flow is this mixed subsonic-supersonic character, it is obvious that no linearization of the differential equations (at least in the physical plane) can adequately describe the flow.

Wind tunnel studies in the transonic range are made difficult by the large lateral extent of the perturbation flow field around bodies in this range. This means that models which are small compared to the test section must be used. Even then there is still a range of speeds from just below $M_\infty = 1$ to just above $M_\infty = 1$ where the model and/or its support configuration are "choked," that is, where local supersonic zones embedded in the subsonic field extend from the model to the tunnel walls, or, in the supersonic case, where embedded subsonic zones extend to the tunnel walls, or shock waves, reflected from the walls, impinge on the model. Some progress has been made recently in modifying wind tunnel test sections so as to

*Some of the results of these experiments have already been reported in Ref. 1.

minimize these effects, but, on the whole, the majority of good test data in the range very close to $M_\infty = 1$ has so far come from free flight tests. Some good transonic data are available, however, from transonic bump tests made in wind tunnels (Ref. 2). Using small models usually results in low Reynolds numbers so that difficulty is often experienced in extrapolating data to full size Reynolds numbers; this seems to be particularly true of the transonic speed range since the effects of boundary layer - shock wave interactions seem to be quite large there (Refs. 3 and 4).

In this paper it is shown that in many instances tests need not be made in the region very close to $M_\infty = 1$ since the flow in this range can be inferred from testing below and above this range and using an interpolation based on the fact that the local Mach number at any point on the surface of unswept two-dimensional bodies and finite three-dimensional bodies has a stationary value at $M_\infty = 1$.

2. Existence of Potential Transonic Flows

G. Guderley has made a detailed investigation of the possibility of smooth transonic flows (that is, subsonic flows with an embedded supersonic zone in which no shock waves appear) (Ref. 5). He proposes that such smooth flows are exceptional, that they are discrete cases occurring for only particular body shapes at particular free stream Mach numbers. Any perturbation of the shape with the Mach number held constant (or vice versa), Guderley claims, would result in a shock appearing in the flow. This bears an analogy to the well known Busemann supersonic biplane which theoretically has no shocks

(and hence no drag) at a discrete value of free stream Mach number and angle of attack (Ref. 6, p. 154). Guderley's proposal is still controversial (for example, see the paper of W. R. Sears who has made a critical survey of the work to date on the existence of transonic potential flows (Ref. 7)).

It is obvious that the potential flow must break down for a given body shape at some Mach number less than one. The argument whether this breakdown occurs precisely when a supersonic region first appears on the body or at a slightly higher Mach number seems somewhat academic, (although very interesting) since it is well known experimentally that the drag rise Mach number (that is, the Mach number where noticeable shocks first appear) is very close to the critical Mach number (that is, the Mach number when sonic velocity first appears on the body) for most bodies without surface slope discontinuities.

Kuo (Ref. 8) proposes that supersonic compression is unstable to disturbances, that is, a supersonic region on a body in subsonic flow must end in a shock with no compression occurring in the supersonic flow ahead of the shock. There seems to be ample experimental evidence to show that this is not strictly true since, for example, the compression region of a λ -shock is clearly supersonic. However, the λ-shock configuration is believed to be a phenomenon associated with laminar boundary layer - shock wave interaction; with turbulent boundary layer (a condition more closely approaching non-viscous flow) hardly any noticeable supersonic compression occurs before the shock ending the supersonic zone (see Ref. 9).

3. Choice of Models

Two-dimensional flow is much simpler to handle than axially symmetric flow both in theoretical work and in interferometry. Hence it was decided to study two-dimensional flows despite the well known difficulties in approximating two-dimensional flow in a wind tunnel.

Due to the considerations mentioned previously it was decided to test very small models which would be of such a shape that viscous influences would not materially affect the flow over them. This led to the choice of half airfoils, wedges and circular arc sections followed by straight sections. These models have favorable pressure gradients on their surfaces over most of the transonic range so that boundary layer separation, if it does occur, will only occur due to shock wave influence. Furthermore, such separation will occur downstream of the part of the body being studied and hence will not affect the measurements. Certain viscous effects will still be evident however, for instance, the effective rounding off of the shoulders and leading edges of the wedge models.

Both theoretical advantages and practical need make the study of thin sections desirable. Consequently the semi-wedge angles chosen were 4 1/2°, 7 1/2°, and 10° (a 26.6° wedge was also used in order to make a comparison with some available theoretical work on a wedge of this angle). The circular arc section chosen was essentially the front half of an 8.8% thick biconvex circular arc airfoil, followed by a straight section. Models of sections much thinner than this, with the same chord lengths used, run into structural difficulties and also the ratio of boundary layer thickness to model thickness

becomes large enough to cause considerable deviation from non-viscous flow.

4. Transonic Flow Theory and Experiments

The investigations of von Kármán, Busemann, Guderley, Frankl, and many others have contributed significantly to methods of approach which can be used to study transonic flow (Refs. 10-15). The detailed numerical calculations for specific cases made by Maccoll and Codd, Emmons, Drougge, Drebinger, Guderley and Yoshihara, and Vincenti and Wagoner (Refs. 16-22) have helped to dispel the idea of a "sonic barrier." Recently J. D. Cole at GALCIT has given an analysis of the flow past wedge sections at high subsonic speeds (Ref. 23). By combining the results of Guderley and Yoshihara's, Vincenti and Wagoner's, and Cole's calculations the flow past thin wedge sections can be given completely through the transonic range permitting a comparison with the present experiments. Some of the investigations mentioned above will be discussed in more detail further on in the present paper.

Available experiments in the transonic range on thin wedge sections are surprisingly few. Pack (Ref. 24) describes some interferometric experiments on 10° and 20° semi-angle wedges made at Braunschweig after the war. His subsonic data appear to be good but the flow in the supersonic interferograms appears to be very non-uniform and not very closely two-dimensional; only one supersonic Mach number was tested where detached shocks occured. His conclusion that the ρ/ρ_∞ distributions on the surface of the 20° semi-angle wedge are very much the same for $M_\infty = 0.803$ and $M_\infty = 1.40$ is interesting but the

statement that this agrees with the theoretical predictions of Maccoll and Codd is incorrect since they indicated that the p/p_o distributions would be nearly the same.

Griffith at Princeton has just recently published the results of some very carefully done experiments on flow past wedge sections of semi-angles of 7°, 10°, 20°, 30°, 45°, and 90° (and several other shapes) with detached shock waves (Ref. 25). These experiments were done in a shock tube and interferograms are presented of the flow fields. The experiments clearly show that the shape of the detached shock and its detachment distance from the sonic point on a wedge depend only on the body thickness and the Mach number (not the wedge angle) when the Mach number is well below the shock attachment Mach number. This is in general agreement with Busemann's considerations in his paper on detached shock waves (Ref. 11).

Liepmann, Ashkenas, and Cole (Ref. 9) made some careful pressure measurements on the surfaces of 6% and 12% biconvex circular arc airfoils at zero angle of attack at high subsonic speeds in connection with studies of shock wave - boundary layer interaction. Some of the results of their tests are combined here with corresponding low supersonic tests from the present investigation to indicate the behavior of the pressure distribution on circular arc airfoils at zero angle of attack through the entire transonic range.

II. APPARATUS AND METHODS

1. Wind Tunnel

The measurements were made in the GALCIT 4 x 10 inch Transonic Wind Tunnel. For a description of the tunnel and the flexible nozzle employed see Ref. 26. The tunnel can be run at both subsonic and low supersonic velocities with continuous Mach number variation through use of the flexible nozzle and a variable second throat nozzle downstream of the test section.

2. Models

The models used were "half airfoils" followed by straight sections. Four of the models were wedges (semi-angles 4.53°, 7.56°, 10.00° and 26.57°) followed by straight sections and the fifth was half of a biconvex circular arc airfoil (8.80% thick) followed by a straight section (see Fig. 1). The distance from the leading edge to the point where the straight section began was of the order of 1/4 inch for all five models. The models were made of tool steel and were very carefully machined and lapped so as to give exact cylindrical surfaces. Two pressure orifices on opposite sides of the airfoil were placed exactly the same distance from the leading edge to aid in setting the model to zero angle of attack by balancing these pressures on an alcohol U-tube. Due to the very short chord lengths vernier protractor measurements of the opening angles of the leading edge were of doubtful accuracy, so the angles were measured by letting the leading edge split a beam of parallel light and measuring

the position of the reflected spots on a wall in back of the model. In this manner the angles could be measured to $\pm$ 0.03°.

3. Interferometer

The interferometer used in this investigation is described in Refs. 27 and 28. One of the main features of this interferometer is that both light beams are passed through the test section; one over the model and the other ahead of the model in the uniform flow field, that is, where the velocity is nearly the free stream velocity. The advantages of this are: 1) the fringe shifts are in relation to the free stream density and 2) the effects of the side wall boundary layers are approximately cancelled out since both beams traverse nearly the same boundary layer at each side window. This leads to improved accuracy when the interferograms are evaluated on the basis of the absolute value of the fringe shift from no-flow conditions. For these tests finite fringe interferograms were used and another method of evaluation was devised which is much simpler and more accurate than the above mentioned technique. Infinite fringe interferograms, while they give the constant density contours immediately, are less accurate than the superimposed finite fringe interferograms because any optical inaccuracies in the system cause the contour fringes to be distorted. These inaccuracies are calibrated out in the superimposed finite fringe interferograms. Also there are times when one does not know whether the density increment between contours of an infinite fringe interferogram is positive or negative; this trouble does not arise with the finite fringe interferograms. A typical

finite fringe interferogram is shown in Fig. 2.

4. Method of Evaluation of Interferograms

The method of evaluation used here depends on two techniques: a) photographic superposition of disturbed and undisturbed interferograms and b) fringe identification by a pressure measured on the model.

Direct photographic superposition of a "no-flow" finite fringe interferogram on a "with-flow" finite fringe interferogram gives rise to dashed shadowy lines (the dashes being where the dark fringes of one picture cross the light fringes of the other); see Fig. 3 for an example of this type of picture. These shadowy lines can easily be shown to be lines of constant density for two-dimensional flow, and are the same contours as would be obtained on an infinite fringe interferogram made with perfect optical surfaces. The increment in density between these shadowy lines is a constant dependent only on the span of the model and the wave length of the monochromatic light being used. This is easily shown since the difference in optical path lengths of the light rays between two adjacent constant density contours must be one wave length of the light being used. For two-dimensional flow the difference in optical path length will simply be $\ell \Delta n$, where ℓ is the span of the model and Δn is the difference in index of refraction between the two light paths. Thus

$$\ell \Delta n = \lambda \tag{1}$$

But the relation between index of refraction and density in a gas is given by

$$n - 1 = k\rho \tag{2}$$

where k = Gladstone-Dale constant (a function of the light frequency and type of gas). Therefore

$$\Delta\rho = \frac{\lambda}{k\ell} \tag{3}$$

where $\Delta\rho$ = difference in density between two adjacent constant density contours. For these experiments

λ = 5461 Å (Mercury green line)

k = 0.1162 ft.^{3}/slug

ℓ = 3.50 inches

so $\frac{\Delta\rho}{\rho_o}$ = 0.0250 per fringe shift, where ρ_o = 0.00211 slugs/ft. was the usual tunnel stagnation density

The advantage of photographic superposition is not only in time saved but also in increased accuracy of evaluation. Any slight changes in fringe spacing or fringe orientation with respect to the "no-flow" interferogram which occur before the "with-flow" interferogram is taken can be almost exactly cancelled out by causing the two superimposed interferograms to coincide exactly in a region where it is known the flow was uniform, since in such regions there should be no isopycnic contours. This is particularly easy to do for supersonic flow if a portion of the flow field ahead of the nose shock wave is included in the interferogram. For subsonic flow care must be taken to include enough of the flow field ahead of the model in the interferogram to have some of the nearly undisturbed flow field for comparison; this was quite simple to do for the small, thin models used in these tests.

The actual superposition technique used here was to first make a print (3 1/2 times enlarged) of the "with-flow" interferogram. This print was then placed under the enlarger and the "no-flow" interferogram negative was put into the enlarger. By changing the enlargement scale and moving the "with-flow" interferogram under the enlarger the fringes were made to coincide exactly in the regions of uniform flow. The constant density contours could then be drawn in on the print. Alternatively the first print could be made on transparent paper (Ansco Reprolith Ortho was used) and when the superposition was accomplished a piece of photo-sensitive paper was slipped under the transparent print and a print of the two interferograms was obtained. This was the technique used for Fig. 3.

In order to identify the density values with the fringes a pressure tap was placed on the model in a region where the pressure gradient was expected to be large. From the pressure reading the density at the pressure tap was calculated using reservoir fluid properties (taking into account entropy changes through shock waves). The pressure tap will always lie between two fringe contours or on a contour, so that, by knowing the density increment between fringe contours, the values of the density on the adjacent contours can be obtained by interpolation. The whole interferogram is determined once the density is known on one contour (except for the shifts through shock waves).

5. Interferometer Sensitivity

It is interesting to note that the interferometric method has its greatest sensitivity in the transonic range. As we pointed out

previously, the density increment between two adjacent contour fringes is a constant

$$\Delta\rho = \frac{\lambda}{k\ell}$$

Now in any part of the flow field where the stagnation density is constant along a streamline,

$$\frac{\rho}{\rho_o} = \left(1 + \frac{\gamma-1}{2} M^2\right)^{-\frac{1}{\gamma-1}} \tag{4}$$

so

$$\frac{d\rho}{\rho_o} = -\left(1 + \frac{\gamma-1}{2} M^2\right)^{-\frac{\gamma}{\gamma-1}} M\,dM \tag{5}$$

Hence the increment in Mach number between adjacent contour fringes is given approximately by

$$\Delta M \doteq \frac{\left(1 + \frac{\gamma-1}{2} M^2\right)^{\frac{\gamma}{\gamma-1}}}{M} \frac{\lambda}{k\ell\rho_o} \quad \text{since} \quad \frac{\Delta\rho}{\rho_o} = \frac{\lambda}{k\ell\rho_o} \tag{6}$$

This function has a minimum at $M = \sqrt{\frac{2}{\gamma+1}}$ which is M = 0.941 for air ($\gamma = 1.4$). A graph of this function is shown in Fig. 4. Note that the Mach number increment per fringe for these tests was always closely equal to 0.05.

Similarly, the expression for the increment in pressure coefficient between adjacent contour fringes is approximately

$$\Delta C_p \doteq \frac{\left(1 + \frac{\gamma-1}{2} M^2\right)^{-1}}{M_\infty^2 \left(1 + \frac{\gamma-1}{2} M^2\right)^{\frac{\gamma}{\gamma-1}}} \frac{\lambda}{k\ell\rho_o} \tag{7}$$

For M close to M_∞, this expression has a minimum at $M_\infty = \sqrt{\frac{2}{2-\gamma}}$ which is 1.832 for air.

6. Side Wall Boundary Layer Effect on Approximating Two-Dimensional Flow

A close approximation to two-dimensional flow over the whole span of the model was required since the interferometer integrates the value of the density from wall to wall. In a non-viscous fluid, letting the model extend from wall to wall would theoretically give two-dimensional flow over the whole span. If the model did not span the whole tunnel, the flow would correspond to that past a model of infinite span with periodic gaps in it where the gaps were equal to twice the distance from the edge of the model to the wall. The effect of the side wall boundary layers, for a model that does not span the tunnel, is roughly to decrease the size of this gap. Approximately the gap size would be decreased by twice the displacement thickness of the wall boundary layer. By making the gap between the edge of the model and the wall approximately equal to the wall boundary layer displacement thickness, one might hope to closely approximate two-dimensional flow over the span. This phenomenon is, of course, very much more complicated than this, particularly in the supersonic case where the shock waves interact with the wall boundary layer. However, by taking circular cylinder and wedge models and varying the gap size in increments of 1/16th of an inch, it was found that the detached bow wave became closely two-dimensional when the gap size was 1/4th of an inch (that is, there was no blur ahead of or behind the shock pictures) which is almost exactly the boundary layer displacement thickness when measured without a model in the test section. When the gap was 3/16th of an inch the shock was

blurred ahead of the main shock and when the gap was 5/16th of an inch it was blurred behind the main shock. These tests were further substantiated by some schlieren pictures, which Mr. Walter G. Vincenti of the NACA Ames Laboratory kindly made available to us, showing a view looking down on a wedge model so that the leading edge of the detached shock appeared as a line; by varying the model span a discrete value of the span was found where this line was almost exactly parallel to the leading edge of the model, while for just slight variations from this gap size the shock was curved forward or backward. Fig. 2 shows a finite fringe interferogram of the circular arc section with a detached shock where the definition of the shock wave was unusually sharp. This is strong, but of course not conclusive, evidence that the flow was closely two-dimensional over most of the span. Further evidence that the flow differed from two-dimensional flow only slightly is given in the next section.

7. Side Wall Boundary Layer Effect on Interferogram Evaluations

A result of the method of interferogram evaluation described above is that the effect of the side wall boundary layer is approximately cancelled out, since the over-all fringe shift from no-flow conditions is unimportant, only the relative fringe shifts from a point of known density being used. This is strictly true only if the integrated side wall boundary layer density defined by

$$\int_0^{\delta} \rho dy \qquad \text{where } y \text{ is the direction perpendicular to the tunnel wall and } y = 0 \text{ is the wall} \qquad (8)$$

is the same over the entire field of view of the interferometer.

Obviously, this can never be exactly true since the pressure field caused by the model, the boundary layer growth, and the shock wave - boundary layer interaction all tend to change this value. An indication that all these effects might be small was obtained from the model tests where pressures were measured at two points on the model in the center of the span, where the flow is closely two-dimensional; the density increment between these two points on the model was compared with the density increment given by the interferogram. The standard deviation from zero of the difference between these two increments over the whole range of test Mach numbers was about 1% of the stagnation density. Also, the values of pressure drag coefficient obtained interferometrically for the attached shock wave cases checked the oblique shock theory very closely, and it is well known that the oblique shock theory checks experiment quite well.

8. Determination of Free Stream Mach Number

An interesting result of the method of evaluation just described is that the free stream Mach number in subsonic flow can be determined from the interferogram and the measured pressure on the model, provided a large enough field of view ahead of the model is obtained in the interferogram. This can be done by noticing that a certain number of compression contours appear around the leading edge and then expansion contours follow these toward the back part of the airfoil; the center fringe corresponding to free stream density can then be traced out into the flow field (see Figs. 9 and 10 of the 10° wedge in subsonic flow). The exact value of the density can be determined

on this fringe as described previously and hence, knowing the stagnation density in the settling chamber, the effective free stream Mach number can be determined from the isentropic flow relations. It is believed that this effective Mach number is a good approximation to the free flight free stream Mach number and would give the same flow as that measured in the wind tunnel for the very small models used in these tests.

This method is more accurate at high subsonic speeds that at low speeds since more contour lines are obtained on the airfoil at the higher speeds (see above). The estimated accuracy in determining free stream Mach number in this way was $\pm$ 0.01 for the range of subsonic Mach numbers tested.

The free stream Mach numbers for the supersonic tests were obtained by calibrating the flexible nozzle jack settings versus Mach number with a static pressure probe in the center of the tunnel. The probe was traversed up and downstream in the region where the models were to be tested and an average Mach number was obtained there. The standard deviations from this average value were of the order of $\pm$ 0.005 in Mach number for the range of supersonic Mach numbers tested.

9. Wind Tunnel Choking

In all the subsonic testing the embedded supersonic zone was not allowed to touch the upper or lower walls. In one or two of the low supersonic tests there was a question whether the embedded subsonic zone touched the ceiling or not. In case it did, it is well known

that in such cases the detached shock changes its curvature near the ceiling so as to come in nearly normal to the walls. Since the models were so very small (1/16" thick compared to the 10" height of the tunnel) it is believed that the effect of this on the pressure distribution was negligible.

10. Reynolds Number

The value of the Reynolds number for all of these tests was approximately 60,000 based on the chord of the model. The boundary layer on the models was laminar and no effort was made to trip the boundary layer to make it turbulent. The compression region in the shocks shown in the high subsonic flow interferograms is believed to be associated with the laminar boundary layer, as mentioned previously.

III. THEORETICAL WORK ON TRANSONIC FLOW

1. Relaxation Calculations

In 1946 J. W. Maccoll presented a paper (Ref. 29) where he described a relaxation calculation of the compressible flow past a 20° semi-angle wedge followed by a straight section at Mach numbers of 0.7 and 1.5. The flow field in both cases contained both subsonic and supersonic velocities. His main assumptions were: 1) sonic velocity occurs at the shoulder and 2) the streamlines of the flow are perpendicular to the sonic line (that is, the line where sonic velocity occurs in the flow). The first assumption can be shown to be correct (see Ref. 23) so that indeed it is not an assumption. The second assumption, as Maccoll realized, was only approximately correct for $M_{\infty} = 1.5$ and certainly quite incorrect far away from the wedge at $M_{\infty} = 0.7$ (since the assumption leads to an infinite supersonic region above the wedge). In effect his solution at $M_{\infty} = 0.7$ was "choked" in the sense that the back part of the body could have no influence on the front part. It is well known that for bodies at high subsonic speeds a finite closed supersonic region occurs in the flow, so that the sonic line makes all angles possible with the streamlines, including 0°. The method of solution used was to assume positions of the shock wave and sonic line, calculate the residues in the relaxation net using the isentropic flow equations (an approximation since flow behind a curved shock is not isentropic) then readjust the shock wave and sonic line location, calculate again, etc., iterating until the solution closely repeated itself. Maccoll found that

the p/p_o' distribution on the wedge surface at $M_\infty = 1.5$ was nearly identical with the p/p_o distribution at $M_\infty = 0.7$. This led him to propose that the pressure in the transonic region, on bodies with distinct corners, varied as the stagnation pressure and he presented a drag curve through $M_\infty = 1$ for the 20° semi-angle wedge calculated on this basis.

G. Drougge in 1948, following Maccoll, calculated the flow past a finite cone of 45° semi-angle with detached shock wave at $M_\infty = 1.80$ and $M_\infty = 2.15$, using the same assumptions as Maccoll (Ref. 19). He also made experiments on this cone and found the agreement with his theory rather good. He made several tests at lower supersonic Mach numbers also, and found that the p/p_o distribution on the cone surface did remain nearly constant except as the Mach number became close to the attachment Mach number.

J. Drebinger in 1950 showed how to calculate, by relaxation techniques, the flow past finite cones and wedges with detached shocks, eliminating the isentropic flow assumption and the assumption on the streamlines being perpendicular to the sonic line (Ref. 20). He calculated a specific example; a 26.6° semi-angle wedge at $M_\infty = 1.440$ and checked the calculated shock wave shape and position experimentally. His calculations showed that, even for the detached shock case, the streamlines differed from being perpendicular to the sonic lines by angles as large as 30°. His calculation was checked in detail experimentally in these tests and agreement was found to be excellent.

2. Transonic Perturbation Theory

By assuming that the velocity component parallel to the free stream direction differs only by a small quantity, u , from a^* , the critical velocity, and keeping only the highest order terms in the differential equation, the equations of two-dimensional irrotational fluid motion are reduced to

$$\begin{aligned} (\gamma+1)\frac{u}{a^*}\frac{\partial u}{\partial x} + \frac{\partial v}{\partial y} &= 0 \\ \frac{\partial u}{\partial y} - \frac{\partial v}{\partial x} &= 0 \end{aligned} \tag{9}$$

It was from these equations that von Kármán and Guderley independently arrived at the transonic similarity laws (Refs. 10 and 5). For two-dimensional steady flow past sections whose shape functions are the same, these laws imply that

$$\frac{M^2-1}{(\gamma+1)\ t/c^{\ 2/3}} = f\left\{\frac{M_\infty^2-1}{[(\gamma+1)\ t/c]^{2/3}}\right\} \tag{10}$$

where M is the local Mach number on the surface of the section. The similarity in pressure and drag coefficients is then

$$\frac{(\gamma+1)^{1/3}\,C_p}{(t/c)^{2/3}} = g\left\{\frac{M_\infty^2-1}{[(\gamma+1)\ t/c]^{2/3}}\right\} \tag{11}$$

$$\frac{(\gamma+1)^{1/3}\,C_D}{(t/c)^{5/3}} = h\left\{\frac{M_\infty^2-1}{[(\gamma+1)\ t/c]^{2/3}}\right\} \tag{12}$$

We shall call these quantities reduced local Mach number, reduced free stream Mach number, reduced pressure coefficient and reduced drag coefficient, respectively, using symbols ξ , ξ_∞, $\tilde{C}_p$ and $\tilde{C}_D$.

By interchanging dependent and independent variables in the

perturbation equations the problem becomes linear

$$\bar{u}\frac{\partial y}{\partial \bar{v}} + \frac{\partial y}{\partial \bar{u}} = 0 \qquad \text{where} \quad \begin{cases} \bar{u} = (\gamma+1)\dfrac{u}{a^*} \\ \bar{v} = (\gamma+1)\dfrac{v}{a^*} \end{cases} \tag{13}$$

$$\frac{\partial x}{\partial \bar{v}} - \frac{\partial y}{\partial \bar{u}} = 0$$

and by eliminating x by differentiation, the Tricomi equation is obtained

$$\bar{u}\frac{\partial^2 y}{\partial \bar{v}^2} + \frac{\partial^2 y}{\partial \bar{u}^2} = 0 \tag{14}$$

The main difficulties with this hodograph $(\bar{u}, \bar{v})$ plane are: a) the mapping of physical boundaries into the hodograph plane is in general not known until the solution to the problem is known so that it is not known where to apply the boundary conditions in the hodograph plane and b) the mapping is often multi-valued, complicating the solution. Two interesting cases are known where these difficulties are avoided. They are: a) the free jet, studied by Tschaplygin in 1905 and b) the finite wedge, studied recently by Guderley and Yoshihara, Vincenti and Wagoner, and Cole. These latter studies came to the author's attention after the present experimental study of the finite wedge in transonic flow had begun and served to make the study more interesting since the data could then be compared with the theoretical results.

3. Theoretical Studies of Transonic Flow Past Thin Wedge Sections

G. Guderley was apparently the first to formulate the problem of the thin finite wedge in the hodograph; he and H. Yoshihara found an approximate solution to the problem of the flow past a thin double

wedge profile at zero angle of attack at Mach number one using the transonic perturbation equations (Ref. 21).

W. G. Vincenti and C. B. Wagoner considered the thin double wedge profile at zero angle of attack for low supersonic reduced Mach numbers where the shock wave is detached (Ref. 22). Their solutions were effected by relaxation calculations in the hodograph plane. Here the bow shock wave and the sonic line are fixed boundaries (their positions are not known originally in the physical plane) and the boundary condition on the shock is the slope of the streamlines (or y = constant lines). This boundary condition was first shown by Busemann, who aptly called the configuration a "hedge hog."

J. D. Cole has recently given a simple approximate analytical solution to the flow past a thin wedge at zero angle of attack followed by a straight section at high subsonic speeds, $M_\infty \leq 1$ (Ref. 23). His solution satisfies the Tricomi equation, and the boundary conditions on the wedge and at infinity but not the boundary conditions on the sonic line. Effectively his solution gives a finite vertical sonic line from the shoulder which is also a limiting line. Cole has indicated that this solution is the singular part of the solution in the hodograph, and as such is most likely the main part of the solution. It is interesting to note that the drag curve slope and curvature at $M_\infty = 1$ obtained from Cole's solution agree exactly with the values obtained from the simple physical considerations of the next section. Also, the pressure distribution on the wedge at $M_\infty = 1$ agrees within 1 or 2% with that obtained by Guderley and Yoshihara.

Since the back half of a double wedge profile has only a very

weak influence on the pressure distribution on the front half for $M_\infty > 1$ (only through the "last Mach wave" from the shoulder point to the sonic point on the detached shock), it is reasonable to take the solution of the double wedge at $M_\infty \geq 1$ and use the front half solutions in connection with Cole's results for $M_\infty \leq 1$ for the wedge followed by a straight section and thus have a solution for the latter semi-infinite body completely through the transonic range. By using linearized subsonic theory and the shock-expansion supersonic theory, the zero angle of attack flow is obtained for all possible values of M_∞.

Tsien and Baron (Ref. 30) have shown that the shock-expansion theory can be expressed in the transonic similarity form for thin bodies in pure supersonic flow near $M_\infty = 1$.

von Kármán (Ref. 10) has indicated also how linearized subsonic and supersonic flow results may be written in the transonic similarity form since, from the Prandtl-Glauert similarity,

$$C_p = \frac{t/c}{\sqrt{1-M_\infty^2}}\, f\left(\frac{x}{c}, \sqrt{1-M_\infty^2}\,\frac{y}{c}\right) \qquad \left\{\begin{array}{l}\text{in linearized}\\ \text{subsonic theory}\end{array}\right. \tag{15}$$

$$C_p = \frac{t/c}{\sqrt{M_\infty^2-1}}\, g\left(\frac{x}{c}, \sqrt{M_\infty^2-1}\,\frac{y}{c}\right) \qquad \left\{\begin{array}{l}\text{in linearized}\\ \text{supersonic theory}\end{array}\right. \tag{16}$$

and from the expressions for reduced pressure coefficient and Mach number, multiplying both sides by $\frac{(\gamma+1)^{1/3}}{(t/c)^{2/3}}$, these equations may also be written as:

$$\frac{(\gamma+1)^{1/3} C_p}{(t/c)^{2/3}} = \sqrt{\frac{\left[(\gamma+1)\,t/c\right]^{2/3}}{1-M_\infty^2}}\, f\left(\frac{x}{c}, \sqrt{\frac{1-M_\infty^2}{\left[(\gamma+1)\,t/c\right]^{2/3}}}\left[(\gamma+1)\frac{t}{c}\right]^{1/3}\frac{y}{c}\right) \tag{15'}$$

$$\frac{(\gamma+1)^{1/3} C_p}{(t/c)^{2/3}} = \sqrt{\frac{\left[(\gamma+1)\, t/c\right]^{2/3}}{M_\infty^2 - 1}}\; g\left(\frac{x}{c}, \sqrt{\frac{M_\infty^2 - 1}{\left[(\gamma+1)\, t/c\right]^{2/3}}}\left[(\gamma+1)\frac{t}{c}\right]^{1/3}\frac{y}{c}\right) \quad (16')$$

but

$$\tilde{C}_p = \frac{(\gamma+1)^{1/3} C_p}{(t/c)^{2/3}}$$

$$\xi_\infty = \frac{M_\infty^2 - 1}{\left[(\gamma+1)\, t/c\right]^{2/3}}$$

$$\tilde{y} = \left[(\gamma+1)\, t/c\right]^{1/3} y$$

so we may write Eqs. (15) and (16) in transonic form

$$\hat{C}_p = F\left(\frac{x}{c}, \frac{\tilde{y}}{c}, \sqrt{-\xi_\infty}\right) \quad (17)$$

$$\tilde{C}_p = G\left(\frac{x}{c}, \frac{\tilde{y}}{c}, \sqrt{\xi_\infty}\right) \quad (18)$$

The subsonic pressure distribution and drag coefficient curves have been calculated here from Cole's analytical expressions and, combined with the results of Guderley and Yoshihara, Vincenti and Wagoner, and Tsien and Baron, the curves for reduced pressure and Mach number distribution and reduced drag coefficient* are given in Figs. 5 to 8 for the finite wedge followed by a straight section.

It can be shown that Cole's solution for large negative values of ξ_∞ goes over exactly into the linearized subsonic solution (see

*The reduced drag coefficient given in Fig. 8 is that for the half wedge and is equal to

$$\tilde{C}_D = \int_0^1 \tilde{C}_p \, d\left(\frac{x}{c}\right)$$

Appendix 1). The reduced pressure coefficient curve for $\xi_\infty = -2.02$ in Fig. 7 is so nearly identical for both solutions that they can not be told apart (except that Cole's solution goes to $C_{p_{cr}}$ at $x/c = 1$ while the linearized solution goes to $-\infty$). This is to be expected since the transonic perturbation equations are not restricted to transonic flow but apply equally well to completely subsonic and completely supersonic flow.* The transonic equation can be written in the form

$$(1-M_\infty^2)\frac{\partial^2\varphi}{\partial x^2} + \frac{\partial^2\varphi}{\partial y^2} = \frac{(\gamma+1)M_\infty}{a_\infty}\frac{\partial\varphi}{\partial x}\frac{\partial^2\varphi}{\partial x^2} \qquad (19)$$

where φ is the perturbation potential such that $u = U + \frac{\partial\varphi}{\partial x}$, $v = \frac{\partial\varphi}{\partial y}$. Thus it is clear that for completely subsonic or completely supersonic flows the term on the right is negligibly small but becomes of paramount importance in transonic flow.

*This was pointed out to the author by Dr. Milton Van Dyke of the NACA Ames Laboratory.

IV. CHARACTERISTIC FEATURES OF TRANSONIC FLOW PAST WEDGE AND CIRCULAR ARC SECTIONS

1. Characteristic Free Stream Mach Numbers

(a) Critical Mach Number

The Mach number at which sonic velocity first appears on the wedge is $M_\infty = 0$ (within the inviscid theory) since subsonic flow can not turn a sharp corner. Due to the fact that the boundary layer rounds off the corner, and perhaps also due to the spatial resolution limitations of the interferometric method, sonic velocity was not found there experimentally until approximately $\xi_\infty = -0.80$ for the wedges.

The critical Mach number for a half circular arc airfoil followed by a straight section can be obtained approximately from linearized subsonic theory. This theory gives the surface pressure distribution as

$$C_p = \frac{-4(t/c)}{\pi\sqrt{1-M_\infty^2}} \left\{ 1 - \left(1 - \frac{x}{c}\right) \log \frac{x/c}{1 - x/c} \right\} \tag{20}$$

which yields

$$C_{p_{MIN.}} = \frac{-1.626\,(t/c)}{\sqrt{1-M_\infty^2}} \quad \text{at} \quad \frac{x}{c} = 0.783 \quad \text{(see Appendix 2)} \tag{21}$$

This equation can also be written in transonic similarity form by multiplying both sides by $\frac{(\gamma+1)^{1/3}}{(t/c)^{2/3}}$ (as shown in the previous section):

$$\tilde{C}_{p_{MIN.}} = \frac{-1.626}{\sqrt{-\xi_\infty}} \tag{22}$$

Now, within the transonic perturbation theory

$$\tilde{C}_p = -2\,(\xi - \xi_\infty) \tag{23}$$

Hence

$$\tilde{C}_{P_{CR}} = 2\,\xi_{\infty} \tag{24}$$

Equating $\tilde{C}_{P_{MIN.}}$ to $\tilde{C}_{P_{CR}}$ we obtain the critical reduced Mach number

$$\xi_{\infty_{CR}} = -0.871$$

For the thickness ratio t/c = 0.088 used in these tests, this predicts a critical Mach number of 0.834 at x/c = 0.783. Experimentally the critical Mach number was found to be 0.825 and occurred somewhere between x/c = 0.75 and 0.95 (the pressure distribution was very flat in this range). It is interesting to note that the experimental $M_{\infty_{CR}}$ was higher for the wedges than for the circular arc profile of the same thickness ratio. This was probably due to a combination of three effects: 1) The boundary layer for the same Reynolds numbers used here was fairly thick in comparison to the dimensions of the model and thus it "rounded off" the shoulder more than would be the case at higher Reynolds numbers. 2) The height of the supersonic zone, even for an ideal non-viscous flow past thin wedges, appears to be quite small until the free stream Mach number is quite close to one. This is apparent from Cole's theory and also from the argument in Ref. 1 that the height of shocks in the supersonic zone must be of the form

$$\left[(\gamma+1)\frac{t}{c}\right]^{1/3}\frac{h}{c} = \frac{1}{\xi_{\infty}^{3}}\,\tilde{C}_{D}$$

3) The spatial resolution of the interferometric method may not have been sufficient to detect very small supersonic zones near the shoulder. There is also a large refraction error near the shoulder due to the high density gradients which tends to obscure details of the flow there.

(b) Shock Attachment Mach Number

The shock attachment Mach number depends only on the opening angle of the profile at the leading edge and can be predicted quite precisely by oblique shock theory. If θ is the semi-opening angle then it can be shown that approximately, for thin profiles,

$$\xi_{\infty_A} = \frac{M_{\infty_A}^2 - 1}{[(\gamma+1)\theta]^{2/3}} = \frac{3}{4^{2/3}} \qquad \text{(see Appendix 3)} \qquad (25)$$

If t/c is the thickness ratio of the circular arc section, $\theta \doteq 2(t/c)$. Hence for the circular arc profile

$$\xi_{\infty_A} = \frac{3}{2^{2/3}} \qquad (26)$$

(c) Mach Number at which Sonic Velocity Appears Behind an Oblique Shock

This Mach Number, M_{∞_S}, is just slightly higher than M_{∞_A} and again is a function only of the opening angle. These values can also be found quite precisely from oblique shock theory, and approximately in similarity form can be given as

$$\xi_{\infty_S} = \frac{M_{\infty_S}^2 - 1}{[(\gamma+1)\theta]^{2/3}} = 2^{1/3} \quad \text{for the wedge} \quad \text{(see Appendix 3)} \qquad (27)$$

and

$$\xi_{\infty_S} = 2 \qquad \text{for the circular arc section} \qquad (28)$$

2. Characteristic Values of the Local Mach Number

(a) Mach Number at Leading Edge

The Mach number at the leading edge is zero (a stagnation point) for all free stream Mach numbers less than the attachment Mach number.

(b) Mach Number at the Shoulder of the Wedge

The Mach number at the shoulder of the wedge just before the turn is always one. This is easily seen in the case of flow with detached shock since the only characteristic distance of the finite wedge is the distance from the leading edge to the shoulder which must determine the shock detachment distance and if the sonic point occurred ahead of the shoulder, the shoulder could not influence the shock position. Subsonic flow cannot turn a sharp corner so the flow must therefore reach Mach number one right at the corner. In the case of subsonic free stream flow the argument is not as simple (see Ref. 23).

At the shoulder the flow around the corner is locally a centered Prandtl-Meyer fan starting from M = 1. The Mach number just behind the corner is thus determined only by the wedge angle and is independent of the free stream Mach number. Behind this point the flow will recompress to the free stream Mach number through a shock or series of shocks, for free stream Mach numbers less than the attachment Mach number. The expression for Mach number M_{PM} behind an expansion from M = 1 through an angle θ is

$$\theta = \sqrt{\frac{\gamma+1}{\gamma-1}}\ TAN^{-1}\sqrt{\frac{\gamma-1}{\gamma+1}}\sqrt{M_{PM}^2-1} - TAN^{-1}\sqrt{M_{PM}^2-1} \tag{29}$$

Expanding the right hand side in powers of $\sqrt{M_{PM}^2-1}$ (assumed small) the first non-zero term yields

$$\theta \doteq \frac{2}{3}\frac{(M_{PM}^2-1)^{3/2}}{\gamma+1} \qquad \text{which is in transonic similarity form} \tag{30}$$

so

$$\xi_{PM} = \frac{M_{PM}^2-1}{[(\gamma+1)\theta]^{2/3}} \doteq \left(\frac{3}{2}\right)^{2/3} \tag{31}$$

V. PRESSURE DISTRIBUTION ON BODIES MOVING THROUGH AN INFINITE FLUID AT SPEEDS NEAR MACH NUMBER ONE

1. Stationary Value of Local Mach Number at Free Stream Mach Number One

During the course of these investigations it was found that for the wedge and circular arc sections the local Mach number distributions on these sections at very high subsonic speeds (above $M_{\infty_{CR}}$ but below choking Mach number) and at very low supersonic speeds (where the detached shock wave was a chord length or so ahead of the section) were nearly identical. In trying to understand why this should be so, the following explanation was derived: 1) At low supersonic speeds the bow shock wave is detached a great distance ahead of the profile and a subsonic flow region is embedded in the flow field between the shock and the sonic line. The part of the shock directly ahead of the profile is nearly normal over quite a distance (of course, the slope of the shock asymptotically tends to the slope of the Mach wave of the free stream flow at large distances lateral to the flow direction). H. Nagamatsu (Ref. 33) has previously indicated this and points out that the flow past the profile should be closely approximated by assuming the profile is in a high speed subsonic flow where the velocity distribution at infinity is slightly non-uniform, the minimum velocity being directly ahead of the profile and equal to the velocity behind the normal shock, and then increasing in both lateral directions. 2) Now the normal shock near Mach number one is nearly symmetrical in the sense that the Mach number behind the shock is just

as much below one as the Mach number ahead is above one. This follows from the normal shock relation:

$$1 - M_2^2 = \frac{M_1^2 - 1}{1 + \frac{2\gamma}{\gamma+1}(M_1^2 - 1)} \qquad \begin{cases} M_1 = \text{Mach number ahead} \\ M_2 = \text{Mach number behind} \end{cases} \tag{32}$$

so near $M_1 = 1$;

$$1 - M_2^2 \doteq M_1^2 - 1 \tag{33}$$

or

$$1 - M_2 \doteq M_1 - 1 \tag{34}$$

Therefore if $M_\infty = 1 + \epsilon$ where ϵ is small, the flow past the profile is nearly the same as the flow past the profile at $M_\infty = 1 - \epsilon$ since the Mach number behind the central part of the detached shock wave is almost exactly $1 - \epsilon$. It follows therefore that the local Mach number distribution on the profile surface must have a stationary value at $M_\infty = 1$, and furthermore vary only slowly in the neighborhood of $M_\infty = 1$. Mathematically this means

$$\left.\frac{dM}{dM_\infty}\right|_{M_\infty = 0} = 0 \tag{35}$$

It should be noticed that this argument is based on two assumptions:* 1) The detached bow wave moves very far ahead of the profile as the flight Mach number decreases toward one. 2) The radius of curvature of the detached bow wave at points directly ahead of the profile becomes extremely large as the flight Mach number decreases toward one.

Examining these assumptions it would seem that the same

*It is believed that these are not actually assumptions but are capable of demonstration if one assumes a smooth variation of drag through Mach number one. Further considerations of this point will be published in the near future.

reasoning should apply to any finite three-dimensional body in an infinite fluid traveling at speeds near Mach number one, except that now two radii of curvature at points on the detached bow wave ahead of the body must be assumed to become large as the flight Mach number decreases toward one. The detached bow wave is so far away from the body at speeds just slightly above Mach number one that the body appears as only a very small object in relation to the radii of curvature of the bow wave, and hence, it would appear as though the shape and attitude of the body could have no appreciable effect in changing the argument presented above.

The reasoning should also apply to an infinite yawed cylinder (whose cross-section may be finite or, if the angle of attack is zero, may extend infinitely far downstream) provided that the Mach number considered is the component of the Mach number normal to the generators of the cylinder.

These arguments are for steady flight speeds. Large accelerations through sonic flight speed could conceivably modify the phenomenon. Thus it is difficult to judge whether or not the available flight test data confirms the concept or not since nearly all such data comes from missile tests that involved large accelerations (or decelerations) through sonic flight speeds. The transonic "bump" tests of Weaver on sweptback wings (Ref. 2) would seem to support our conclusions since they show drag coefficient maxima very near Mach number one, a necessary consequence of the concept for finite three-dimensional bodies and finite unswept two-dimensional bodies as we shall now show.

2. Slope of Pressure and Drag Coefficient Curves at $M_\infty = 1$

Eq. (35) enables one to calculate the slope of the pressure and drag coefficient curves at Mach number one as follows:

$$C_p = \frac{p - p_\infty}{q_\infty} \tag{36}$$

$$= \frac{2}{\gamma M_\infty^2} \left\{ \left(\frac{1 + \frac{\gamma - 1}{2} M_\infty^2}{1 + \frac{\gamma - 1}{2} M^2} \right)^{\frac{\gamma}{\gamma - 1}} - 1 \right\} \quad \text{for isentropic flow} \tag{37}$$

so

$$\left. \frac{dC_p}{dM_\infty} \right|_{M_\infty = 1} = \frac{4}{\gamma + 1} - \frac{2C_p \big|_{M_\infty = 1}}{\gamma + 1} \quad \text{using} \quad \left. \frac{dM}{dM_\infty} \right|_{M_\infty = 1} = 0 \tag{38}$$

Now for a two-dimensional body the pressure drag coefficient (based on the chord) is given by the contour integral

$$C_D = \frac{-1}{c} \oint C_p \, (\hat{\imath} \cdot \hat{n}) \, ds \tag{39}$$

where

$\hat{\imath}$ = unit vector in stream direction

$\hat{n}$ = unit normal to profile pointing outward

ds = element of length along profile contour

so if angle of attack is constant and M_∞ is changing

$$\left. \frac{dC_D}{dM_\infty} \right|_{M_\infty = 1} = -\frac{1}{c} \oint \left(\frac{4}{\gamma + 1} - \frac{2C_p \big|_{M_\infty = 1}}{\gamma + 1} \right) \hat{\imath} \cdot \hat{n} \, ds \tag{40}$$

but $\oint \hat{\imath} \cdot \hat{n} \, ds = 0$ for a closed contour, so

$$\left. \frac{dC_D}{dM_\infty} \right|_{M_\infty = 1} = -\frac{2}{\gamma + 1} \, C_D \big|_{M_\infty = 1} \tag{41}$$

For the front part of a profile (defined as that part ahead of the maximum thickness) the usual definition of a drag coefficient is

$$C_{D_F} = -\frac{1}{c} \int_a^b C_p \, \hat{\imath} \cdot n \, ds \tag{42}$$

where $\int_a^b$ means the counter-clockwise line integral from the point of maximum thickness on the upper surface to the point of maximum thickness on the lower surface; thus

$$\left.\frac{dC_{D_F}}{dM_\infty}\right|_{M_\infty=1} = -\frac{1}{c}\int_a^b \left(\frac{4}{\gamma+1} - \frac{2C_p|_{M_\infty=1}}{\gamma+1}\right) \hat{\imath}\cdot\hat{n}\, ds$$

so

$$\left.\frac{dC_{D_F}}{dM_\infty}\right|_{M_\infty=1} = \frac{4}{\gamma+1}\,\frac{t}{c}\cos\alpha - \frac{2}{\gamma+1}\,C_{D_F}|_{M_\infty=1} \tag{43}$$

where

t = maximum thickness of profile

α = angle of attack of profile

Similarly the drag coefficient for the rear part is

$$C_{D_R} = -\frac{1}{c}\int_b^a C_p\,\hat{\imath}\cdot\hat{n}\, ds \tag{44}$$

so

$$\left.\frac{dC_{D_R}}{dM_\infty}\right|_{M_\infty=1} = -\frac{4}{\gamma+1}\,\frac{t}{c}\cos\alpha - \frac{2}{\gamma+1}\,C_{D_R}|_{M_\infty=1} \tag{45}$$

For the tests on wedge and circular arc sections followed by straight sections we shall often use the concept of drag coefficient of the front part of the section.

For bodies of revolution (which includes spheres, cone-cylinders, etc.) the pressure drag coefficient (based on maximum cross-sectional area) at zero angle of attack is

$$C_D = \int_{x/\ell=0}^{1} C_p\, d\left(\frac{r}{R}\right)^2 \tag{46}$$

where:

R = maximum radius of body

ℓ = length of body

x = distance from nose along axis

Therefore

$$\left.\frac{dC_D}{dM_\infty}\right|_{M_\infty=1} = \frac{-2C_D\big|_{M_\infty=1}}{\gamma+1}$$

as before in the two-dimensional case. However, for front and back drag coefficients we have

$$C_{D_F} = \int_{r=0}^{R} C_p \, d\left(\frac{r}{R}\right)^2 \tag{47}$$

so

$$\left.\frac{dC_{D_F}}{dM_\infty}\right|_{M_\infty=1} = \frac{4}{\gamma+1} - \frac{2}{\gamma+1} C_{D_F}\big|_{M_\infty=1} \tag{48a}$$

and similarly

$$\left.\frac{dC_{D_R}}{dM_\infty}\right|_{M_\infty=1} = -\frac{4}{\gamma+1} - \frac{2}{\gamma+1} C_{D_R}\big|_{M_\infty=1} \tag{48b}$$

and these differ from two-dimensional values obtained above in Eqs. (43) and (45) by not involving the fineness ratio of the body (this is of course due to the different reference areas for drag coefficients).

For the general finite three-dimensional body the pressure drag coefficient is given by

$$C_D = -\frac{1}{A} \iint_S C_p \, (\hat{i}\cdot\hat{n}) \, d\sigma \tag{49}$$

where A is some reference area of the body and S is the surface of the body. It follows as it did previously that

$$\left.\frac{dC_D}{dM_\infty}\right|_{M_\infty=1} = -\frac{2}{\gamma+1} C_D\big|_{M_\infty=1}$$

3. Slope of the Drag Coefficient Curve at $M_\infty = 1$ in Transonic Similarity Parameters for Two-Dimensional Flows

Within the transonic approximation

$$\tilde{C}_p = -2(\xi - \xi_\infty) \tag{50}$$

so

$$\frac{d\tilde{C}_p}{d\xi_\infty} = -2\left(\frac{d\xi}{d\xi_\infty} - 1\right) \tag{51}$$

Now $\left.\frac{dM}{dM_\infty}\right|_{M_\infty = 1} = 0$ implies that $\left.\frac{d\xi}{d\xi_\infty}\right|_{\xi_\infty = 0} = 0$; hence

$$\left.\frac{d\tilde{C}_p}{d\xi_\infty}\right|_{\xi_\infty = 0} = 2 \tag{52}$$

Now

$$\tilde{C}_p = -\frac{1}{t/c}\oint \tilde{C}_p \, \hat{\imath}\cdot\hat{n}\, d\left(\frac{s}{c}\right) \tag{53}$$

so

$$\left.\frac{d\tilde{C}_D}{d\xi_\infty}\right|_{\xi_\infty = 0} = 0 \tag{54}$$

Similarly it is easy to show that

$$\left.\frac{d\tilde{C}_{D_F}}{d\xi_\infty}\right|_{\xi_\infty = 0} = 2 \tag{55}$$

and

$$\left.\frac{dC_{D_R}}{d\xi_\infty}\right|_{\xi_\infty = 0} = -2 \tag{56}$$

4. Other Data Showing the Slow Variation of Local Mach Number Near $M_\infty = 1$

As we have mentioned previously, J. W. Maccoll in 1946 had already proposed the slow variation of local Mach number near $M_\infty = 1$ on "bodies having distinct corners." It appears that this latter restriction is not necessary. Maccoll's proposal was based on rather slim evidence and it is believed that here, on the basis of the argument presented concerning the normal shock, the principle is explained more convincingly. Also the experimental evidence given here and by

Drougge (Ref. 19), Bleakney and Griffith (personal communication), Weaver (Ref. 2), and by some NACA reports, tends to bear out the conclusions of slow variation of local Mach number on bodies near $M_\infty = 1$.

This fact is sometimes slightly obscured in the NACA reports because pressure coefficient was plotted instead of ρ/ρ_o or local Mach number. However, constant Mach number lines were sometimes drawn on these plots and there the evidence shows up strongly (see for example Ref. 39, Figs. 7-11, pp. 36 and 37). The relative constancy of local Mach number distribution near $M_\infty = 1$ for airfoils at angle of attack is also shown clearly in Figs. 8, 9, and 10 of Ref. 31.

VI. ON COMPARING THEORY AND EXPERIMENT

In Refs. 1 and 22 discussions were presented on the philosophy of comparing experiments with approximate theories, and we shall not repeat their discussions here, except to mention that in some of the theoretical curves presented here the values have been shown with a certain spread which results from using a pressure coefficient equal to $-2\,\frac{u-u_\infty}{a^*}$ or $-2\,\frac{u-u_\infty}{U}$ (the former value is the one that fits into transonic similarity theory, the latter value is the one more commonly used in perturbation analysis).

In connection with the idea presented in Ref. 1 of extrapolating experimental data to zero thickness in order to compare with results from transonic perturbation analyses, it is interesting to note that the characteristic Mach numbers mentioned in Section IV can be presented in powers of the thickness of the wedge (or equivalently in powers of the wedge angle), the first term of which gives the transonic similarity expression; two of these values are

$$\xi_{\infty_S} = \frac{M_{\infty_S}^2 - 1}{\left[(\gamma+1)\theta\right]^{2/3}} = 2^{1/3}\left[1 + \frac{19\gamma+2}{24}\left(\frac{2}{\gamma+1}\right)^{1/3}\theta^{2/3} + O(\theta^{4/3})\right] \qquad (57)$$

$$\xi_{P_M} = \frac{M_{P_M}^2 - 1}{\left[(\gamma+1)\theta\right]^{2/3}} = \left(\frac{3}{2}\right)^{2/3}\left[1 + \frac{4\gamma}{5(\gamma+1)}\left(\frac{3(\gamma+1)}{2}\right)^{2/3}\theta^{2/3} + O(\theta^{4/3})\right] \qquad (58)$$

(see Appendices 4 and 5)

In transonic perturbation theory the terms in θ on the right hand side are neglected. This can lead to fairly large errors for even moderately large values of θ since the approach to $\theta = 0$ is nonlinear and

$$\frac{d\xi_{\infty_S}}{d\theta} \text{ and } \frac{d\xi_{PM}}{d\theta} \longrightarrow \infty \text{ as } \theta \to 0 \tag{59}$$

Judging from this one might expect that quantitative agreement of transonic perturbation analyses with experiment would not be so good. However, in comparing two similar shapes with only slightly different thickness ratios by transonic similarity considerations one would expect fairly good agreement.

VII. EXPERIMENTAL RESULTS

1. Flow Field Near the 10° Wedge

Figs. 9 through 15 show interferograms of the flow past the 10° semi-angle wedge for fourteen Mach numbers from 0.700 to 0.892 and 1.207 to 1.465 (the interferograms for the 4 1/2° and 7 1/2° wedge were very similar and hence are not shown here). Notice that the lines of constant density in the subsonic flow interferograms are roughly elliptical in shape as predicted by the theory (see Appendices 1 and 2). A supersonic flow region was first detected between $M_\infty = 0.700$ and 0.794 (the sonic line is shown as a dashed line in the figures) and a shock emanating from the corner appears in the supersonic zone at $M_\infty = 0.794$. As the Mach number was increased, this zone grew larger and a shock appeared at the rear of it, while the shock emanating from the corner weakened and disappeared. This rearward shock was of the typical λ type associated with a laminar boundary layer, and the interferograms clearly indicated the separation of the boundary layer ahead of this shock. The similarity between the flow field at $M_\infty = 0.892$ and at $M_\infty = 1.207$ (Figs. 10 and 11) is striking; the base of the rearward shock has moved quite far back on the wake of the blunt trailing edge at $M_\infty = 1.207$ but in the vincinity of and ahead of the sonic line the two fields are nearly identical except for the detached shock wave which appears about 1 1/2 chord lengths ahead of the wedge at $M_\infty = 1.207$. As the Mach number was increased above 1.207, the detached shock moved in closer to the leading edge and finally "attached" at a Mach number quite close to the theoretical

attachment Mach number of $M_\infty = 1.418$. Notice that the process of attachment is very continuous. The effect of the boundary layer is quite noticeable in the last few interferograms: this can be roughly accounted for by considering the boundary layer to change the shape of the body by its displacement thickness, then considering a non-viscous flow past this revised shape. On the wedge the boundary layer will not grow as rapidly as on a flat plate due to the favorable pressure gradient and, in fact, the effect of the strong expansion around the corner is known to cause an almost complete collapse of the boundary layer there. As the bow shock wave gets close to attachment the velocities in the subsonic region behind it are getting very close to sonic velocity and hence the flow in this region is very sensitive to any slight curvature of the "revised shape" of the wedge. This accounts for the shift of the base of the sonic line forward to the leading edge as the shock approaches attachment. The non-viscous theory would indicate that the sonic line would always begin at the corner and, at a Mach number just slightly above the shock attachment Mach number, the whole subsonic region would become sonic; then, with increasing Mach number, the flow behind the shock would be completely supersonic. As observed, the boundary layer effect is to make the wedge have a curved surface and the sonic line actually moves slowly from the corner to the nose. Even with attached shock wave at $M_\infty = 1.465$ the flow behind the shock is not quite uniform (as non-viscous theory would indicate it should be) due to the effective curved surface caused by the boundary layer.

2. Local Mach Number Distributions on the Three Thin Wedges

Figs. 16 through 18 show the variation of local Mach number distribution on the surfaces of the 4 1/2°, 7 1/2°, and 10° semi-angle wedges with free stream Mach number. This should be compared with Fig. 5 which shows the corresponding theoretical curve in terms of the transonic similarity parameters. The general behavior of the theoretical and experimental curves is quite definitely in good agreement. Particularly noteworthy is the slow variation of the local Mach number distribution near free stream Mach number one.

3. Pressure Coefficient Distributions on the Three Thin Wedges

The slow variation of the Mach number distribution in the range near $M_\infty = 1$ is obscured when the results are plotted in terms of pressure coefficient, since the pressure coefficient changes a great deal if local Mach number is constant while free stream Mach number changes. A better parameter for presenting transonic pressure distributions would be p/p_o (p/p_o' in case of detached shock). Typical C_p distributions are shown in Figs. 17 and 18 for the 7 1/2° wedge (the results for the 10° and 4 1/2° wedges were very similar and hence they are not presented). The points shown were where the fringes intersected the body in the interferograms. Since for a wedge the drag coefficient is proportional to the average C_p , the drag rise is evident in the subsonic distributions as the point where $C_p = 0$ moves rearward with increasing free stream Mach number. Linearized subsonic theory (which predicts $C_D = 0$) locates the $C_p = 0$ point at x/c = 50%. Fig. 7 shows theoretical reduced C_p distributions at various reduced free

stream Mach numbers. Again the qualitative agreement of these curves with experiment is evident.

4. Shock Detachment Distance for the Three Thin Wedges

Fig. 21 shows the shock detachment distance versus reduced free stream Mach number for the three thin wedges and includes the theoretical values from Ref. 22. Here Vincenti and Wagoner's values for ξ_{∞} have been multiplied by $\frac{\xi_{\infty A}|_{\theta = 7\frac{1}{2}^{\circ}}}{\xi_{\infty A}|_{\theta=0^{\circ}}}$ * in order to make the transonic perturbation value of detachment reduced Mach number agree with the value from oblique shock theory for the 7 1/2° wedge: the reason for this was discussed in Section VI, namely the difficulty of comparing transonic perturbation theory quantitatively with experiment. Notice how rapidly the shock wave moves away from the wedge as Mach number is decreased toward one.

5. Drag Coefficient Variation with Mach Number for the Three Thin Wedges

It was shown in Ref. 1 that the viscous effects on the wedge tend to compensate each other at the leading edge and the shoulder so that the over-all pressure drag is nearly the same as if the flow were inviscid. Thus it would be expected that the pressure drag coefficients obtained by integrating the experimental pressure distributions would check the inviscid transonic perturbation theory. The reduced

*In terms of Mach number, for the 7 1/2° wedge the shock theory predicts attachment at $M_{\infty A} = 1.33$ ($\xi_{\infty A} = 1.68$) while the transonic perturbation theory predicts $M_{\infty A} = 1.25$ ($\xi_{\infty A} = 1.19$).

drag coefficient used here was

$$\tilde{C}_D = \int_0^1 \tilde{C}_p \, d\left(\frac{x}{c}\right) \tag{60}$$

which is, in essence, the reduced drag coefficient of the upper (or lower) half wedge. This was done since the wedge model was regarded as the front half of a double wedge profile and hence the value given here is the part of the reduced drag coefficient contributed by the front half of such an airfoil (C_{D_F} as on Eq. (42), page 32), based on the chord of the double wedge profile, which would be twice the chord of the model used here. Of course, this viewpoint is valid only for supersonic free stream Mach numbers.

Fig. 22 shows the reduced drag coefficients for the three thin wedges plotted versus reduced Mach number. It is seen that the results give nearly a universal curve, which they should if the transonic similarity law is true, but that there are systematic variations with wedge angle. This is to be expected based on the discussion of Section VI. The vertical lines thru the experimental points indicate estimated accuracy of the data. This figure should be compared with Fig. 8, the theoretical reduced drag coefficient variation with reduced Mach number. It is obvious that the qualitative agreement of theory and experiment is good. In Fig. 23 the theory and experiment are compared directly for the three thin wedges. Here the theoretical drag coefficients are shown with a vertical spread, the upper values for $M_\infty > 1$ corresponding to the use of the pressure coefficient $C_p = \frac{-2(u-u_\infty)}{a^*}$ and the lower values to the use of the pressure coefficient $C_p = \frac{-2(u-u_\infty)}{U}$. The situation is vice versa for $M_\infty < 1$. From

this figure it is evident that the transonic perturbation theory gives a good approximation to experiment.

6. Flow Field at $M_\infty = 1.44$ for the 26.6° Wedge

Fig. 24 shows the experimental and theoretical constant velocity lines in the subsonic region behind the detached shock wave for a 26.57° semi-angle wedge at $M_\infty = 1.44$. The theoretical analysis was made using relaxation calculations by J. Drebinger (Ref. 20) using the flow equations with entropy variation behind the shock taken into account. The experimental constant velocity lines were determined from the isopycnic lines of the interferogram by taking into account the lateral stagnation pressure gradient behind the curved shock. The isopycnic lines near this strong shock wave were probably slightly in error due to the "smearing out" of the pressure discontinuity across the shock in the side wall boundary layers. It is seen that the agreement between theory and experiment on detachment distance and constant velocity contours near the wedge is good.

Fig. 25 shows the surface pressure distribution from Ref. 18 and the present experiments. Again it is seen that the agreement is good.

7. Flow Field Near the 8.8% Circular Arc Section

Figs. 26 through 32 show interferograms of the flow past the 8.8% circular arc section for fourteen Mach numbers from 0.718 to 0.936 and 1.11 to 1.500.

Supersonic velocity first occurred at $M_\infty = 0.825$ (see page 27) and in Fig. 27 a nearly symmetric supersonic zone is shown at

$M_\infty = 0.848$. No shock waves were apparent in this zone although a sensitive schlieren apparatus might have shown some weak shocks there. At $M_\infty = 0.890$ the supersonic zone has grown rapidly and now terminates in the λ -shock configuration. Further increase of Mach number to $M_\infty = 0.935$ (Fig. 28) shows the supersonic zone increasing laterally and the terminating shock moving rearward into the wake of the body. Fig. 28 also shows the density distribution at $M_\infty \doteq 1.11$ (the detached shock wave was just out of the field of view of the interferometer) and it is interesting to note the similarity between the flow field at $M_\infty = 0.935$ and $M_\infty \doteq 1.11$. It would appear as though the shock terminating the supersonic zone at $M_\infty = 0.935$ had moved rearward to form the trailing edge shock (which is actually in the wake here due to the blunt trailing edge) and the supersonic zone had grown laterally until the sonic line joined with the detached shock far away from the body at $M_\infty = 1$, thus causing an embedded subsonic zone in the supersonic flow with further increase in Mach number.

With further increase of Mach number above $M_\infty = 1.11$, Figs. 29 through 32 show that the detached shock again approached the leading edge and the embedded subsonic zone decreased in size until finally the shock "attached" somewhere between $M_\infty = 1.400$ and $M_\infty = 1.450$ (the theoretical value being $M_{\infty_A} = 1.423$).

8. Local Mach Number Distributions on the 8.8% Circular Arc Section

Fig. 33 shows the local Mach number distributions for the 8.8% circular arc section as obtained from the experiments at various free stream Mach numbers. Again it is apparent that the variation of

local Mach number distribution near $M_\infty = 1$ is very slow, and indeed, the distribution for $M_\infty = 1$ could be interpolated from this figure with good accuracy.

Fig. 34 is a cross-plot of the data of Fig. 33 except that here the data are given in transonic similarity parameters. This figure shows contours of constant reduced local Mach number on a reduced free stream Mach number versus chordwise position curve. The dotted lines represent subsonic local Mach numbers, the solid lines supersonic local Mach numbers. Note again the slow variation of local Mach number distribution with free stream Mach number near sonic velocity.

9. Pressure Coefficient Distributions on the 8.8% Circular Arc Section

Figs. 35 and 36 show the pressure coefficient distributions on the 8.8% circular arc section for various free stream Mach numbers. The points shown are where the fringes intersected the body in the interferogram. Again the presentation in this manner obscures the interesting fact observed in Fig. 33.

10. Drag Coefficient Variation with Mach Number for the 8.8% Circular Arc Section

Fig. 37 shows the experimental determination of the drag coefficient of the front part of the 8.8% circular arc section. This again is of the nature of a fore-drag coefficient, and, as shown in Eq. (43), it should have a positive slope equal to $\frac{4}{\gamma+1}\frac{t}{c} - \frac{2}{\gamma+1} C_D|_{M_\infty=1}$ at $M_\infty = 1$; this is how the subsonic data has been joined with the

supersonic data. The vertical lines through the experimental points again indicate estimated accuracy of the data. For the case of attached shock the pressure distribution can be calculated using characteristics theory and the shock polar; however, a close approximation is obtained by considering the flow behind the shock wave to be Prandtl-Meyer flow (this yields, approximately, parabolic shaped bow and trailing edge shock waves, see Ref. 34). From this pressure distribution the drag was calculated and is shown in Fig. 37. Taking into account the "reflected" characteristics from the shock wave would give more compression and increase the drag coefficient so that it would agree better with the experimental values at $M_\infty = 1.450$ and 1.500 shown in Fig. 37.

Note that the tests were made at low enough supersonic speeds to definitely get below the drag coefficient maximum at $M \doteq 1.20$.

11. Local Mach Number Distributions on a 12% Biconvex Circular Arc Airfoil

Fig. 36 shows local Mach number distributions from Ref. 9 for high subsonic speed flow over a 12% biconvex circular arc airfoil (with turbulent boundary layer). The data for the 8.8% circular arc section at two supersonic speeds have been scaled according to the transonic similarity laws to the 12% case and are shown for the front half of the 12% airfoil in Fig. 38. The back half for these two cases has been faired in using a Prandtl-Meyer expansion which should be approximately correct (a more accurate determination could have been made using characteristic theory and the shock polar). At $M_\infty = 1.58$,

the theory indicates that the shock is attached with sonic speed just behind the shock on the leading edge, so that the distribution can be obtained by standard methods mentioned above; again the Prandtl-Meyer expansion approximation was used for the distribution at $M_\infty = 1.58$ on Fig. 38.

The behavior of the Mach number distribution is similar to those shown previously, except in this case the movement of the shock terminating the local supersonic zone is shown. Apparently little change in local Mach number distribution occurs between $M_\infty = 0.936$ and $M_\infty = 1.29$.

12. Drag Coefficient Variation with Mach Number for a 12% Biconvex Circular Arc Airfoil

The data of Fig. 39 were converted to pressures which were integrated to give the pressure drag coefficient for the various free stream Mach numbers. In addition the drag of the front and back halves are shown separately. The drag coefficient variation between $M_\infty = 0.96$ and $M_\infty = 1.20$ was based on constant local Mach number distribution at values interpolated between the curves for $M_\infty = 0.936$ and $M_\infty = 1.29$. The data were faired into the curves for attached shock wave calculated on the Prandtl-Meyer expansion basis. It is seen that the fore-drag coefficient has a maximum after $M_\infty = 1$ while the drag coefficient of the rear part has a maximum before $M_\infty = 1$. The overall airfoil has a maximum drag coefficient just before $M_\infty = 1$ in order for the curve to have the slightly negative slope at $M_\infty = 1$ given by Eq. (41), page 32.

VIII. CONCLUSIONS

The transonic similarity theory of von Kármán and Guderley was checked and found to be in good agreement with experiment for thin wedge profiles near $M_\infty = 1$.

The results of theoretical calculations using transonic perturbation theory made by Guderley and Yoshihara, Vincenti and Wagoner, and Cole for a wedge in transonic flow were checked experimentally at high subsonic and low supersonic speeds for three wedges of different angles and were found to be in good agreement with experiment.

The flow field and the surface pressure distribution for a 26.6° semi-angle wedge at $M_\infty = 1.44$ were obtained experimentally and were found to be in excellent agreement with the theoretical calculations of this flow made by Drebinger.

The pressure distributions and drag coefficients for an 8.8% circular arc section followed by a straight section and for a 12% biconvex circular arc airfoil were presented completely through the transonic range. It was shown that some difficulty arises in comparing two-dimensional transonic perturbation theory with experiment, since this theory neglects terms of order $(t/c)^{2/3}$ and higher; for even moderate thickness ratios this will cause noticeable deviations from more exact theory.

It was shown from some physical arguments that the local Mach number distribution on bodies traveling through an infinite fluid has a stationary value at $M_\infty = 1$. This was verified experimentally for the case of two-dimensional flow. It was shown that this concept implies a drag coefficient maximum just below $M_\infty = 1$ for all bodies in

steady flight. This fact can be used to obtain the variation of local Mach number distribution on bodies completely through the transonic range of velocities from wind tunnel tests, provided small models are used so that tests can be carried well above critical Mach number and to low enough supersonic Mach numbers so that the bow shock wave is detached a chord length or so.

REFERENCES

1. Liepmann, H. W. and Bryson, A. E. Jr.: Transonic Flow Past Wedge Sections. Jour. Aero. Sci., Vol. 17, No. 12, Dec. 1950, pp. 745-755.

2. Weaver, J. H.: A Method of Wind Tunnel Testing Through the Transonic Range. Jour. Aero. Sci., Vol. 15, No. 1, Jan. 1948, pp. 28-34.

3. Ackeret, J., Feldman, F. and Rott, N.: Investigations of Compression Shocks and Boundary Layers in Gases Moving at High Speeds. NACA T.M. 1113, Jan. 1947.

4. Liepmann, H. W.: The Interaction Between Boundary Layer and Shock Waves in Transonic Flow. Jour. Aero. Sci., Vol. 13, No. 12, Dec. 1946, pp. 623-637.

5. Guderley, G.: On the Transition from a Transonic Potential Flow to a Flow with Shocks. U.S.A.F. A.M.C. Tech. Report No. F-TR-2160-ND, 1947.

6. Ferri, A.: Elements of Aerodynamics of Supersonic Flows. The MacMillan Co., New York, 1949.

7. Sears, W. R.: Transonic Potential Flow of a Compressible Fluid. Jour. Appl. Phys., Vol. 21, No. 8, Aug. 1950, pp. 771-778.

8. Kuo, Y. H.: On the Stability of Two-Dimensional Smooth Transonic Flows. Jour. Aero. Sci., Vol. 18, No. 1, Jan. 1951.

9. Liepmann, H. W., Ashkenas, H. I. and Cole, J. D.: Experiments in Transonic Flow. U.S.A.F. A.M.C. Tech. Report No. 5667, 1948.

10. von Kármán, Th.: The Similarity Law of Transonic Flow. Jour. Math. and Phys., Vol. 26, 1947, pp. 182-190.

11. Busemann, A.: Analytical Methods for Treating Detached Shock Waves. NACA T.N. 1858.

12. Busemann, A.: The Drag Problem at High Subsonic Velocities. Jour. Aero. Sci., Vol. 16, No. 6, 1949, pp. 337-344.

13. Guderley, G.: Considerations of the Structure of Mixed Subsonic-Supersonic Flow Patterns. U.S.A.F. A.M.C. Tech. Report No. F-TR-2168-ND, 1947.

14. Guderley, G.: Singularities at the Sonic Velocity. U.S.A.F. A.M.C. Tech. Report No. F-TR-1171-ND, 1948.

15. Frankl, F.: On the Problems of Chaplygin for Mixed Sub- and Supersonic Flows. NACA T.M. 1155, 1947.

16. Maccoll, J. W. and Codd, J.: Theoretical Investigations of the Flow Around Various Bodies in the Sonic Region of Velocities. Theo. Res. Report No. 17/45, Armament Res. Dept., British Ministry of Supply, Sept. 1945.

17. Emmons, H. W.: Theoretical Flow of a Frictionless Adiabatic Perfect Gas Inside a Two-Dimensional Hyperbolic Nozzle. NACA T.N. 1003, May 1946.

18. Emmons, H. W.: Flow of a Compressible Fluid Past a Symmetrical Airfoil in a Wind Tunnel and Free Air. NACA T.N. 1746, Nov. 1948.

19. Drougge, G.: The Flow Around Conical Tips in the Upper Transonic Range. Report No. 25, Aero. Res. Inst. of Sweden (stockholm), 1948.

20. Drebinger, J. W.: Detached Shock Waves. Ph.D. Thesis, Harvard University, May 1950.

21. Guderley, G. and Yoshihara, H.: The Flow Over a Wedge Profile at Mach Number One. Jour. Aero. Sci., Vol. 17, No. 11, pp. 723-736, Nov. 1950.

22. Vincenti, W. G. and Wagoner, C. B.: Transonic Flow Past a Wedge Profile with Detached Bow Wave. NACA T.N. 2339, 1951.

23. Cole, J. D.: Drag of a Finite Wedge at High Subsonic Speeds. To be published in Jour. Math. and Phys.

24. Pack, D. C.: Investigations of the Flow Past Finite Wedges at 20 Degree and 40 Degree Apex Angle at Subsonic and Supersonic Speeds Using a Mach-Zehnder Interferometer. British R. and M. No. 2321, 1949.

25. Griffith, W. C.: Transonic Flow. Princeton Univ. Dept. of Phys., Project NR 061-020, Contract N6-ori-105, Task II, Tech. Report II-7, Dec. 1950.

26. Dhawan, S. and Roshko, A.: A Flexible Nozzle for a Small Supersonic Wind Tunnel. Jour. Aero. Sci., Vol. 18, No. 4, April 1951.

27. Ashkenas, H. I.: Design and Construction of a Mach-Zehnder Interferometer for Use with the GALCIT Transonic Wind Tunnel. A.E. Thesis, Calif. Inst. of Tech., 1949.

28. Ashkenas, H. I. and Bryson, A. E.: Design and Performance of a Simple Interferometer for Wind Tunnel Measurements. Jour. Aero. Sci., Vol. 18, No. 2, Feb. 1951, pp. 82-91.

29. Maccoll, J. W.: Investigations of Flow at Sonic Speeds. Paper read at Sixth Int. Cong. of App. Mech. Paris, 1946 (unpublished).

30. Tsien, H. S. and Baron, J.: Airfoils in Slightly Supersonic Flow. Jour. Aero. Sci., Vol. 16, No. 1, Jan. 1949, pp. 55-61.

31. Graham, D. J., Nitzberg, G. E. and Olson, R. N.: A Systematic Investigation of Pressure Distributions at High Speeds Over Five Representative NACA Low-Drag and Conventional Airfoil Sections. NACA TR 832, 1945.

32. Nitzberg, G. E. and Crandall, S.: A Study of Flow Changes Associated with Airfoil Section Drag Rise at Supercritical Speeds. NACA T.N. 1813, Feb. 1949.

33. Nagamatsu, H. T.: Theoretical Investigation of Detached Shock Waves. Ph.D. Thesis, Calif. Inst. of Tech., 1949.

34. Liepmann, H. W.: On the Relation Between Drag and Entropy. Douglas Aircraft Report SM-13726, 1950.

APPENDIX 1

ASYMPTOTIC REPRESENTATION OF COLE'S SOLUTION FOR LARGE NEGATIVE VALUES OF REDUCED FREE STREAM MACH NUMBER

Cole's solution for the high subsonic velocity flow past a thin wedge (Ref. 23) is given as follows (in Cole's notation)

$$y(z,v;z_1) = \left(\frac{2zz_1}{3}\right)^{1/3} V_0 \int_0^\infty \frac{\sinh \lambda (V_0 - V)}{\sinh \lambda V_0} J_{-1/3}(\lambda z) J_{-1/3}(\lambda z_1) \lambda d\lambda \qquad (61)$$

$$x(z,v;z_1) = 1 - z_1^{1/3} z^{2/3} V_0 \int_0^\infty \frac{\cosh \lambda (V_0 - V)}{\sinh \lambda V_0} J_{2/3}(\lambda z) J_{-1/3}(\lambda z_1) \lambda d\lambda \qquad (62)$$

where the centerline of the wedge is at $y = 0$, leading edge at $x = 0$, shoulder at $x = 1$, and

$$z = \frac{2}{3}(1-M_\infty^2)^{3/2} = \frac{2}{3}\left[-(\gamma+1)\frac{u}{a^*}\right]^{3/2}$$

$$z_1 = \frac{2}{3}(1-M_\infty^2)^{3/2} = \frac{2}{3}\left[-(\gamma+1)\frac{u_\infty}{a^*}\right]^{3/2} \qquad (63)$$

$$V_0 = (\gamma+1)\theta$$

and other notation is the same as the present paper.

Using the standard methods of partial fraction expansion we may write

$$\frac{\sinh \lambda (V_0 - V)}{\sinh \lambda V_0} = 1 - \frac{V}{V_0} + 2\sum_{n=1}^{\infty} \sin\left(n\pi \frac{V}{V_0}\right) \frac{\lambda^2 V_0^2}{\lambda^2 V_0^2 + n^2\pi^2} \qquad (64)$$

$$\frac{\cosh \lambda (V_0 - V)}{\sinh \lambda V_0} = \frac{1}{\lambda V_0} + 2\sum_{n=1}^{\infty} \cos\left(n\pi \frac{V}{V_0}\right) \frac{\lambda V_0}{\lambda^2 V_0^2 + n^2\pi^2} \qquad (65)$$

Substituting these into the integrals above and making use of the integrals

$$\int_0^\infty \frac{\lambda^3}{\lambda^2+\alpha^2} J_{-1/3}(\lambda\beta) J_{-1/3}(\lambda\gamma)\, d\lambda = \begin{cases} -\alpha^2 I_{-1/3}(\alpha\gamma) K_{-1/3}(\alpha\beta) & ; \beta > \gamma > 0 \\ -\alpha^2 K_{1/3}(\alpha\gamma) I_{-1/3}(\alpha\beta) & ; \gamma > \beta > 0 \end{cases} \tag{66}$$

and

$$\int_0^\infty \frac{\lambda^2}{\lambda^2+\alpha^2} J_{-1/3}(\lambda\beta) J_{2/3}(\lambda\gamma)\, d\lambda = \begin{cases} -\alpha^2 I_{2/3}(\alpha\gamma) K_{-1/3}(\alpha\beta) & ; \beta > \gamma > 0 \\ \alpha K_{2/3}(\alpha\gamma) I_{-1/3}(\alpha\beta) & ; \gamma > \beta > 0 \end{cases} \tag{67}^*$$

We can write Eqs. (61) and (62) as

$$\tilde{y} = v_0^{1/3} y = \begin{cases} 2\left(\frac{2}{3}\frac{z}{v_0}\frac{z_1}{v_0}\right)^{1/3} \sum_{n=1}^{\infty} n\pi \sin\left(n\pi\frac{v}{v_0}\right) I_{-1/3}\left(n\pi\frac{z}{v_0}\right) K_{-1/3}\left(n\pi\frac{z_1}{v_0}\right) ; z_1 > z > 0 \\ 2\left(\frac{2}{3}\frac{z}{v_0}\frac{z_1}{v_0}\right)^{1/3} \sum_{n=1}^{\infty} n\pi \sin\left(n\pi\frac{v}{v_0}\right) K_{-1/3}\left(n\pi\frac{z}{v_0}\right) I_{-1/3}\left(n\pi\frac{z_1}{v_0}\right) ; z > z_1 > 0 \end{cases} \tag{68}$$

$$\chi = \begin{cases} 1 + 2\left(\frac{z_1}{v_0}\right)^{1/3}\left(\frac{z}{v_0}\right)^{2/3} \sum_{n=1}^{\infty} n\pi \cos\left(n\pi\frac{v}{v_0}\right) I_{2/3}\left(n\pi\frac{z}{v_0}\right) K_{-1/3}\left(n\pi\frac{z_1}{v_0}\right) ; z_1 > z > 0 \\ -2\left(\frac{z_1}{v_0}\right)^{1/3}\left(\frac{z}{v_0}\right)^{2/3} \sum_{n=1}^{\infty} n\pi \cos\left(n\pi\frac{v}{v_0}\right) K_{2/3}\left(n\pi\frac{z}{v_0}\right) I_{-1/3}\left(n\pi\frac{z_1}{v_0}\right) ; z > z_1 > 0 \end{cases} \tag{69}^{**}$$

Making use of the asymptotic formulae

$$I_\nu(z) \cong \frac{1}{\sqrt{2\pi z}} e^z + \cdots \quad \text{as} \quad z \to \infty \tag{70}$$

$$K_\nu(z) \cong \sqrt{\frac{\pi}{2z}} e^{-z} + \cdots \quad \text{as} \quad z \to \infty \tag{71}$$

and the simple summations

$$\sum_{n=1}^{\infty} e^{-an} \sin n\pi x = \frac{\sin \pi x}{2\cosh a - 2\cos \pi x} \tag{72}$$

$$\sum_{n=1}^{\infty} e^{-an} \cos n\pi x = \frac{\cos \pi x - e^{-a}}{2\cosh a - 2\cos \pi x} \tag{73}$$

---

*G. N. Watson "Bessel Functions," Cambridge Univ. Press for Eq. (67). Eq. (66) is obtained by differentiation of Eq. (67) with respect to γ.

**Figs. 5, 6 and 7 were calculated from this equation for $v = 0$, for the cases $\xi_\infty \leq 0$.

we can write Eqs. (68) and (69) for large values of z and z_1 as

$$\tilde{y} \cong \frac{1}{2}\left(\frac{2}{3}\right)^{1/3}\left(\frac{z}{V_0}\,\frac{z_1}{V_0}\right)^{-1/6} \frac{\sin \pi \frac{v}{V_0}}{\cosh \frac{\pi (z-z_1)}{V_0} - \cos \pi \frac{v}{V_0}} \quad ; \quad z, z_1 \to \infty \tag{74}$$

$$\chi \cong \begin{cases} 1 + \frac{1}{2}\left(\frac{z}{z_1}\right)^{1/6} \dfrac{\cos \pi \frac{v}{V_0} - e^{\frac{+\pi (z-z_1)}{V_0}}}{\cosh \frac{\pi (z-z_1)}{V_0} - \cos \pi \frac{v}{V_0}} & ; \quad z_1 > z \to \infty \\ -\frac{1}{2}\left(\frac{z}{z_1}\right)^{1/6} \dfrac{\cos \pi \frac{v}{V_0} - e^{\frac{-\pi (z-z_1)}{V_0}}}{\cosh \frac{\pi (z-z_1)}{V_0} - \cos \pi \frac{v}{V_0}} & ; \quad z > z_1 \to \infty \end{cases} \tag{75}$$

Eliminating v between Eqs. (74) and (75) for $z_1 > z \to \infty$ we find

$$\left[\frac{y}{\left(\frac{z}{z_1}\right)^{1/6} 2\left(\frac{3z_1}{2}\right)^{1/3} \sinh \frac{\pi (z-z_1)}{V_0}}\right]^2 + \left[\frac{\chi + \frac{\left(\frac{z}{z_1}\right)^{1/6} e^{\frac{-\pi (z-z_1)}{V_0}}}{2 \sinh \frac{\pi (z-z_1)}{V_0}}}{\frac{\left(\frac{z}{z_1}\right)^{1/6}}{2 \sinh \frac{\pi (z-z_1)}{V_0}}}\right]^2 = 1 \tag{76}$$

and for $z > z_1 \to \infty$ simply replace χ by $\chi - 1$, and $z - z_1$ by $z_1 - z$ in Eq. (76). Thus the lines of constant Mach number are ellipses with center on $y = 0$, with ratio of semi-axes equal to

$$\left(\frac{3z_1}{2}\right)^{1/3} = \sqrt{1 - M_\infty^2} \tag{77}$$

which is precisely the solution given by the linearized subsonic theory (see Appendix 2).

Now, in the notation of the present paper

$$\frac{\pi (z-z_1)}{V_0} = \frac{2\pi}{3}\left[(-\xi)^{3/2} - (-\xi_\infty)^{3/2}\right]$$

and since $\xi - \xi_\infty$ is small on the wedge and since

$$\tilde{C}_p = -2(\xi - \xi_\infty)$$

we can write that

$$\frac{\pi(z-z_1)}{V_0} = \frac{2\pi}{3}(-\xi_\infty)^{3/2}\left[\left\{1 - \frac{\tilde{C}_p}{2(-\xi_\infty)}\right\}^{3/2} - 1\right]$$

hence,

$$\frac{\pi(z-z_1)}{V_0} = \frac{2\pi}{3}(-\xi_\infty)^{3/2}\left[\left\{1 - \frac{3}{4}\frac{\tilde{C}_p}{(-\xi_\infty)} + \cdots\right\} - 1\right]$$

so, approximately

$$\frac{\pi(z-z_1)}{V_0} \doteq -\frac{\pi}{2}(-\xi_\infty)^{1/2}\tilde{C}_p = -\frac{\pi}{2}\frac{C_p\sqrt{1-M_\infty^2}}{\theta} \quad ; \quad z, z_1 \to \infty \qquad (78)$$

Similarly, for large z and z_1 it follows that

$$\left(\frac{z}{z_1}\right)^{1/6} \doteq 1 \quad ; \quad z, z_1 \to \infty \quad \text{for} \quad z - z_1 \text{ small} \qquad (79)$$

Substituting Eq. (78) and (79) into Eq. (16) we get the exact linearized subsonic solution for constant velocity lines (see Appendix 2). Therefore on the wedge ($y = 0$), from Eqs. (76), (78), and (79), we have approximately for large z and z_1

$$\chi + \frac{1}{e^{\pi\sqrt{-\xi_\infty}\,\tilde{C}_p} - 1} = \pm \frac{1}{e^{\frac{\pi}{2}\sqrt{-\xi_\infty}\,\tilde{C}_p} - e^{-\frac{\pi}{2}\sqrt{-\xi_\infty}\,\tilde{C}_p}}$$

Solving this for $\tilde{C}_p$ we find

$$\tilde{C}_p\sqrt{-\xi_\infty} = -\frac{2}{\pi}\log\frac{1-\chi}{\chi}$$

or

$$C_p = \frac{-2\theta}{\pi\sqrt{1-M_\infty^2}}\log\frac{\chi}{\chi-1} \qquad (80)$$

which is precisely the linearized subsonic solution for flow past a wedge (see Appendix 2). Thus Cole's solution far away from $M_\infty = 1$ tends exactly to the linearized subsonic solution.

APPENDIX 2

LINEARIZED SUBSONIC AND SUPERSONIC FLOW PAST WEDGE AND CIRCULAR ARC SECTIONS

1. Linearized Subsonic Flow Past a Wedge

Let the wedge centerline be on $y = 0$, with leading edge at $x = 0$, shoulder at $x = c$. Then the incompressible flow problem is to find an analytic function $u - iv$ such that $v = 0$ on $y = 0$ except for $0 < x < c$ where $v = U\theta$ and $u - iv = 0$ at infinity. Such a function is

$$u - iv = \frac{U\theta}{\pi} \log \frac{z/c}{(z/c) - 1} \tag{81}$$

where

$z = x + iy$

U = free stream velocity

Thus on $y = 0$,

$$C_{p_0} = \frac{-2u}{U} = \frac{-2\theta}{\pi} \log \frac{x/c}{1 - (x/c)} \tag{82}$$

Using the Prandtl-Glauert transformation, for linearized subsonic flow we have

$$C_p = \frac{C_{p_0}}{\sqrt{1 - M_\infty^2}} = \frac{-2\theta}{\pi \sqrt{1 - M_\infty^2}} \log \frac{x/c}{1 - (x/c)} \tag{83}$$

or in transonic similarity notation

$$\tilde{C}_p = \frac{-2}{\pi \sqrt{-\xi_\infty}} \log \frac{x/c}{1 - (x/c)} \tag{84}$$

For the incompressible case the lines of constant pressure in the fluid will be where

$$\frac{z/c}{(z/c)-1} = \text{constant}$$

but these are circles with centers at

$$x = \frac{e^{\frac{-\pi C_p}{\theta}}}{1-e^{\frac{-\pi C_p}{\theta}}} \quad , \; y = 0 \tag{85}$$

and radii

$$\frac{e^{\frac{-\pi}{2}\frac{C_p}{\theta}}}{1-e^{\frac{-\pi C_p}{\theta}}}$$

In the Prandtl-Glauert Transformation, the y distance is stretched by the factor $\sqrt{1-M_\infty^2}$ as is the pressure coefficient so the lines of constant pressure (and hence density) are ellipses with ratio of axes equal to $\sqrt{1-M_\infty^2}$ given by the equation

$$\left[\frac{y}{\frac{1}{2\sqrt{1-M_\infty^2}\,\sinh\frac{\pi}{2}\frac{C_p\sqrt{1-M_\infty^2}}{\theta}}}\right]^2 + \left[\frac{x + \frac{e^{\frac{\pi C_p\sqrt{1-M_\infty^2}}{2\theta}}}{2\sinh\frac{\pi C_p\sqrt{1-M_\infty^2}}{2\theta}}}{\frac{1}{\sinh\frac{\pi}{2}\frac{C_p\sqrt{1-M_\infty^2}}{\theta}}}\right]^2 = 1 \tag{86}$$

2. Linearized Supersonic Flow Past a Wedge

From the Ackeret theory the pressure coefficient in supersonic flow is proportional to slope and for the wedge yields simply

$$C_p = \frac{2\theta}{\sqrt{M_\infty^2 - 1}} \tag{87}$$

or

$$\tilde{C}_p \cong \frac{2}{\sqrt{\xi_\infty}} \tag{88}$$

3. Linearized Subsonic Flow Past a Circular Arc Section

For the circular arc section, the slope of the surface varies almost linearly with distance from the zero slope point along the axis of the profile. For the section shown in Fig. 1 then, with centerline on $y=0$, leading edge at $x=0$, and zero slope point at $x=c$, the incompressible flow problem is again to find an analytic function $u-iv$ such that on $y=0$, $v=0$ except for $0<x<c$ where $v = 2U\frac{t}{c}(1-\frac{x}{c})$ where t is the half thickness at $x=c$ and $u-iv=0$ at infinity. Such a function is

$$u-iv = -\frac{2U}{\pi}\frac{t}{c}\left[\left(\frac{z}{c}-1\right)\log\frac{z/c}{(z/c)-1}-1\right] \tag{89}$$

On the wedge ($y=0$, $0<x<c$), then

$$C_{p_0} = -\frac{2u}{U} = -\frac{4}{\pi}\frac{t}{c}\left[\left(1-\frac{x}{c}\right)\log\frac{x/c}{1-(x/c)}+1\right] \tag{90}$$

so the linearized subsonic solution is

$$C_p = \frac{-\frac{4}{\pi}\frac{t}{c}}{\sqrt{1-M_\infty^2}}\left[\left(1-\frac{x}{c}\right)\log\frac{x/c}{1-(x/c)}+1\right] \tag{91}$$

or

$$\tilde{C}_p = \frac{4}{\pi\sqrt{-\xi_\infty}}\left[\left(1-\frac{x}{c}\right)\log\frac{x/c}{1-(x/c)}+1\right] \tag{92}$$

The minimum C_p is obtained by differentiation, and one finds that

$$\frac{dC_p}{d(x/c)} = 0 \qquad \text{at the point where} \quad \log\frac{x/c}{1-(x/c)} = \frac{1}{x/c}$$

and numerically the solution of this transcendental equation is

$$\frac{x}{c} = 0.783 \tag{93}$$

which gives

$$C_{P_{MIN}} = \frac{-1.626\,(t/c)}{\sqrt{1-M_\infty^2}} \tag{93}$$

4. Linearized Supersonic Flow Past a Circular Arc Section

The result here is again simple from the Ackeret theory:

$$C_p = \frac{4\,(t/c)}{\sqrt{M_\infty^2-1}}\left(1-\frac{x}{c}\right) \tag{94}$$

or

$$\tilde{C}_p = \frac{4}{\sqrt{\xi_\infty}}\left(1-\frac{x}{c}\right) \tag{95}$$

APPENDIX 3

TRANSONIC SHOCK POLAR

The equation of the shock polar in the hodograph plane is

$$\bar{v}^2 = (U-\bar{u})^2 \frac{\frac{\bar{u}}{a^*} - \frac{a^*}{U}}{\frac{a^*}{U} + \frac{2}{\gamma+1}\frac{U}{a^*} - \frac{\bar{u}}{a^*}} \tag{96}$$

where U is the velocity ahead of the shock and $\bar{u}$, $\bar{v}$ are velocity components behind the shock parallel and perpendicular to the direction of U respectively. Making the transonic approximation in this equation we let

$$\begin{aligned} \bar{u} &= a^* + u \\ \bar{v} &= v \\ U &= a^* + u_\infty \end{aligned} \tag{97}$$

and substituting into Eq. (96), neglecting higher powers of the perturbation velocities one obtains

$$v^2 = \frac{\gamma+1}{2}(u_\infty - u)^2 \left(\frac{u}{a^*} + \frac{u_\infty}{a^*}\right) \tag{98}$$

Letting

$$\begin{aligned} u' &= (\gamma+1)\frac{u}{a^*} \\ v' &= (\gamma+1)\frac{v}{a^*} \end{aligned} \tag{99}$$

we then have

$$2(v')^2 = (u'_\infty - u')^2 (u' + u'_\infty) \tag{100}$$

The wedge angle for detachment of the shock will now be given by the maximum value of v' . This is easily seen to occur at $u' = -\frac{1}{3}u'_\infty$ giving $v'_{MAX} = \frac{4}{9}\sqrt{3}\, u_\infty^{3/2}$. Since within the transonic approximation

$$v' = (\gamma+1)\theta \text{ on the wedge}$$

and

$$u'_\infty \doteq M_\infty^2 - 1 \tag{101}$$

this implies that

$$(\gamma+1)\theta_{MAX} \doteq \frac{4}{3^{3/2}} (M_\infty^2 - 1)^{3/2} \tag{102}$$

or viewed in another light, this implies that the reduced attachment Mach number is

$$\xi_{\infty_A} = \frac{M_{\infty_A}^2 - 1}{\left[(\gamma+1)\theta\right]^{2/3}} = \frac{3}{4^{2/3}} = 1.19 \tag{103}$$

Similarly the wedge angle for obtaining exactly sonic velocity behind the shock is given by the value of v' where $u' = 0$. This is $v' = \frac{1}{\sqrt{2}} (u'_\infty)^{3/2}$. Again using Eq. (101) this can be written

$$(\gamma+1)\theta_S \doteq \frac{1}{\sqrt{2}} (M_\infty^2 - 1)^{3/2} \tag{104}$$

and viewed in another light this implies that the reduced Mach number for which sonic velocity is obtained behind the shock on a wedge is

$$\xi_{\infty_S} = \frac{M_{\infty_S}^2 - 1}{\left[(\gamma+1)\theta\right]^{2/3}} = 2^{1/3} = 1.26 \tag{105}$$

APPENDIX 4

VARIATION OF REDUCED MACH NUMBER AT WHICH SONIC VELOCITY OCCURS BEHIND AN OBLIQUE SHOCK WITH FLOW DEFLECTION ANGLE

The oblique shock relations can be written

$$M_2^2 = \frac{1 + \frac{\gamma-1}{2} M_1^2}{\gamma M_1^2 \sin^2\beta - \frac{\gamma-1}{2}} + \frac{M_1^2 \cos^2\beta}{1 + \frac{\gamma-1}{2} M_1^2 \sin\beta} \tag{106}$$

$$\tan\theta = 2 \operatorname{ctn}\beta \frac{M_1^2 \sin^2\beta - 1}{M_1^2 (\gamma + \cos 2\beta) + 2} \tag{107}$$

where

M_1 = Mach number ahead of shock

M_2 = Mach number behind shock

β = shock wave angle

θ = flow deflection

For $M_2 = 1$, eliminating β between these two equations yields

$$\tan\theta = \frac{f(M_1)}{\gamma M_1^2 - f(M_1)} \sqrt{\frac{M_1^2 - 1 + \frac{\gamma+1}{2\gamma} f(M_1)}{1 + \frac{\gamma+1}{2\gamma} f(M_1)}} \tag{108}$$

where

$$f(M_1) = \frac{M_1^2 - 1}{1} - 1 + \sqrt{1 + \frac{\gamma-1}{\gamma+1}(M_1^2 - 1) + \left(\frac{M_1^2 - 1}{2}\right)^2}$$

Expanding the right hand side in powers of $M_1^2 - 1$ (assumed small), one obtains

$$(\gamma+1)\tan\theta = \frac{(M_1^2 - 1)^{3/2}}{2^{1/2}} \left[1 - \frac{19\gamma + 2}{16(\gamma+1)} (M_1^2 - 1) + \cdots\right] \tag{109}$$

Reverting this series and letting $\theta \doteq \tan\theta$, and $M_1 = M_{\infty_S}$, one finds

$$\xi_{\infty_S} = \frac{M_{\infty_S}^2 - 1}{\left[(\gamma+1)\,\theta\right]^{2/3}} = 2^{1/3}\left[1 + \frac{19\gamma+2}{24\left(\frac{\gamma+1}{2}\right)^{1/3}}\,\theta^{2/3} + O\left(\theta^{4/3}\right)\right] \qquad (110)$$

for $\gamma = 1.4$,

$$\frac{19\gamma+2}{24\left(\frac{\gamma+1}{2}\right)^{1/3}} = 1.122$$

APPENDIX 5

VARIATION OF REDUCED MACH NUMBER BEHIND A PRANDTL-MEYER EXPANSION FROM M = 1 THROUGH AN ANGLE θ, WITH θ

The exact relation here is

$$\theta = \sqrt{\frac{\gamma+1}{\gamma-1}}\ \tan^{-1}\sqrt{\frac{\gamma-1}{\gamma+1}}\ \sqrt{M_{pM}^2-1}\ -\ \tan^{-1}\sqrt{M_{pM}^2-1} \tag{111}$$

Expanding the right hand side in terms of $\sqrt{M_{pM}^2-1}$, using

$$\tan^{-1} x = x - \frac{x^3}{3} + \frac{x^5}{5} - \frac{x^7}{7} + \cdots$$

one obtains

$$(\gamma+1)\theta = \frac{2}{3}\left(M_{pM}^2-1\right)^{3/2} \sum_{n=1}^{\infty} \frac{(-)^n a_n \left(M_{pM}^2-1\right)^n}{1+\frac{2n}{3}} \tag{112}$$

where

$$a_n = \frac{\gamma+1}{2}\left[1-\left(\frac{\gamma-1}{\gamma+1}\right)^{n+1}\right]$$

Reverting this series the first few terms are

$$M_{pM}^2-1 = \left[\frac{3(\gamma+1)}{2}\theta\right]^{3/2}\left\{1+\frac{4\gamma}{5(\gamma+1)}\left[\frac{3(\gamma+1)}{2}\theta\right]^{2/3}+O\left(\theta^{4/3}\right)\right\} \tag{113}$$

Therefore,

$$\Xi_{pM} = \frac{M_{pM}^2-1}{\left[(\gamma+1)\theta\right]^{2/3}} = \left(\frac{3}{2}\right)^{2/3}\left[1+\frac{4\gamma}{5(\gamma+1)}\left[\frac{3(\gamma+1)}{2}\right]^{2/3}\theta^{2/3}+O\left(\theta^{4/3}\right)\right] \tag{114}$$

For $\gamma = 1.4$

$$\frac{4\gamma}{5(\gamma+1)}\left[\frac{3(\gamma+1)}{2}\right]^{2/3} = 1.097$$

GEOMETRY OF SECTIONS TESTED

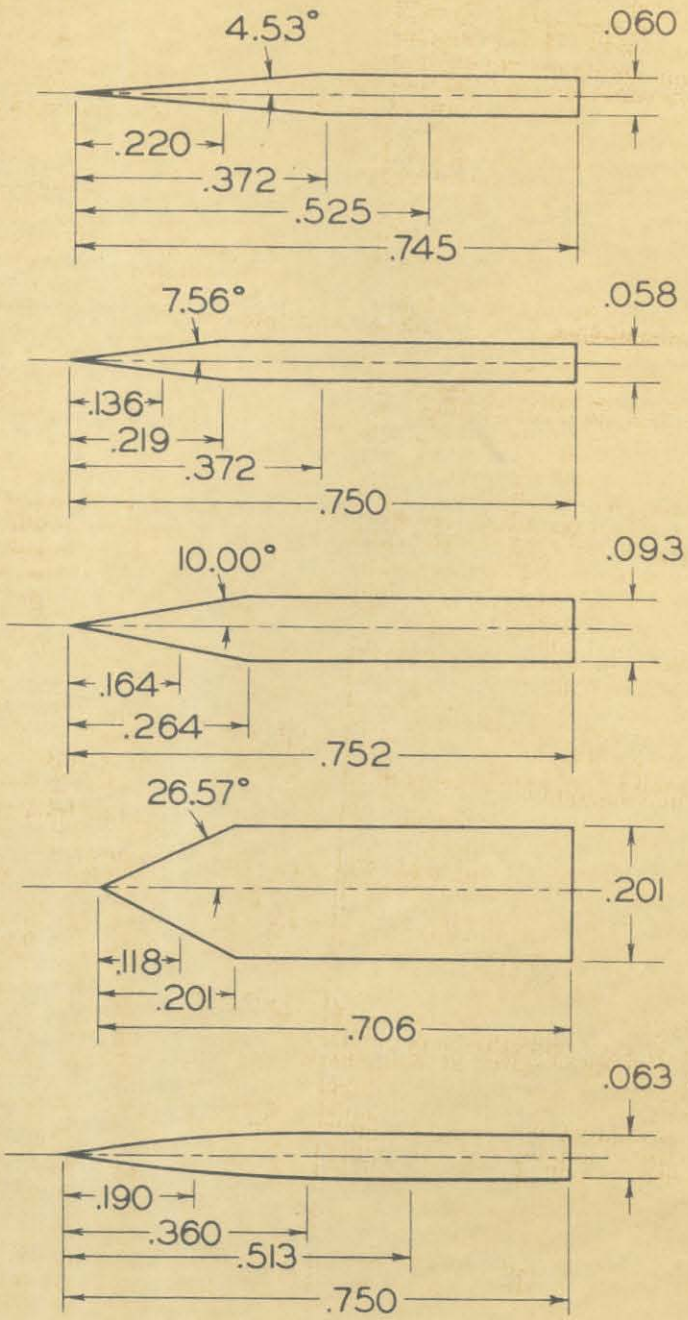

ALL DIMENSIONS IN INCHES

FIG. 1

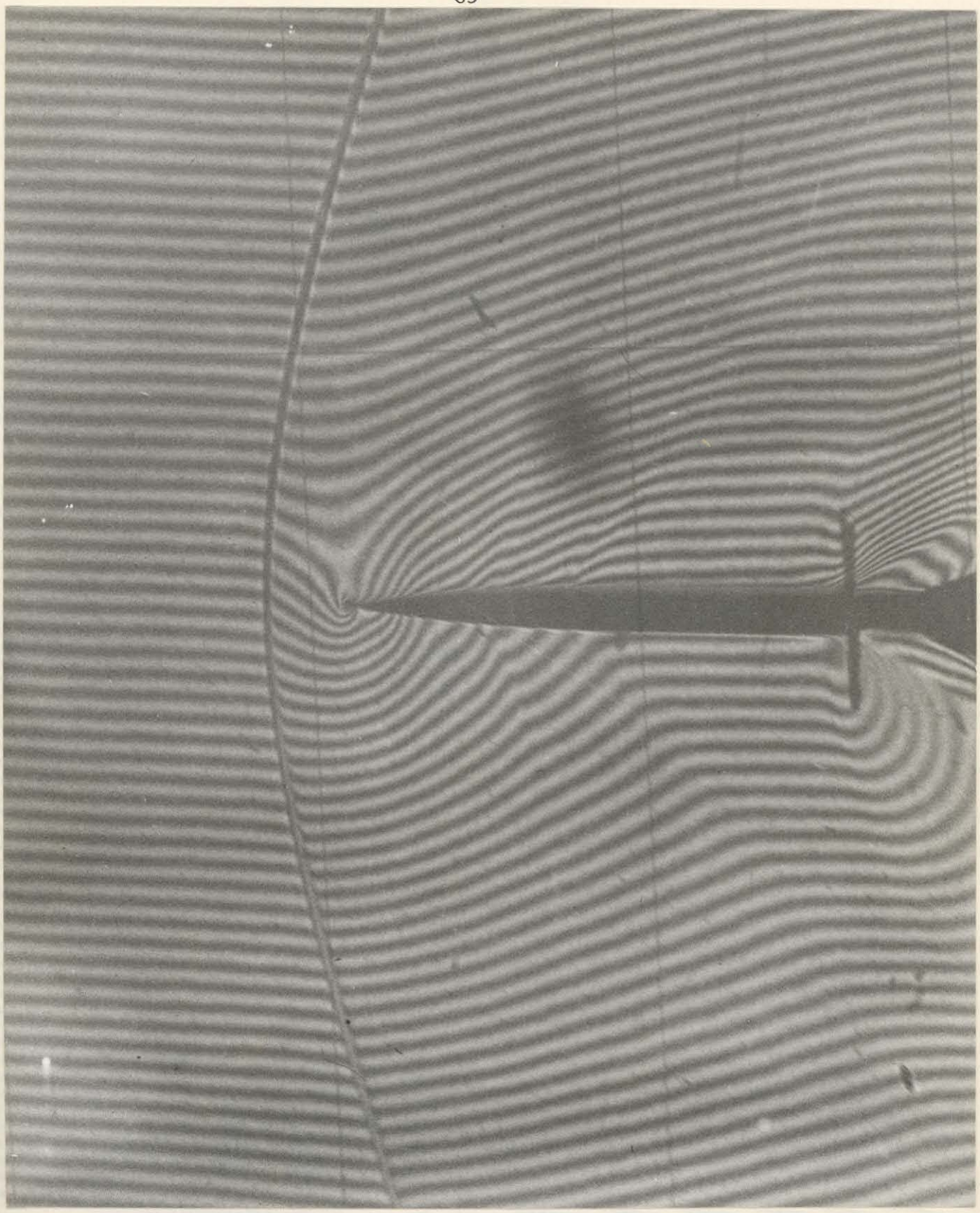

Typical Finite Fringe Interferogram

8.8% Circular Arc Section at M = 1.200

Fig. 2

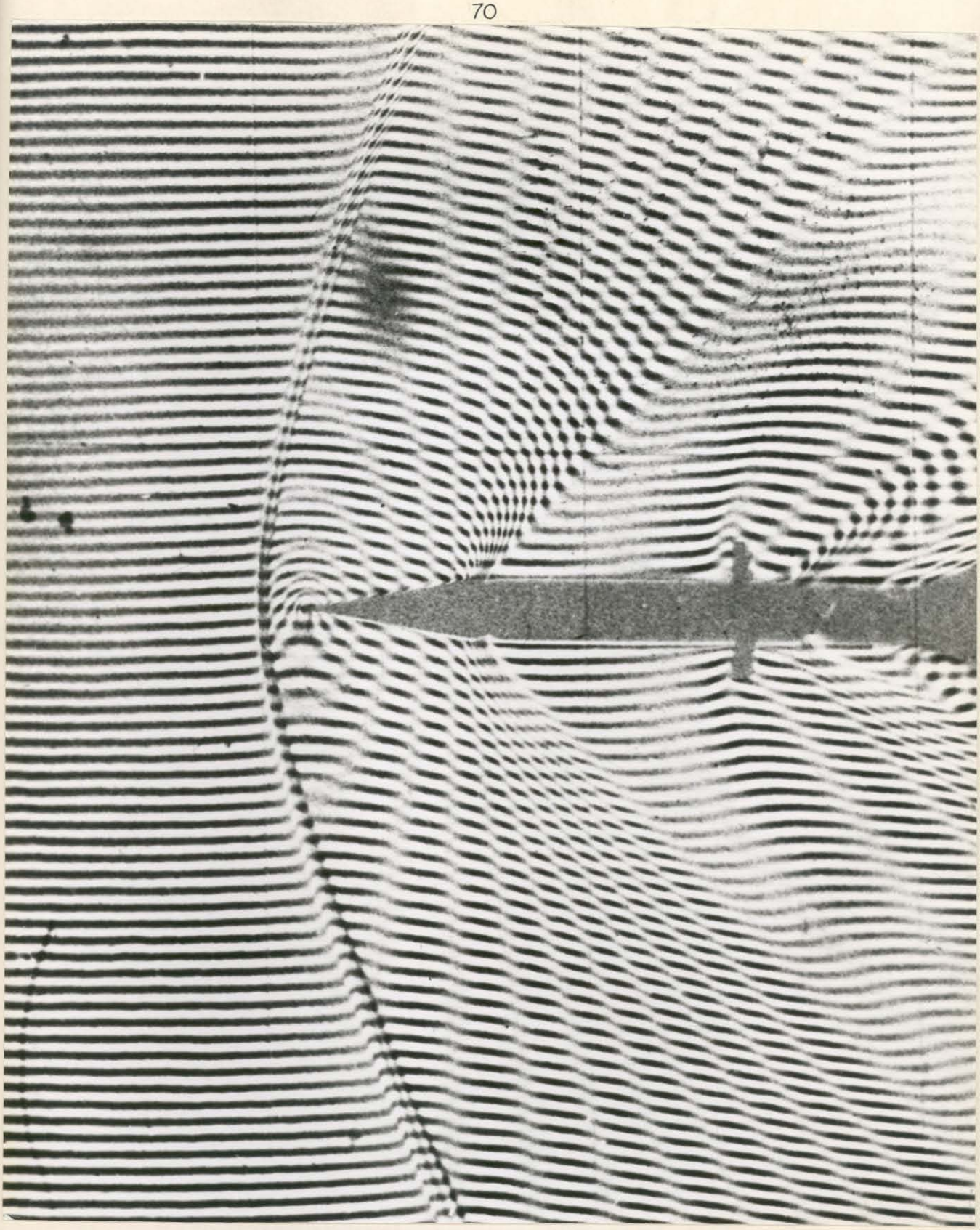

Typical Superimposed Finite Fringe Interferogram

10 Semi-Angle Wedge at M = 1.278

Fig. 3

INCREMENT IN MACH NUMBER PER FRINGE CONTOUR VERSUS LOCAL MACH NUMBER FOR AIR ($\gamma = 1.4$)

$\frac{\lambda}{K\ell\rho_0} = .0\,25 \pm 0.001$ FOR THESE TESTS

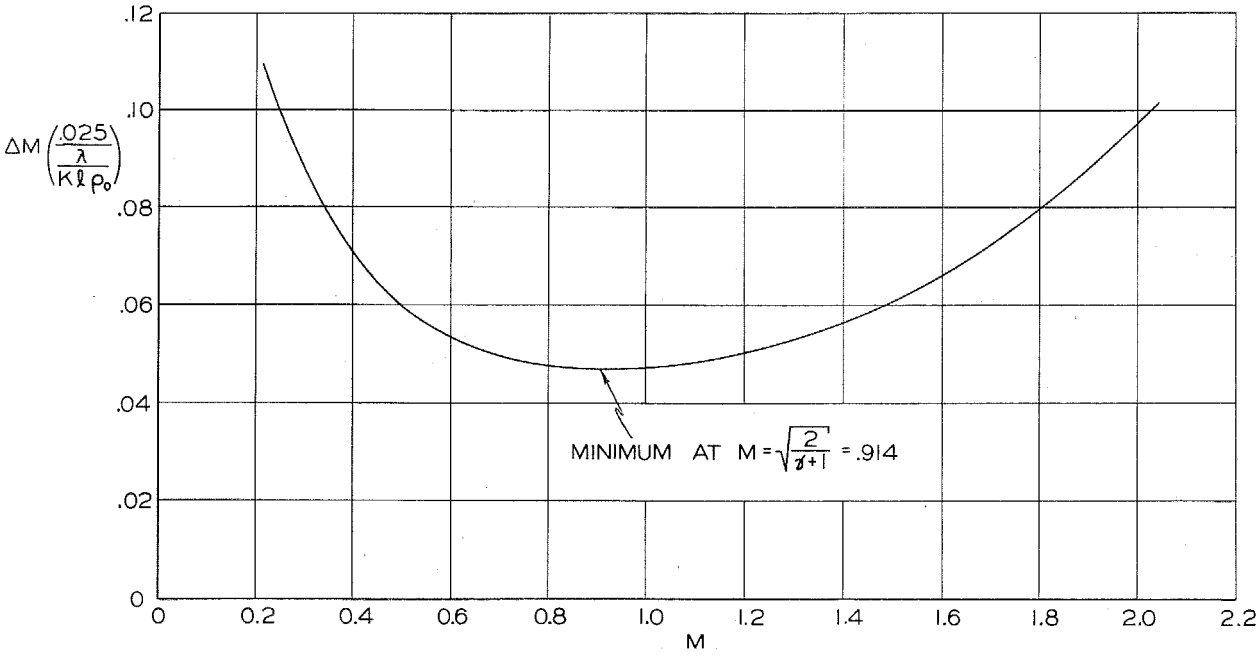

FIG. 4

THEORETICAL REDUCED LOCAL MACH NUMBER DISTRIBUTIONS ON A WEDGE NEAR MACH NUMBER ONE

COLE, GUDERLEY, VINCENTI, AND TSIEN AND BARON

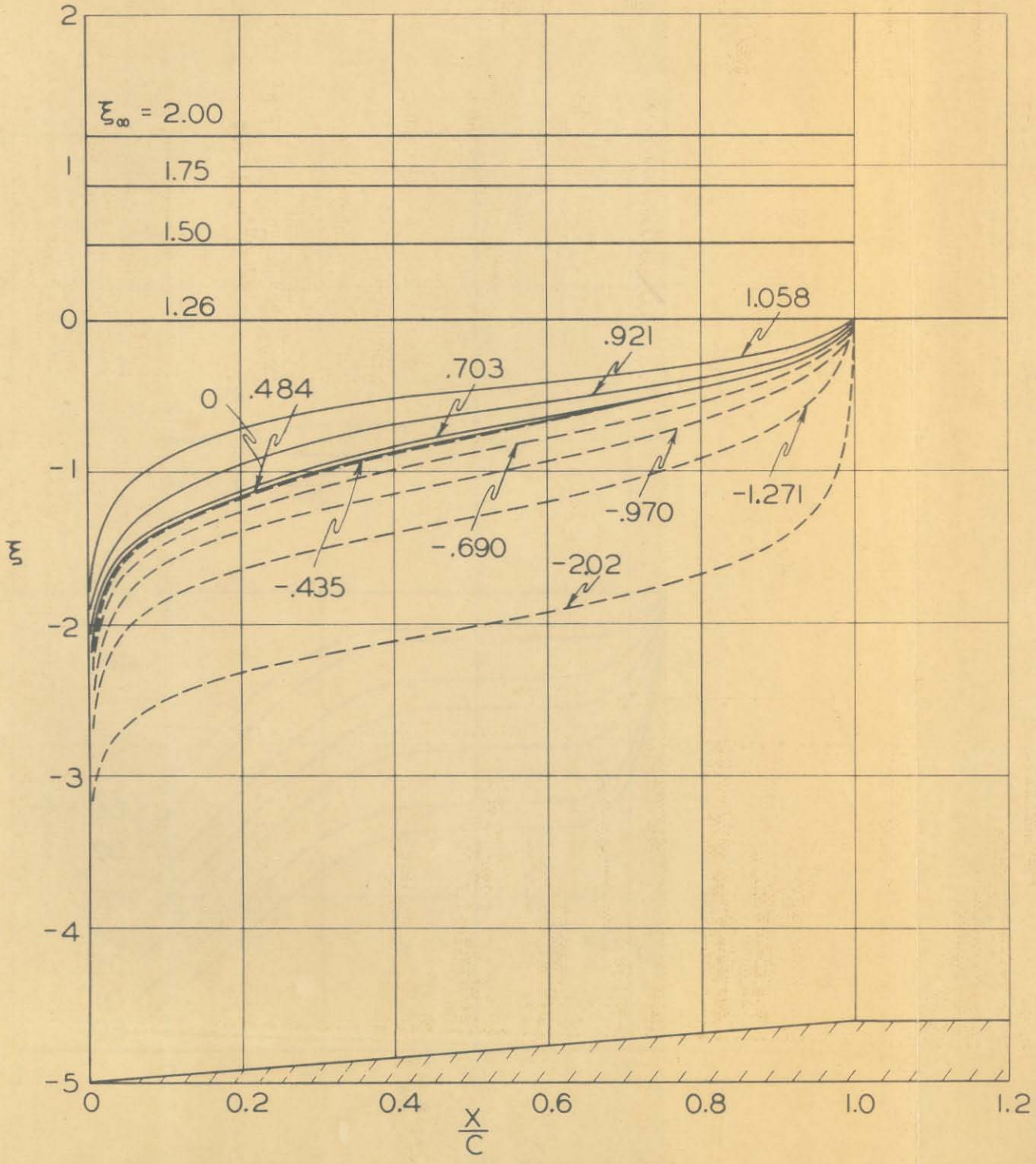

FIG. 5

THEORETICAL REDUCED LOCAL MACH NUMBER VERSUS REDUCED FREE STREAM MACH NUMBER AT SEVERAL CHORDWISE STATIONS ON A WEDGE

COLE, GUDERLEY, VINCENTI, AND TSIEN AND BARON

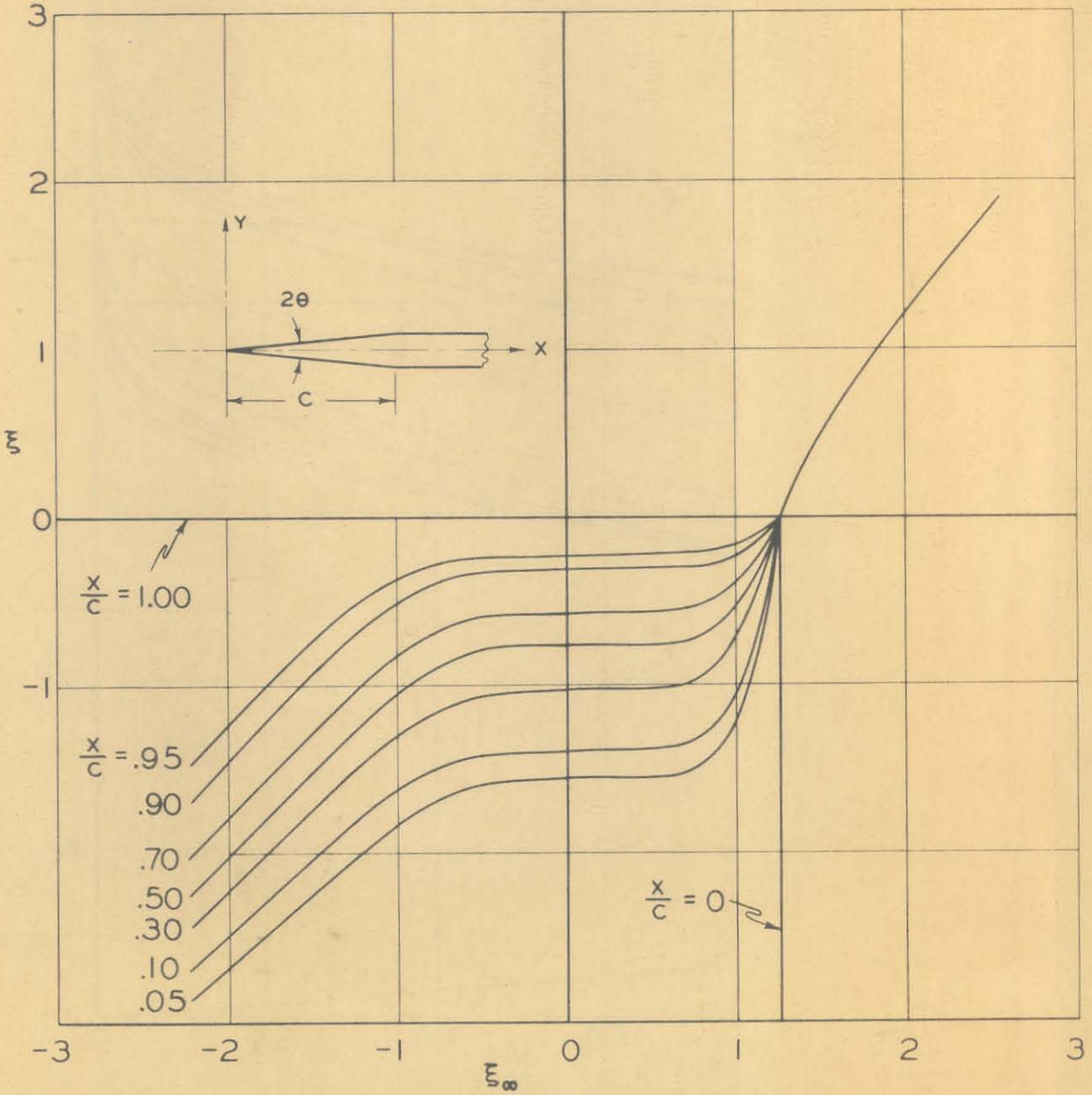

FIG. 6

THEORETICAL REDUCED PRESSURE COEFFICIENT DISTRIBUTIONS ON A WEDGE NEAR MACH NUMBER ONE

COLE, GUDERLEY, VINCENTI, AND TSIEN AND BARON

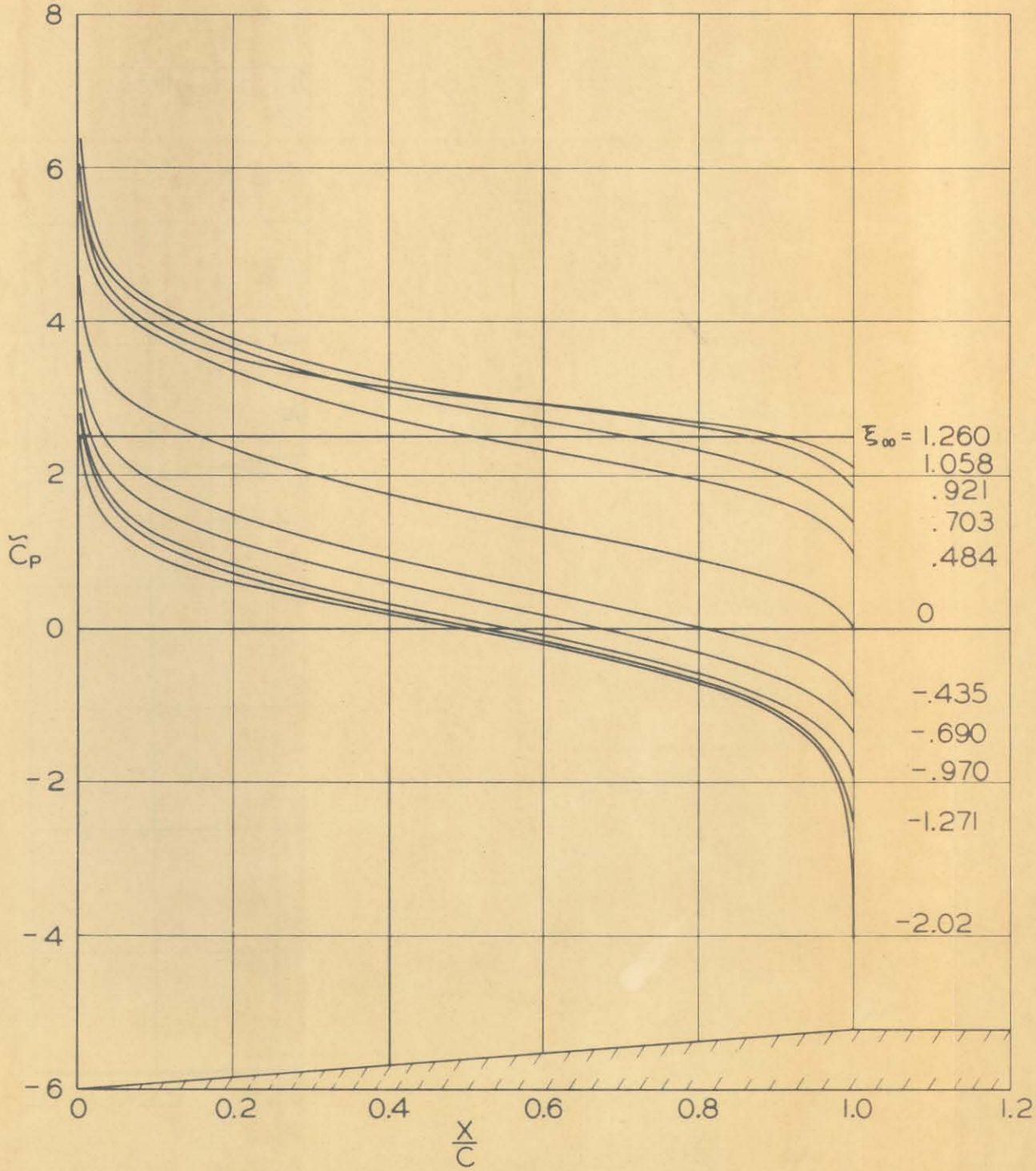

FIG. 7

THEORETICAL REDUCED DRAG COEFFICIENT VERSUS REDUCED MACH NUMBER FOR A WEDGE

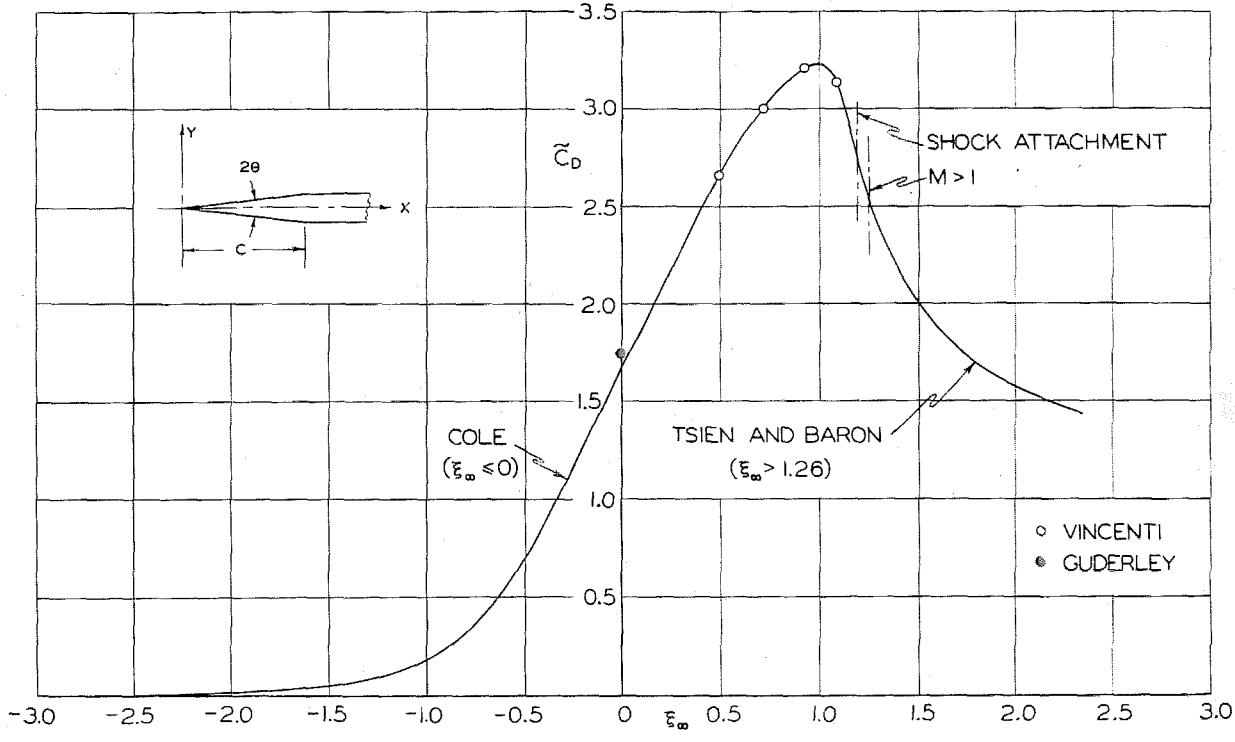

FIG. 8

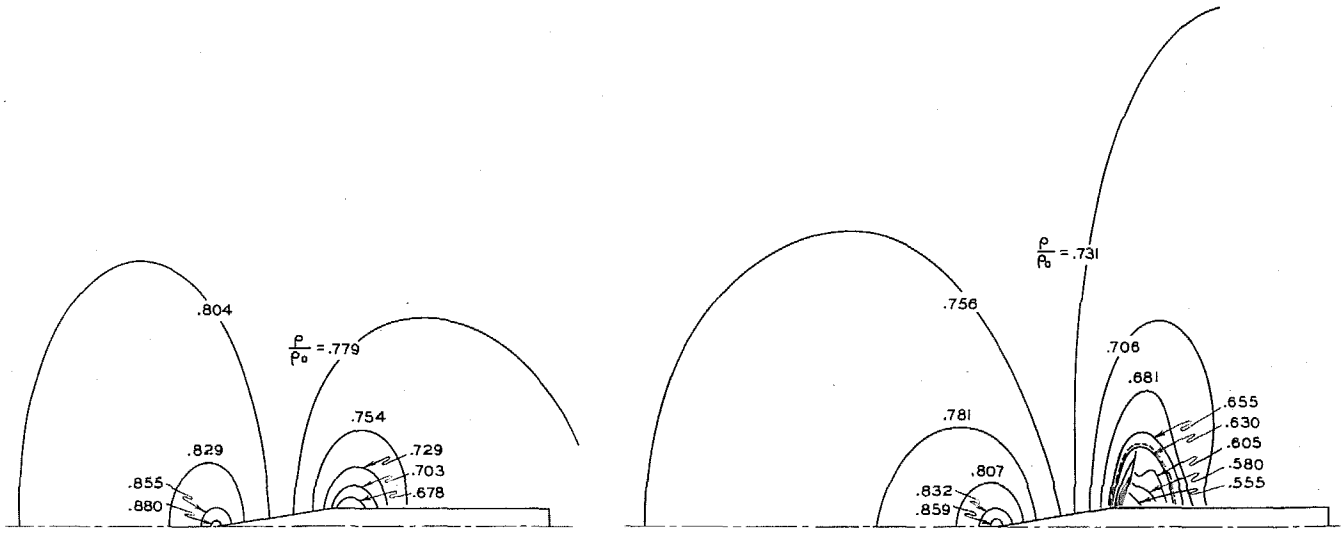

M_∞ = .700

$\frac{\rho_\infty}{\rho_0}$ = .791

M_∞ = .794

$\frac{\rho_\infty}{\rho_0}$ = .743

10° SEMI-ANGLE WEDGE

FIG. 9

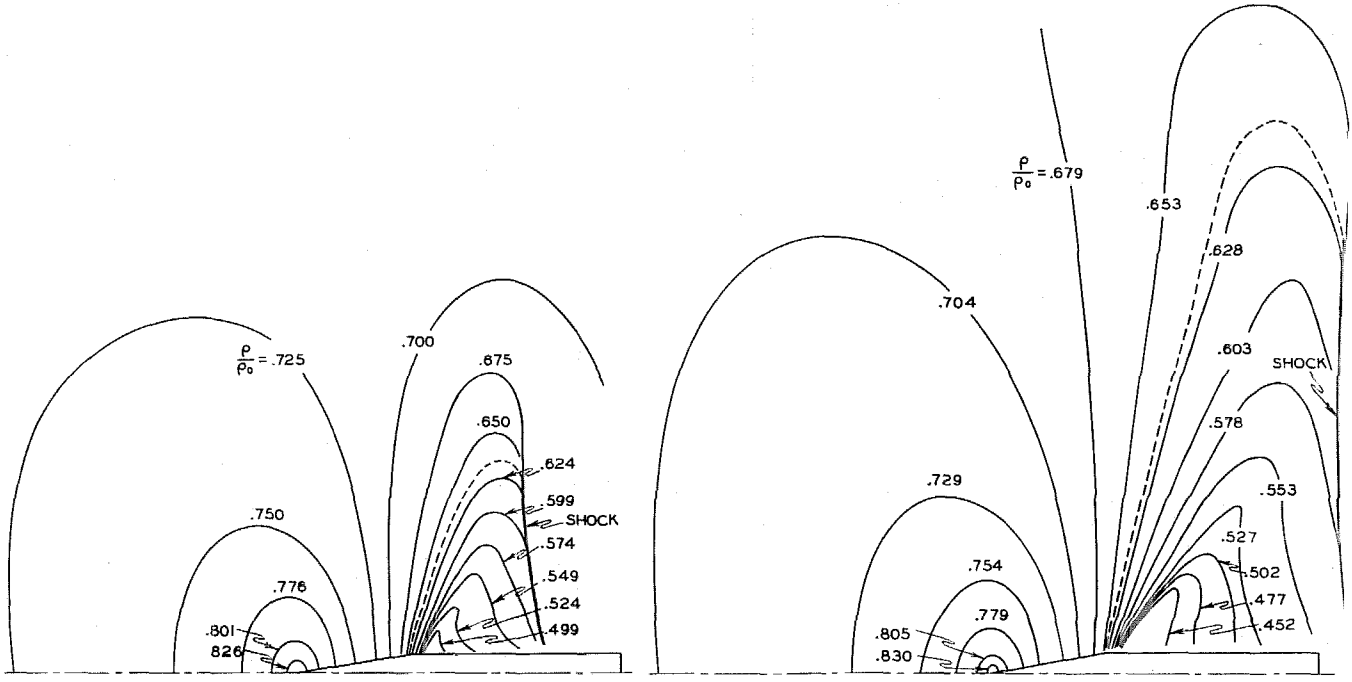

$M_\infty = .852$

$\frac{\rho_\infty}{\rho_0} = .712$

$M_\infty = .892$

$\frac{\rho_\infty}{\rho_0} = .691$

10° SEMI-ANGLE WEDGE

FIG. 10

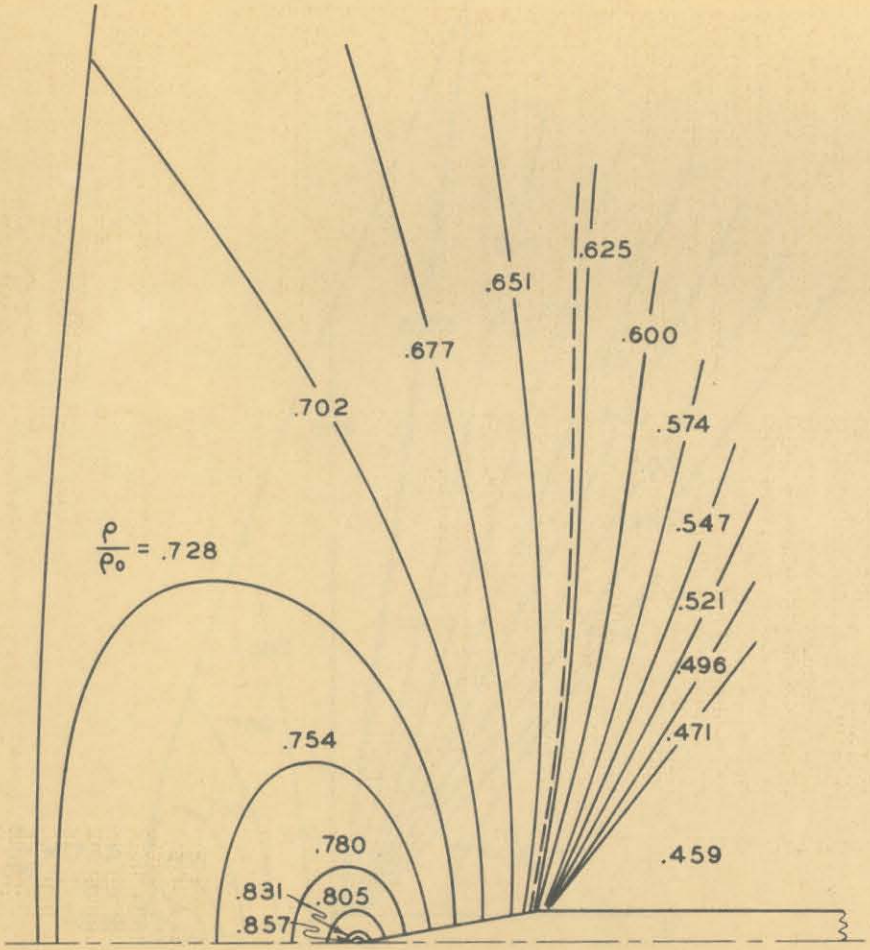

$M_\infty = 1.207$

$\frac{\rho_\infty}{\rho_0} = .528$

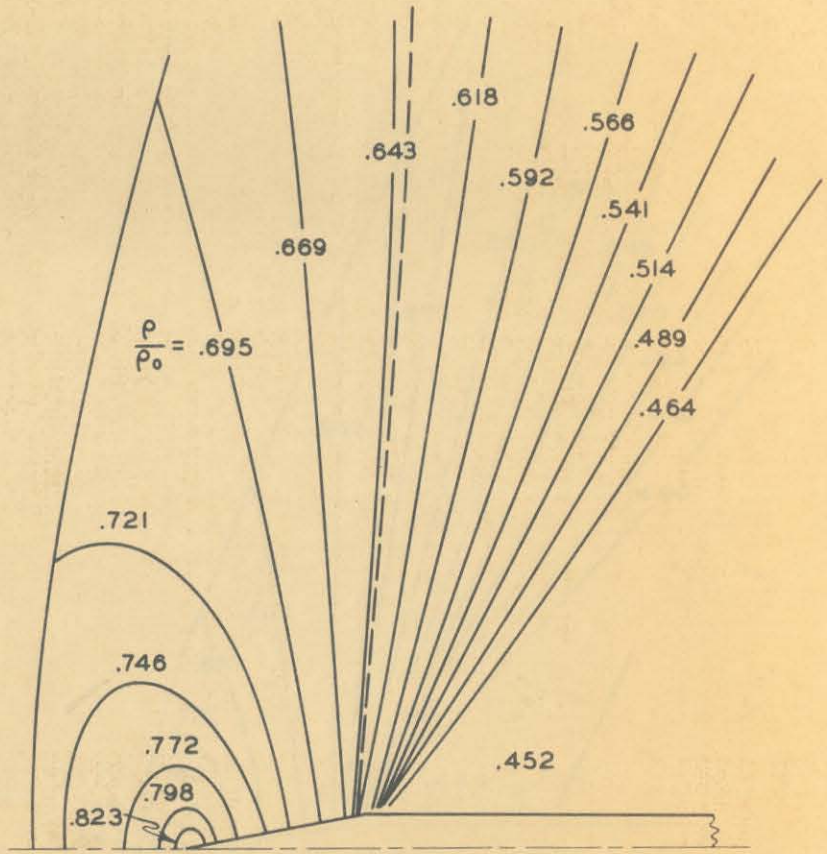

$M_\infty = 1.240$

$\frac{\rho_\infty}{\rho_0} = .511$

10° SEMI-ANGLE WEDGE

FIG. 11

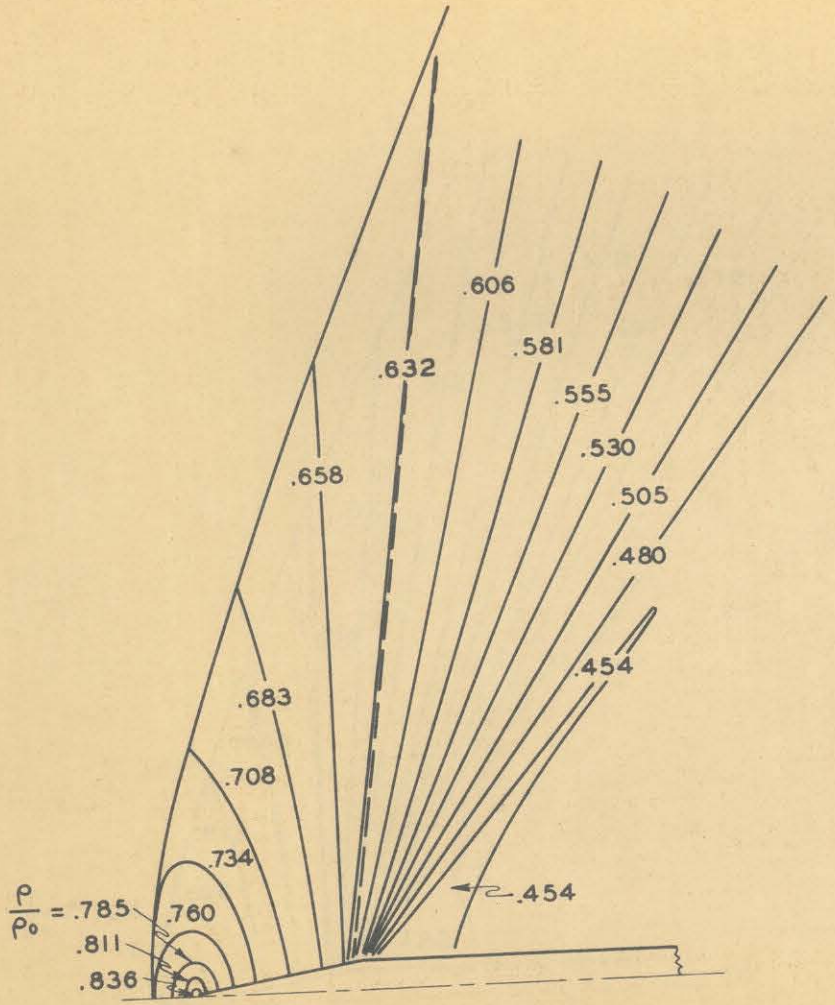

$M_\infty = 1.278$

$\frac{\rho_\infty}{\rho_0} = .493$

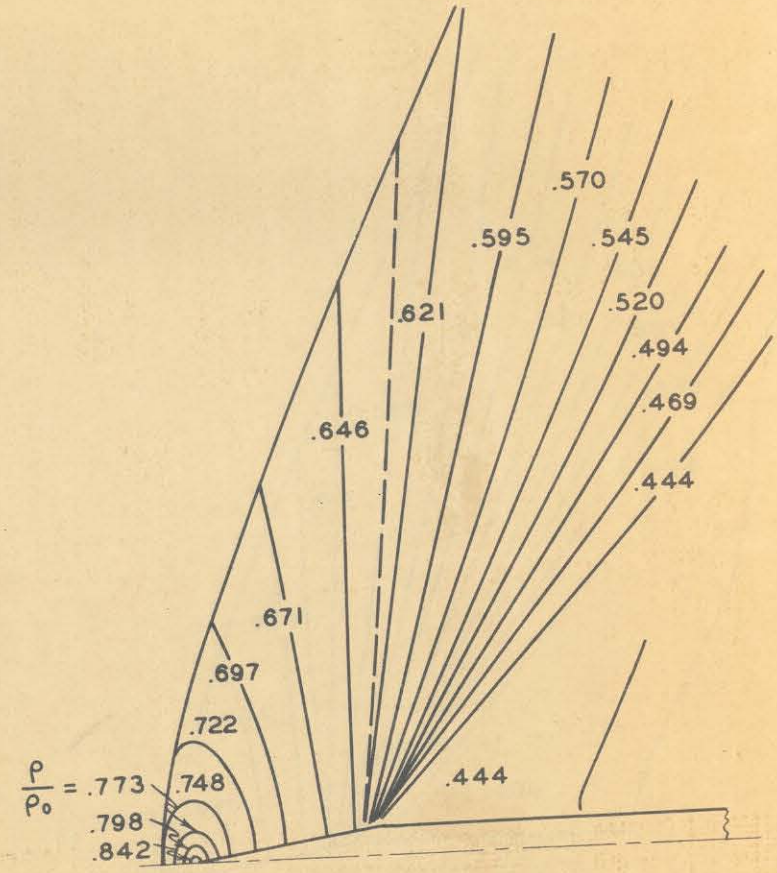

$M_\infty = 1.315$

$\frac{\rho_\infty}{\rho_0} = .476$

10° SEMI-ANGLE WEDGE

FIG. 12

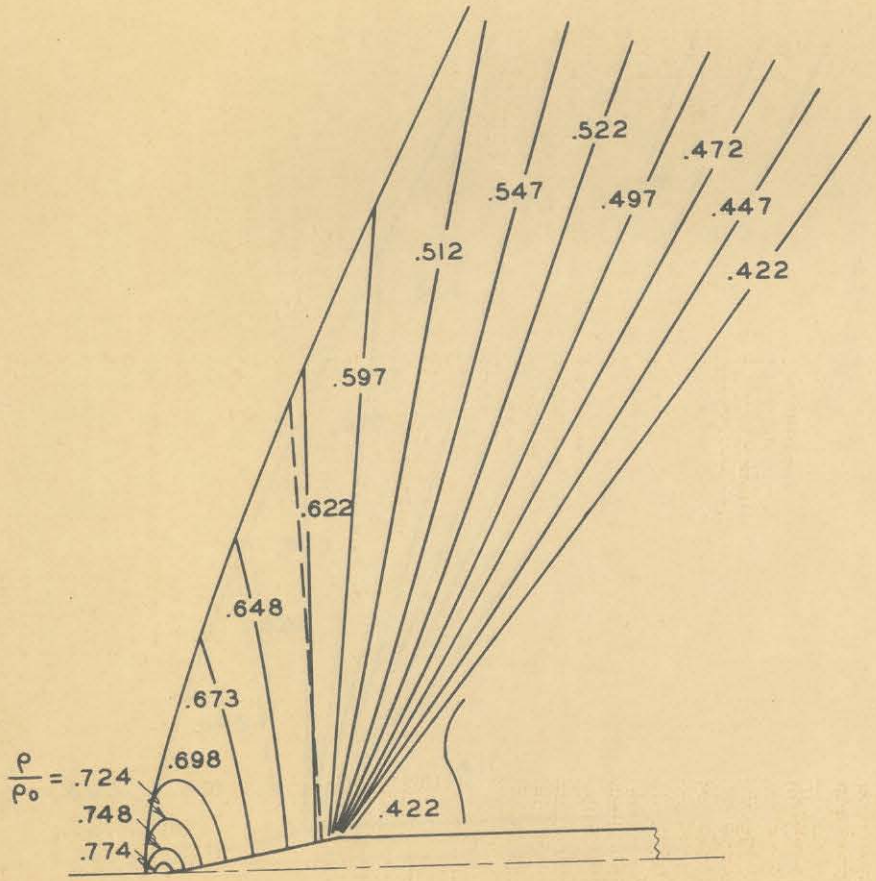

$M_\infty = 1.356$

$\frac{\rho_\infty}{\rho_0} = .457$

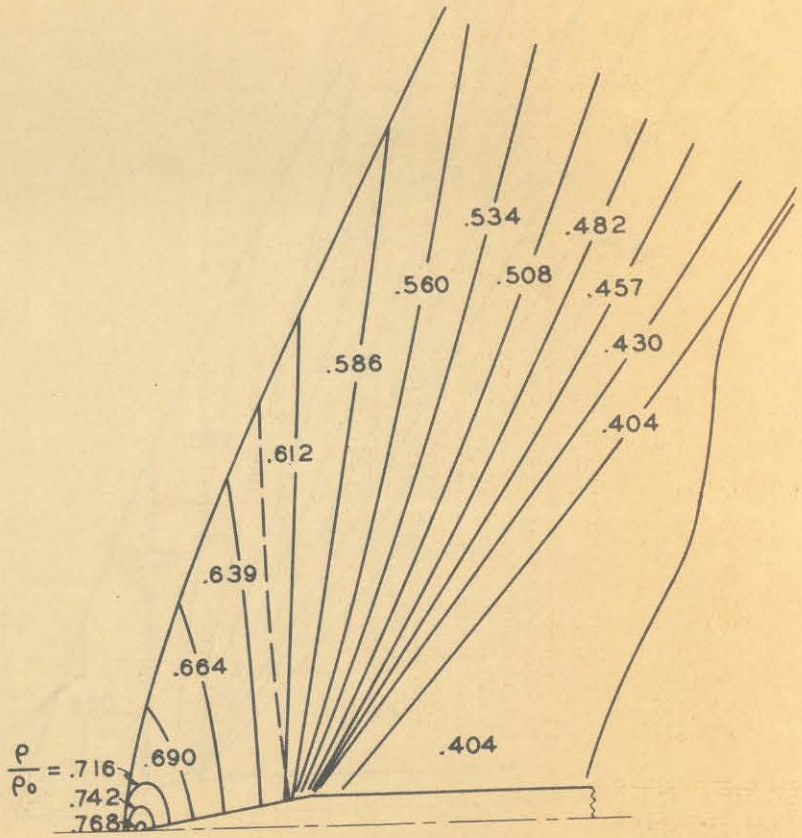

$M_\infty = 1.375$

$\frac{\rho_\infty}{\rho_0} = .449$

10° SEMI-ANGLE WEDGE

FIG. 13

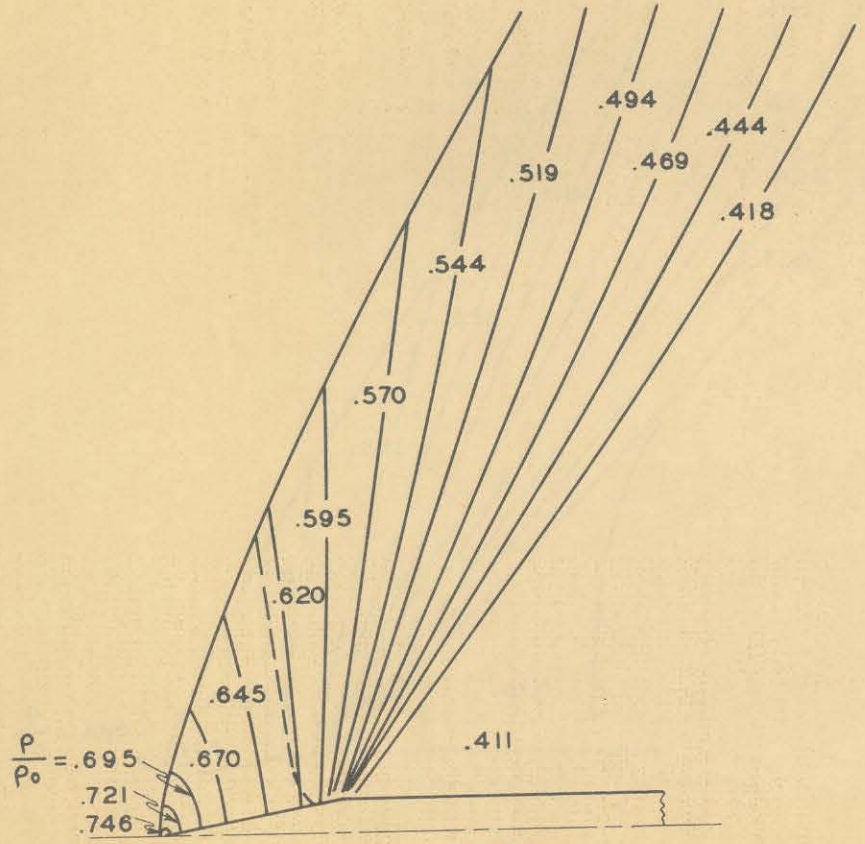

$M_\infty = 1.391$

$\frac{\rho_\infty}{\rho_0} = .441$

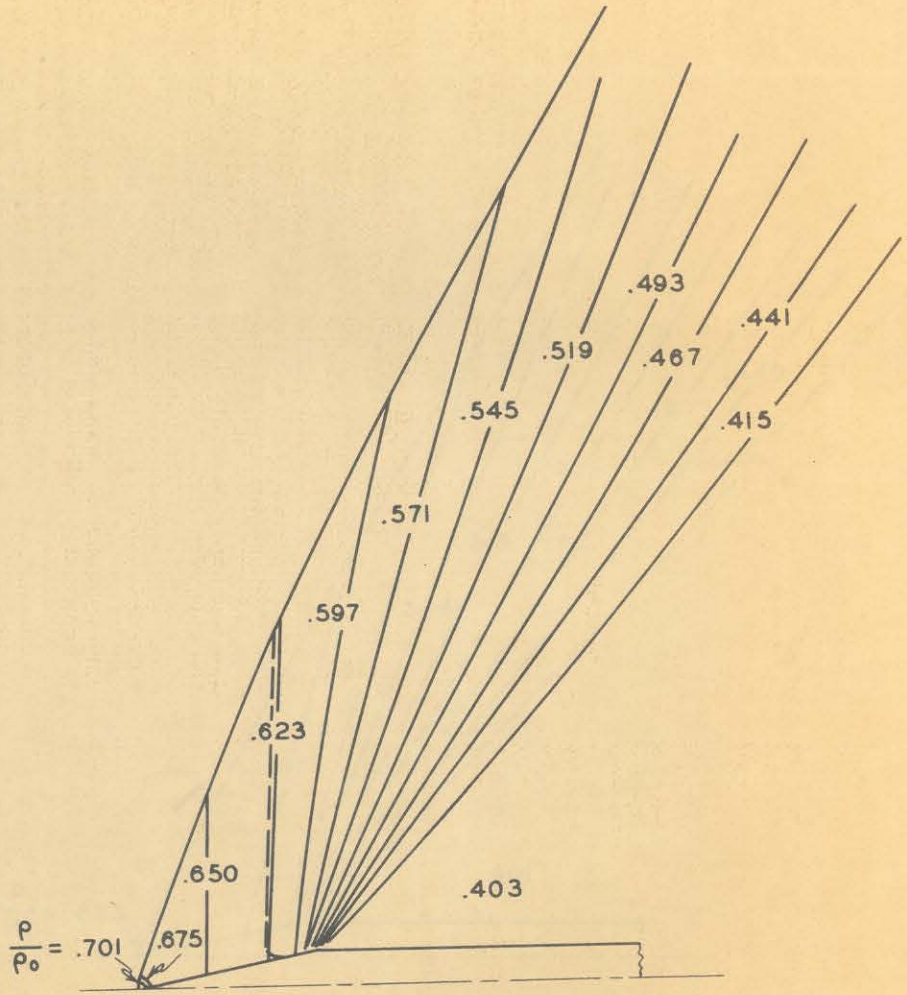

$M_\infty = 1.411$

$\frac{\rho_\infty}{\rho_0} = .432$

10° SEMI-ANGLE WEDGE

FIG. 14

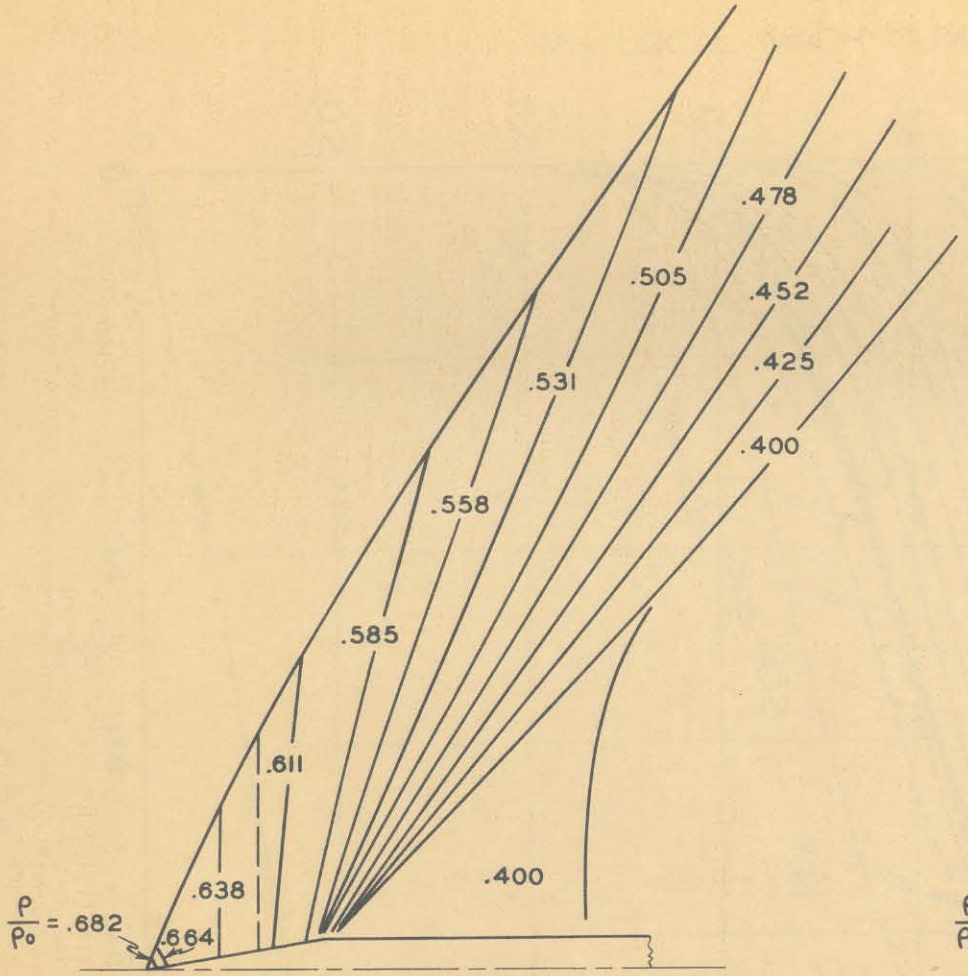

M_∞ = 1.436

$\frac{\rho_\infty}{\rho_0}$ = .422

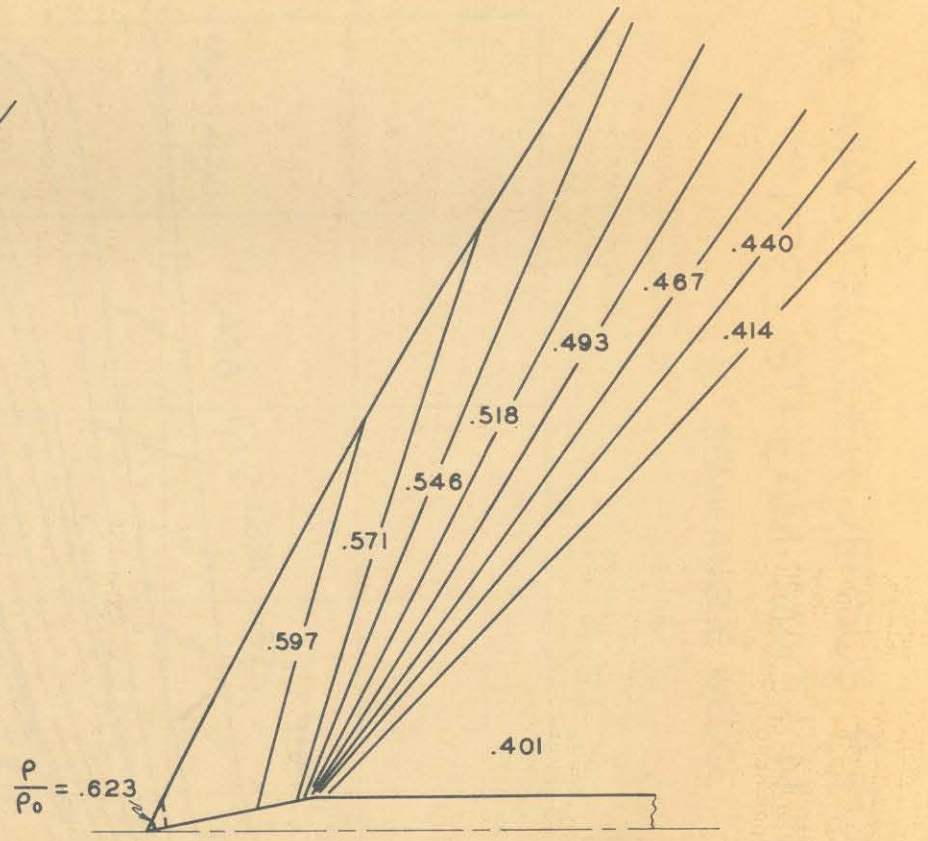

M_∞ = 1.465

$\frac{\rho_\infty}{\rho_0}$ = .409

10° SEMI-ANGLE WEDGE

FIG. 15

LOCAL MACH NUMBER VERSUS $\frac{X}{C}$ FOR INCREASING FREE STREAM MACH NUMBER

10° SEMI-ANGLE WEDGE

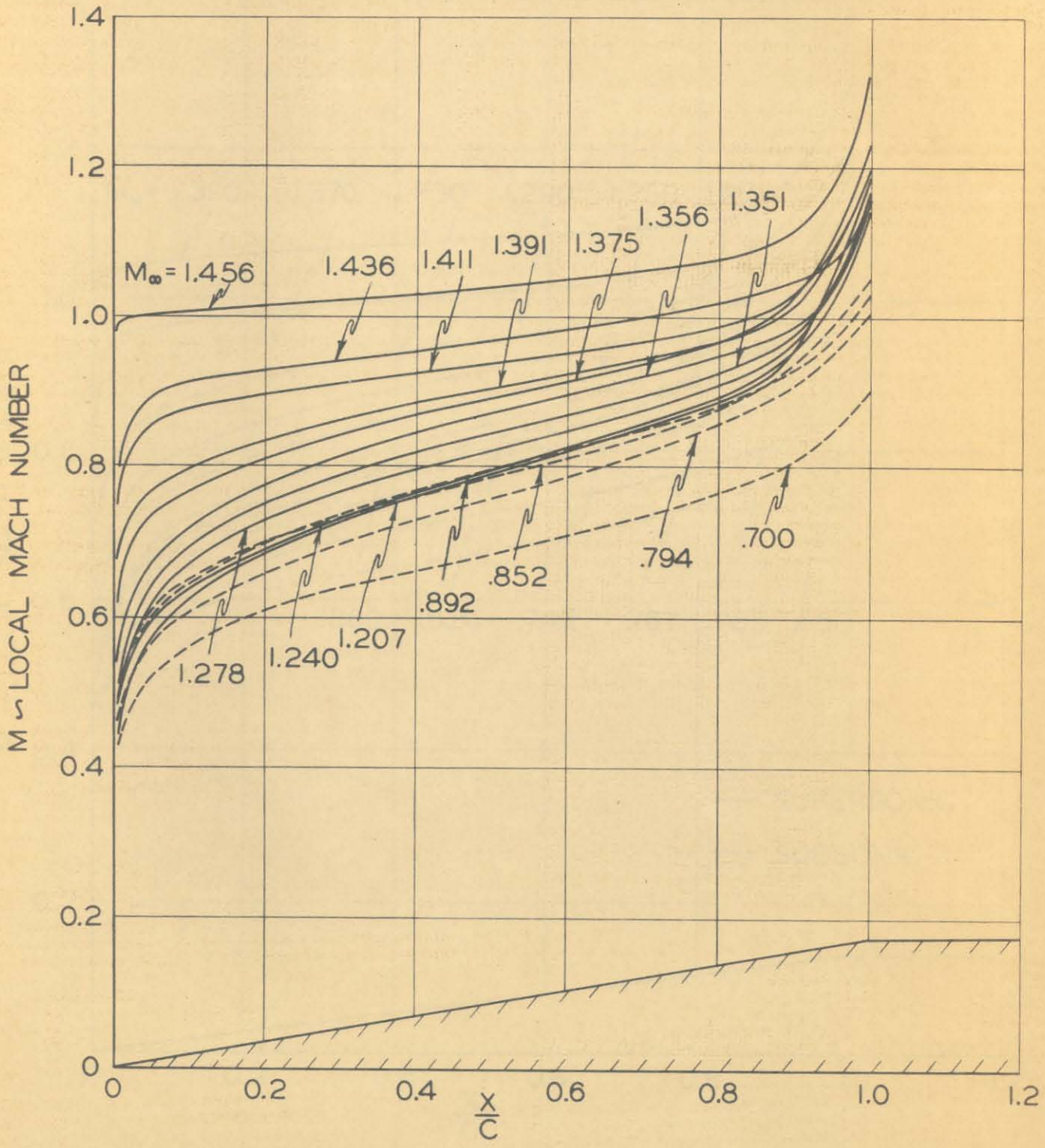

FIG. 16

LOCAL MACH NUMBER VERSUS $\frac{X}{C}$ FOR INCREASING FREE STREAM MACH NUMBER

$7\frac{1}{2}^{\circ}$ SEMI-ANGLE WEDGE

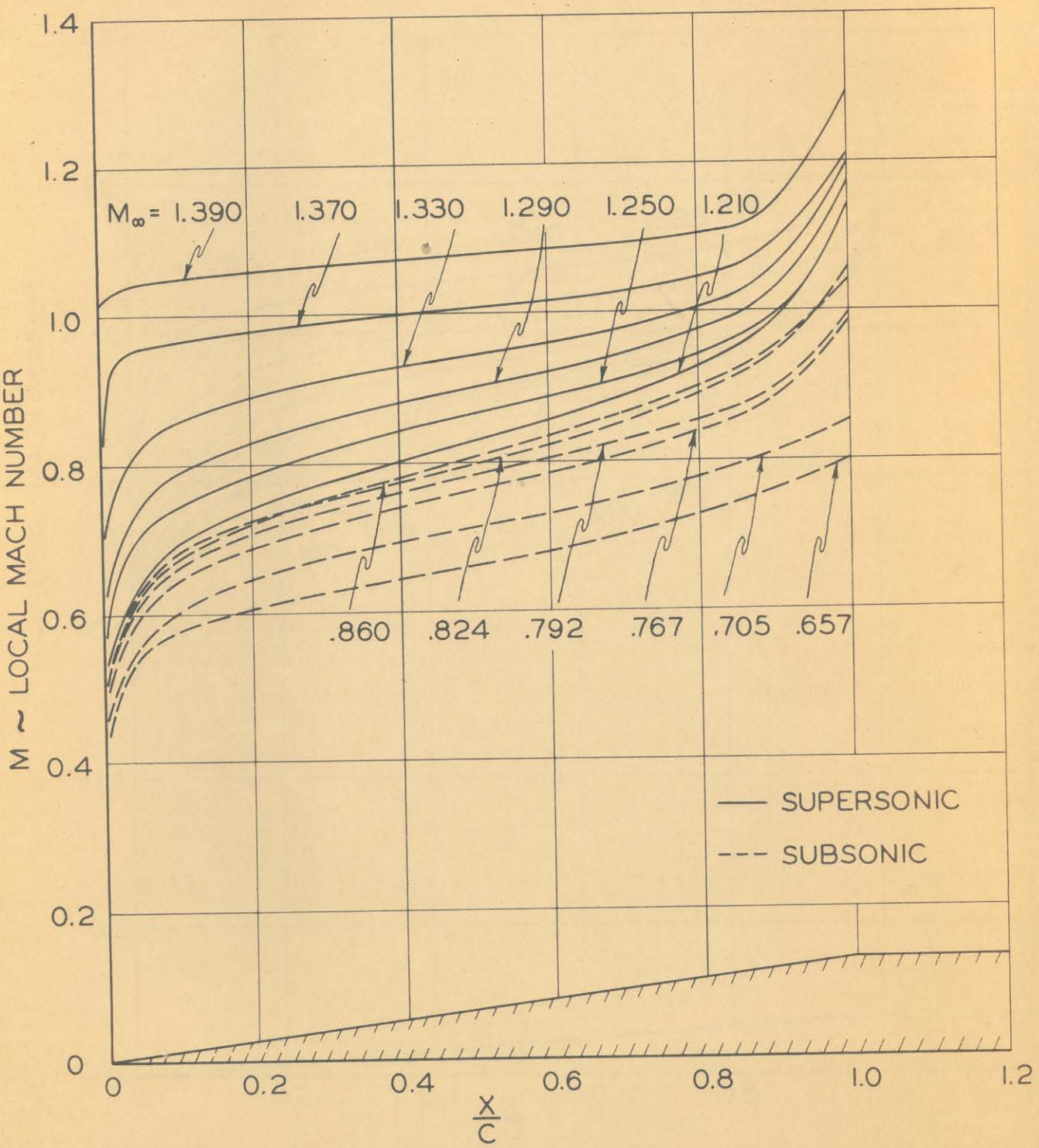

FIG. 17

LOCAL MACH NUMBER VERSUS $\frac{X}{C}$ FOR INCREASING FREE STREAM MACH NUMBER

$4\frac{1}{2}^{\circ}$ SEMI-ANGLE WEDGE

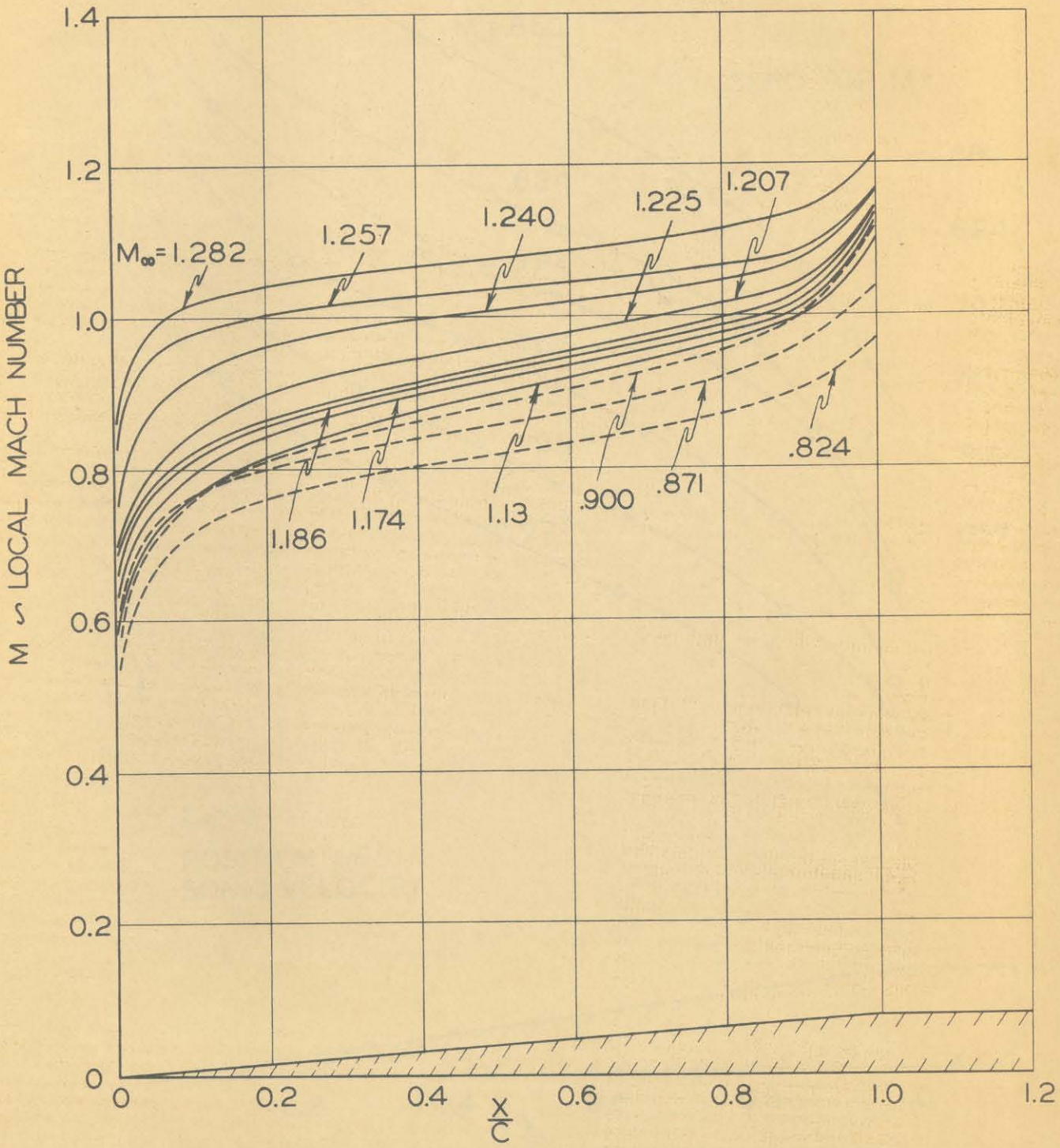

FIG. 18

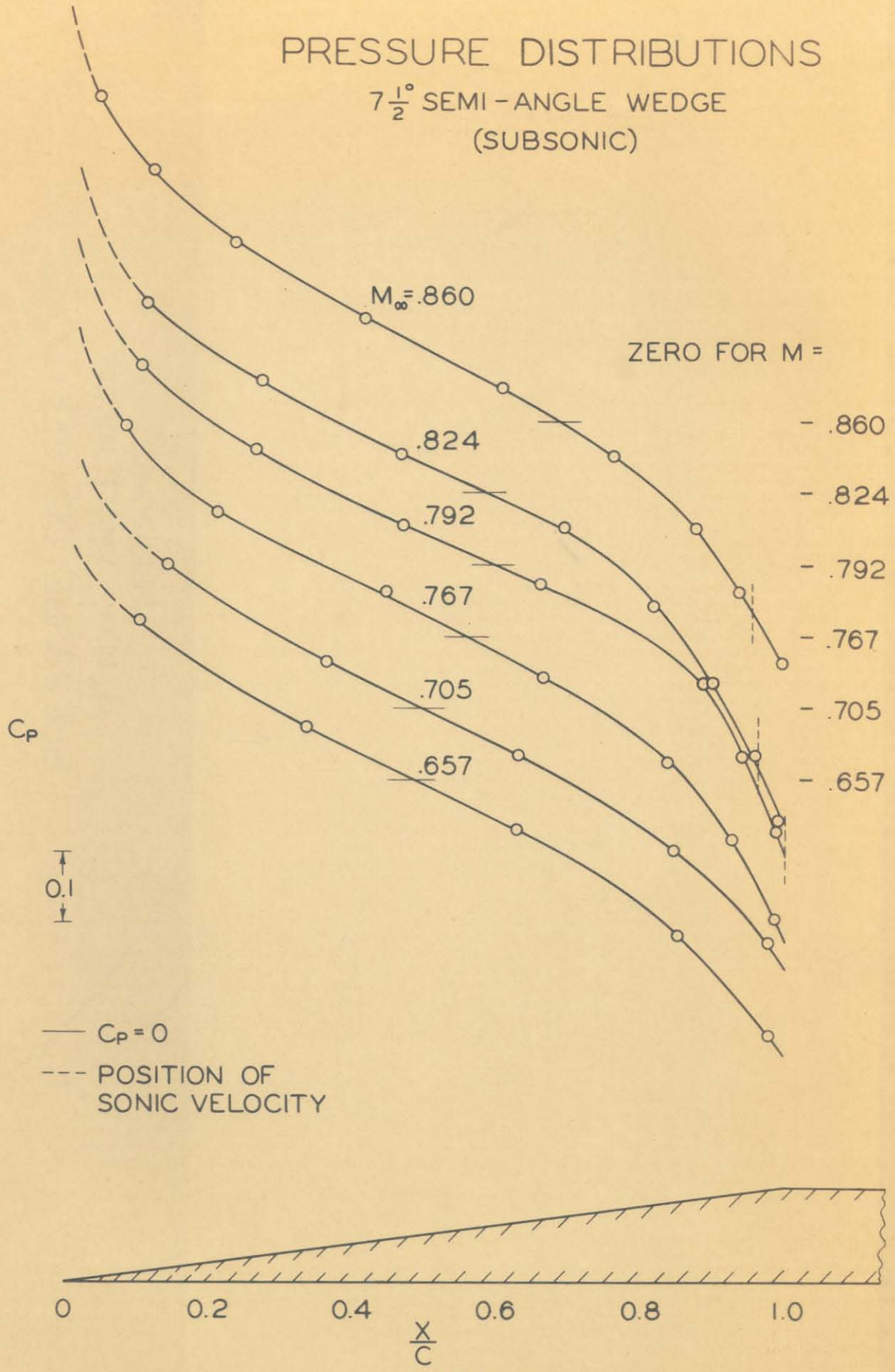
PRESSURE DISTRIBUTIONS
7 1/2° SEMI-ANGLE WEDGE
(SUBSONIC)
M∞=.860
.824
.792
.767
.705
.657
ZERO FOR M =
- .860
- .824
- .792
- .767
- .705
- .657
Cp
0.1
Cp = 0
POSITION OF SONIC VELOCITY
0
0.2
0.4
0.6
0.8
1.0
X/C

FIG. 19

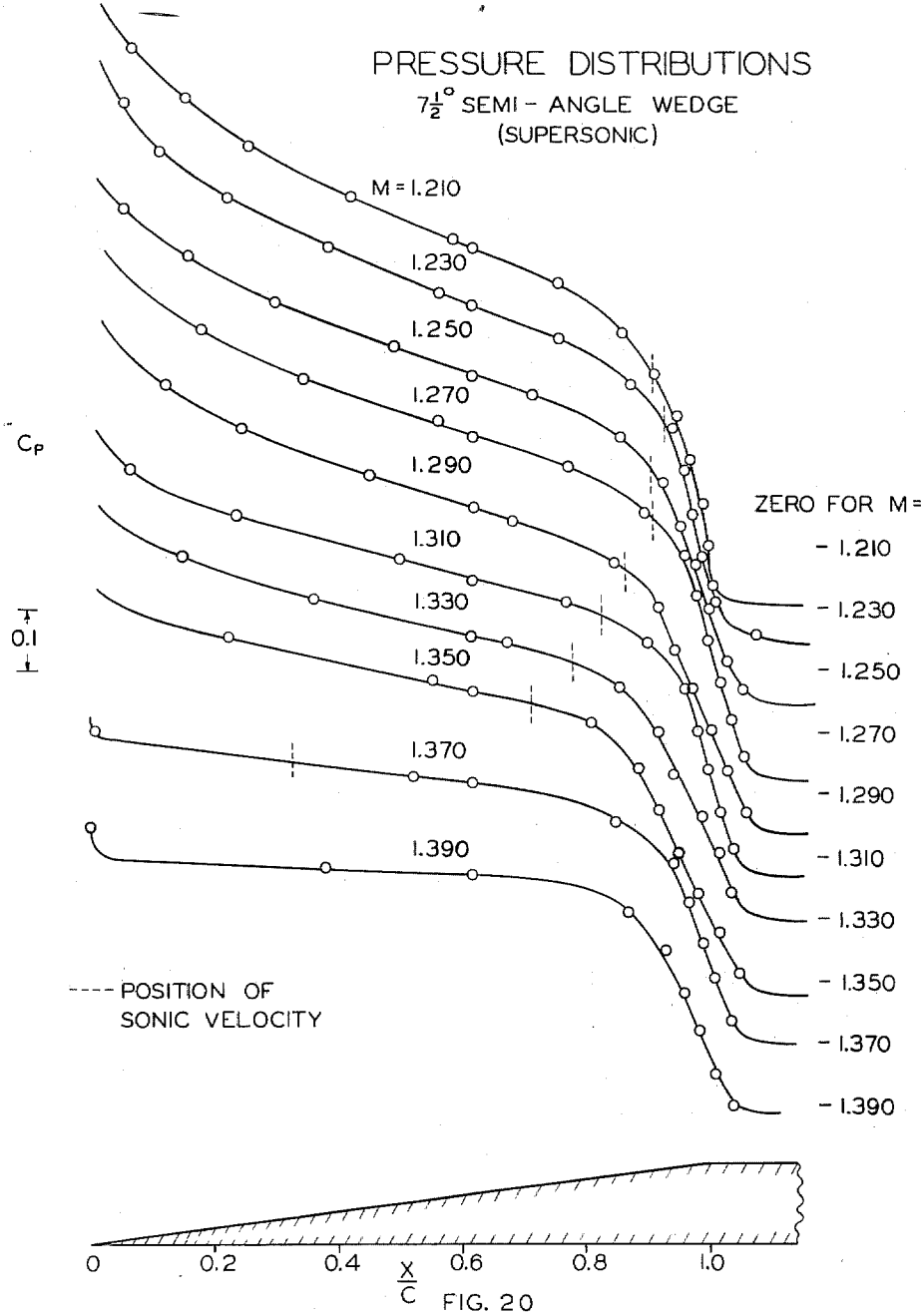
PRESSURE DISTRIBUTIONS
7½° SEMI - ANGLE WEDGE
(SUPERSONIC)
M = 1.210
1.230
1.250
1.270
1.290
1.310
1.330
1.350
1.370
1.390
C_P
0.1
ZERO FOR M =
- 1.210
- 1.230
- 1.250
- 1.270
- 1.290
- 1.310
- 1.330
- 1.350
- 1.370
- 1.390
---- POSITION OF SONIC VELOCITY
0
0.2
0.4
0.6
0.8
1.0
X/C

FIG. 20

SHOCK DETACHMENT DISTANCE VERSUS REDUCED MACH NUMBER FOR A WEDGE

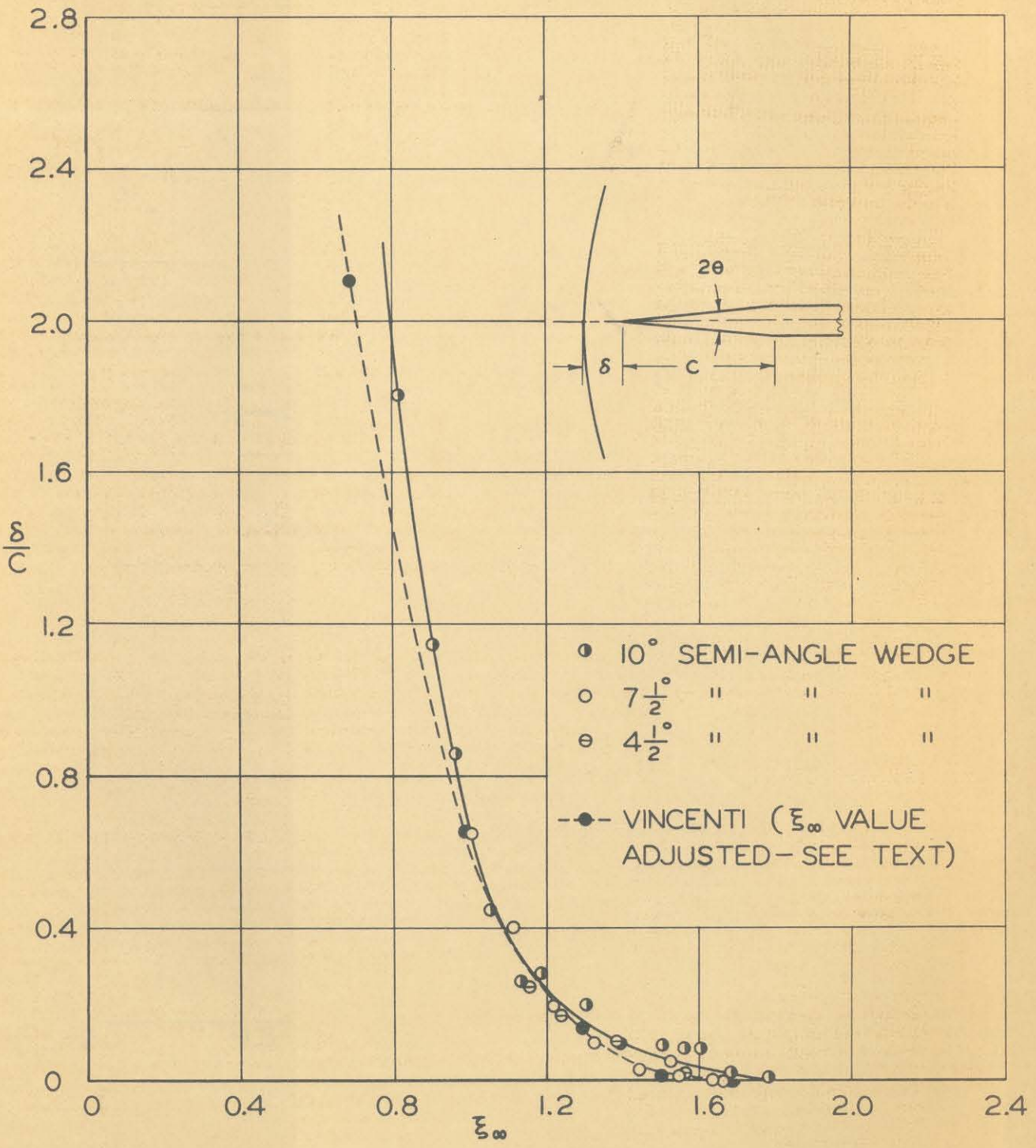

FIG. 21

EXPERIMENTAL REDUCED DRAG COEFFICIENT VERSUS REDUCED MACH NUMBER ON A WEDGE

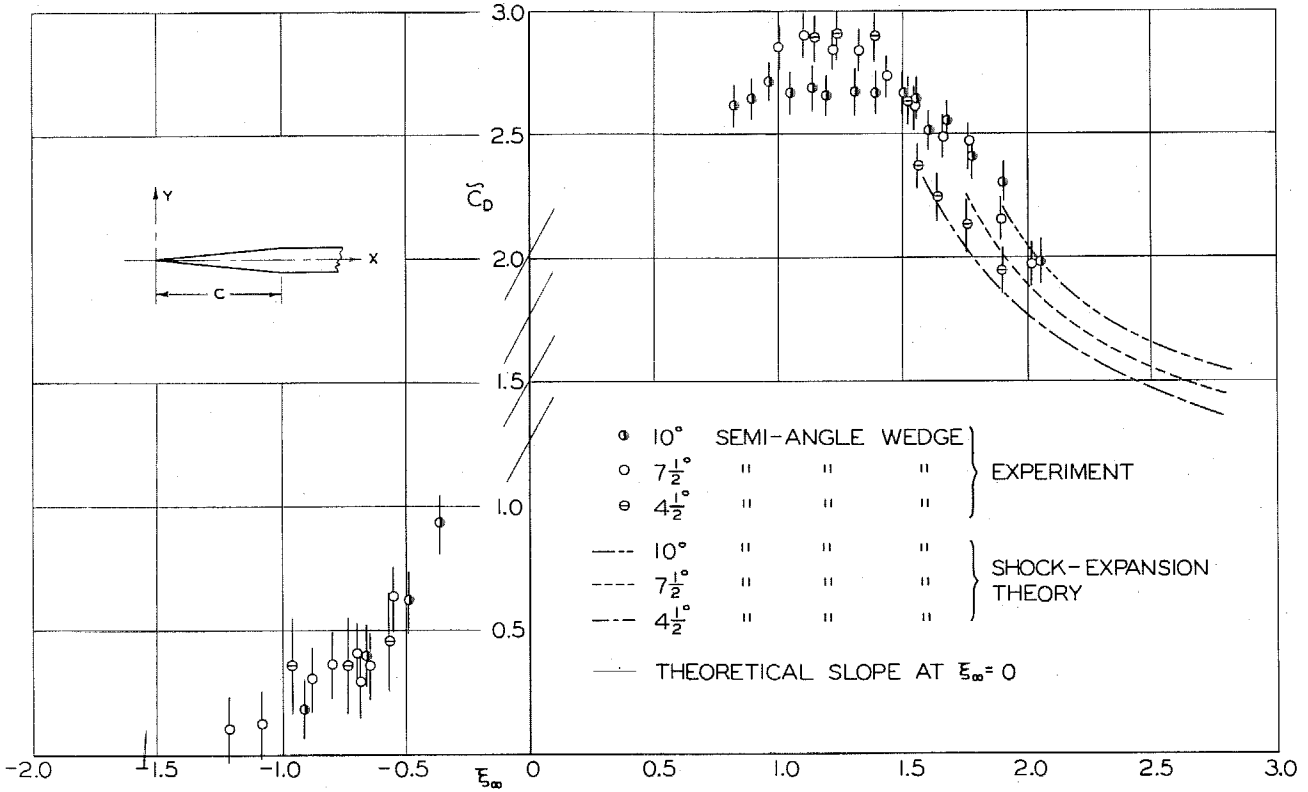

FIG. 22

DRAG COEFFICIENT VERSUS MACH NUMBER FOR $4\frac{1}{2}°, 7\frac{1}{2}°, 10°$ SEMI-ANGLE WEDGES

COMPARISON OF THEORY WITH EXPERIMENT

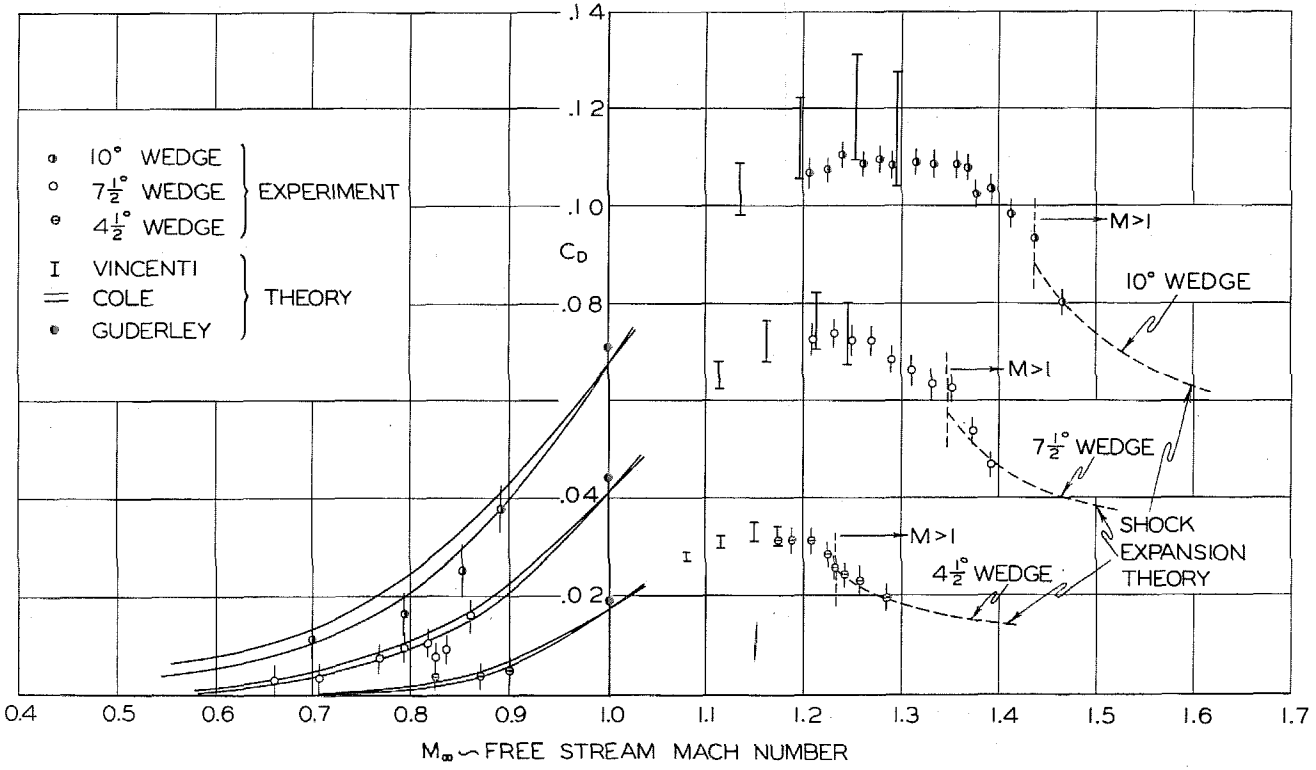

FIG. 23

26.6° SEMI-ANGLE WEDGE AT $M_\infty = 1.440$

CONSTANT MACH NUMBER CONTOURS

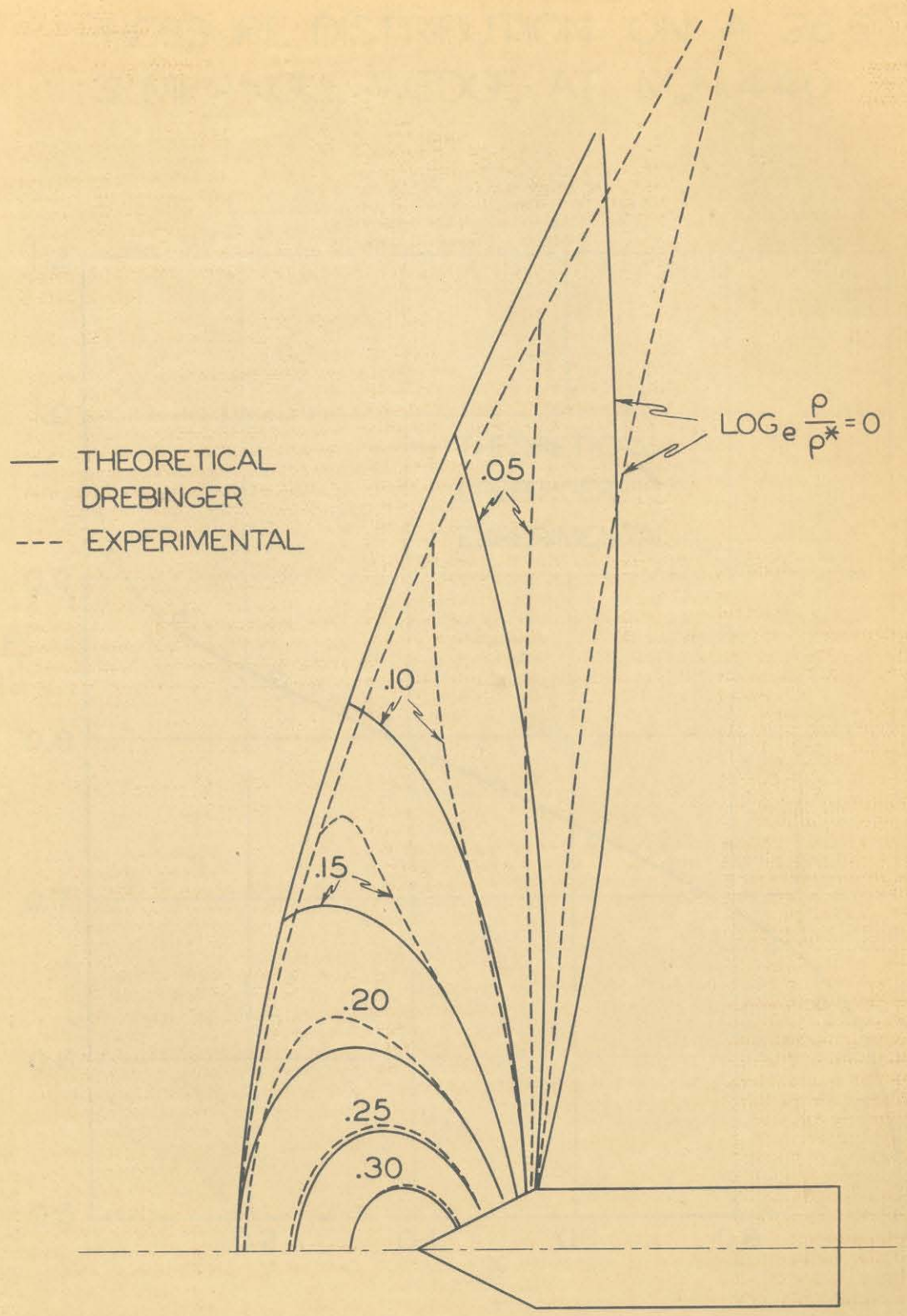

FIG. 24

PRESSURE DISTRIBUTION ON A 26.6° SEMI-ANGLE WEDGE AT M_∞=1.440

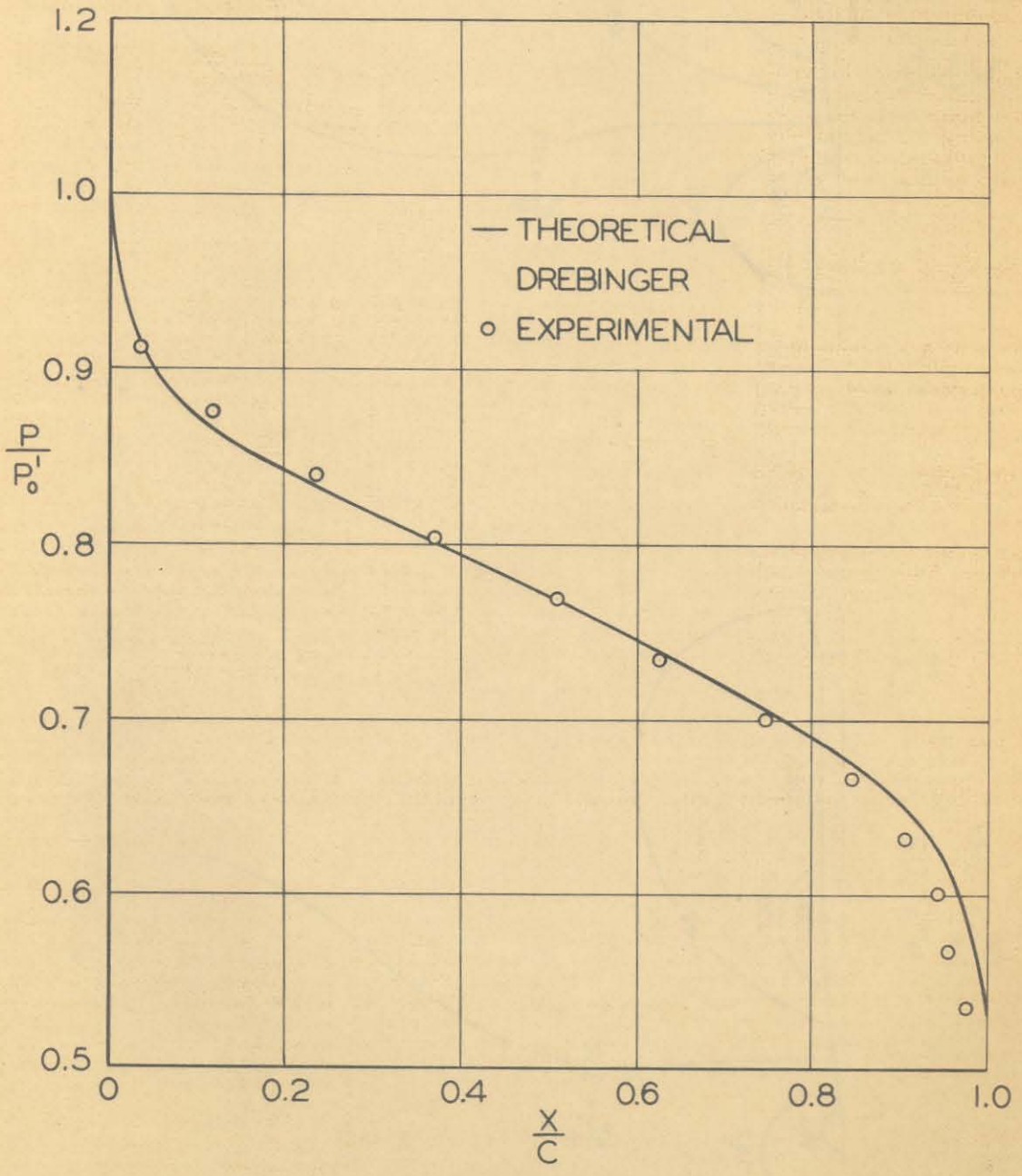

FIG. 25

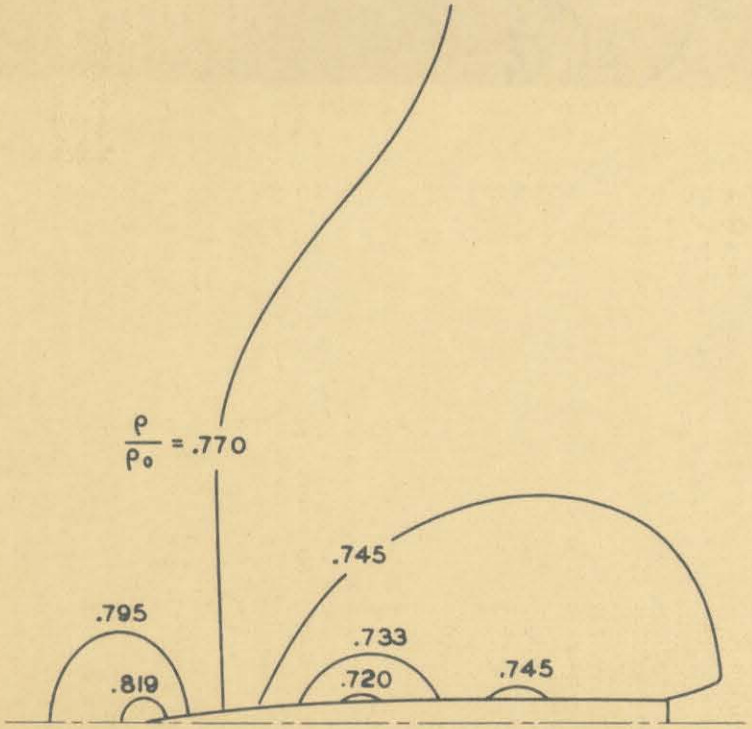

M_∞ = .718

$\frac{\rho_\infty}{\rho_0}$ = .783

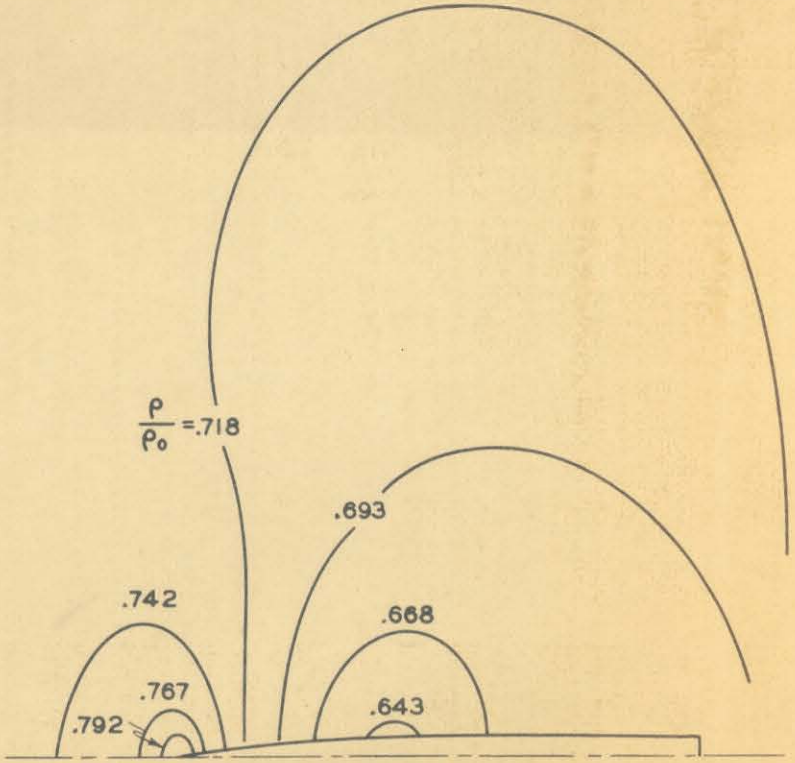

M_∞ = .819

$\frac{\rho_\infty}{\rho_0}$ = .730

8.8% CIRCULAR ARC SECTION

FIG. 26

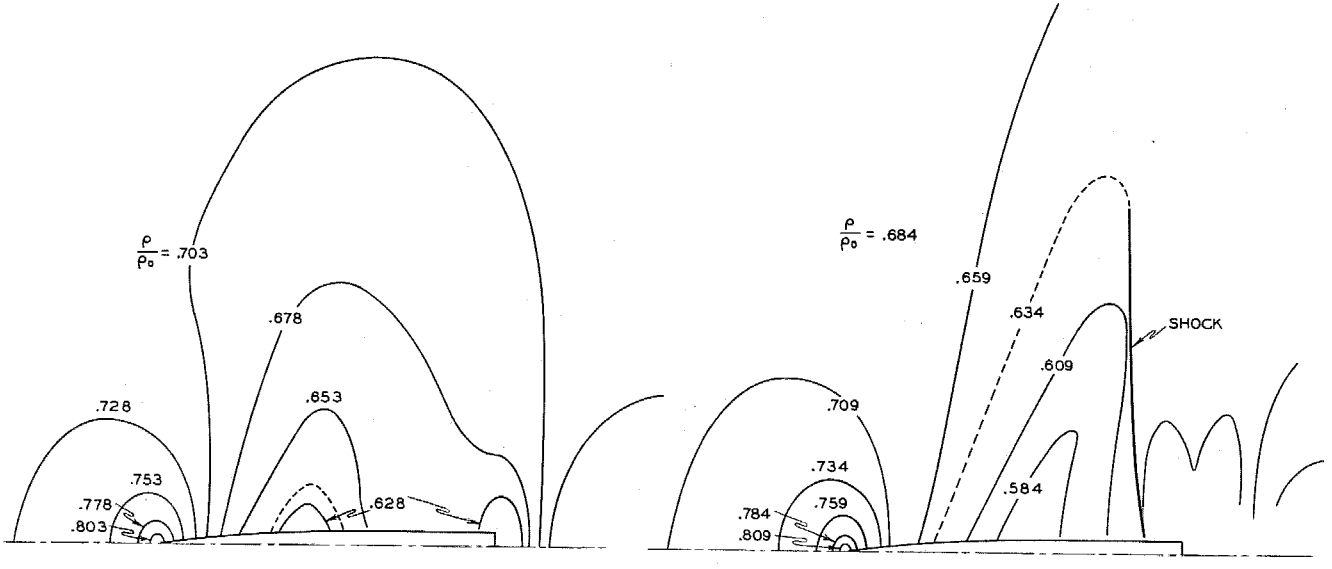

$M_\infty = .848$
$\frac{\rho_\infty}{\rho_0} = .715$

$M_\infty = .890$
$\frac{\rho_\infty}{\rho_0} = .696$

8.8% CIRCULAR ARC SECTION

FIG. 27

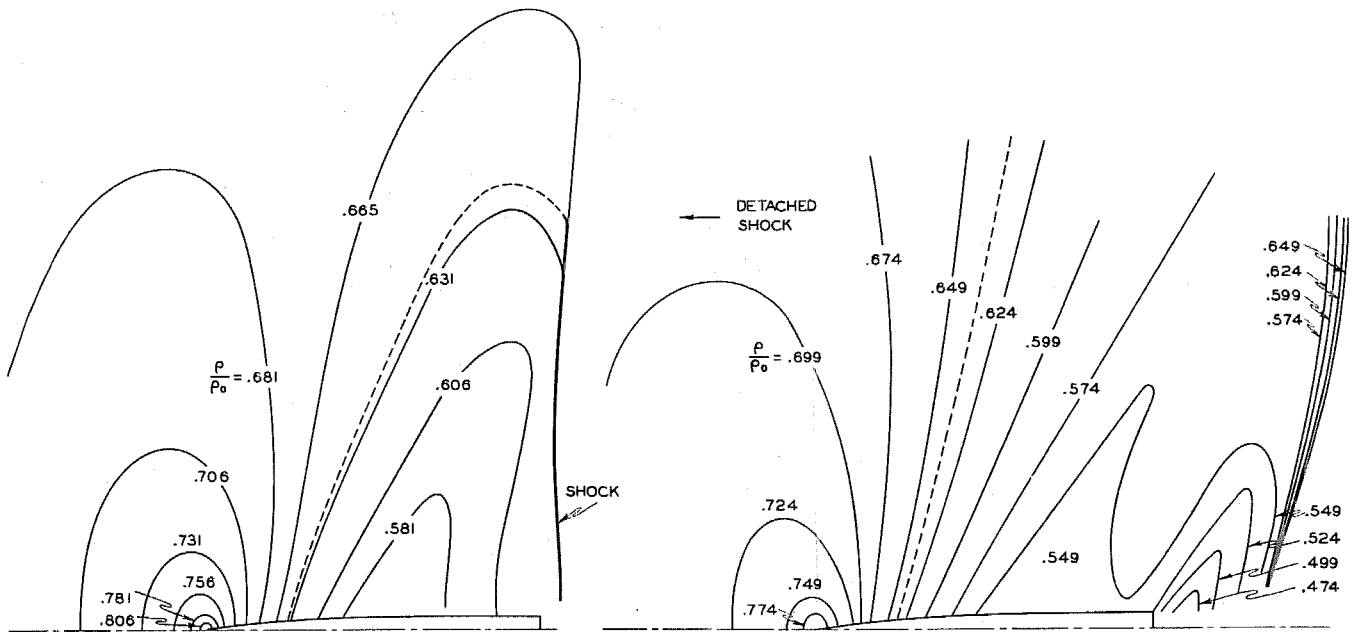

M_∞ = .935

$\frac{\rho_\infty}{\rho_0}$ = .668

M_∞ = 1.11

$\frac{\rho_\infty}{\rho_0}$ = .577

8.8% CIRCULAR ARC SECTION

FIG. 28

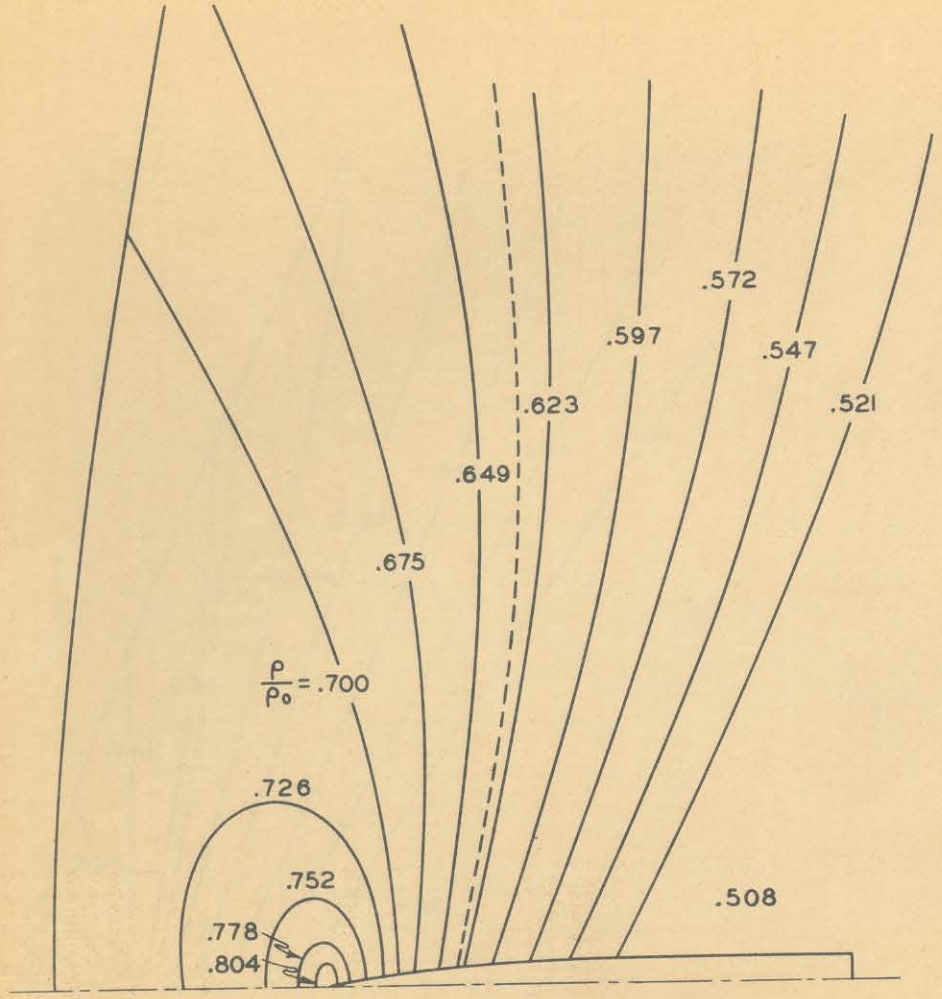

$M_\infty = 1.160$

$\frac{\rho_\infty}{\rho_0} = .551$

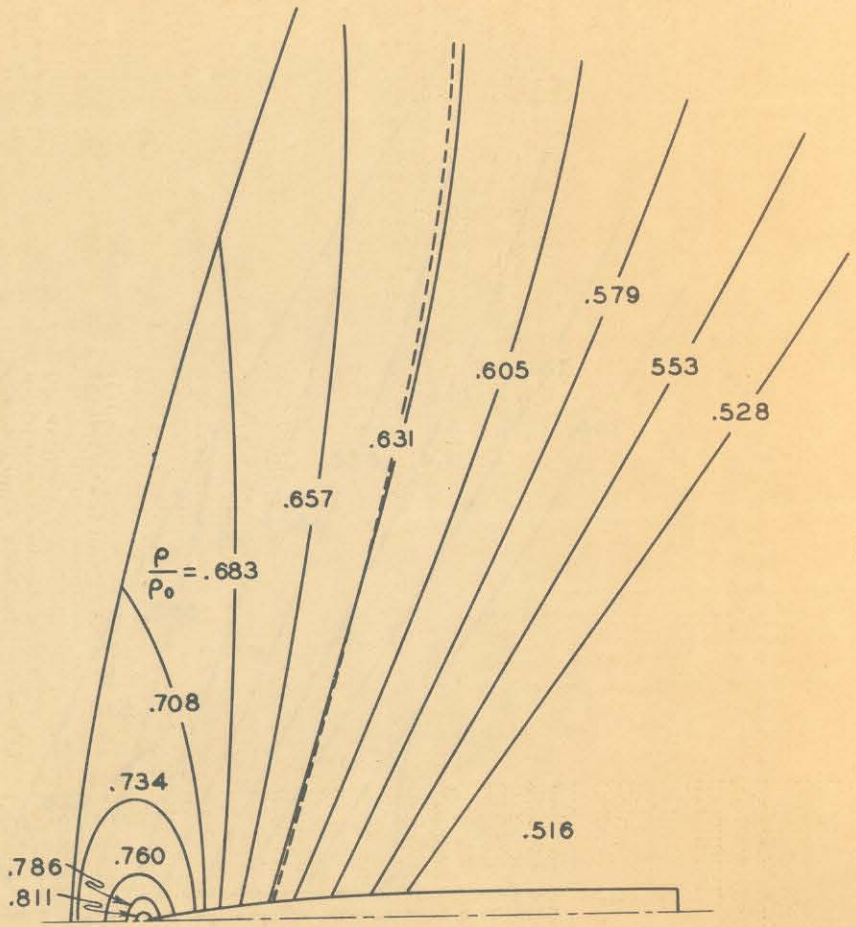

$M_\infty = 1.200$

$\frac{\rho_\infty}{\rho_0} = .531$

8.8% CIRCULAR ARC SECTION

FIG. 29

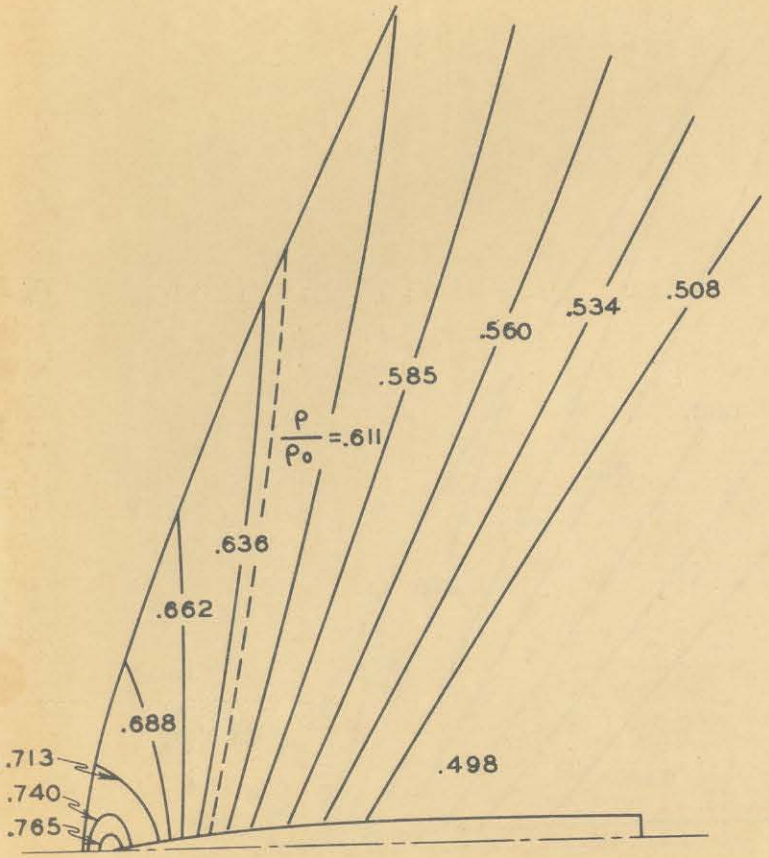

$M_\infty = 1.250$

$\frac{\rho_\infty}{\rho_0} = .507$

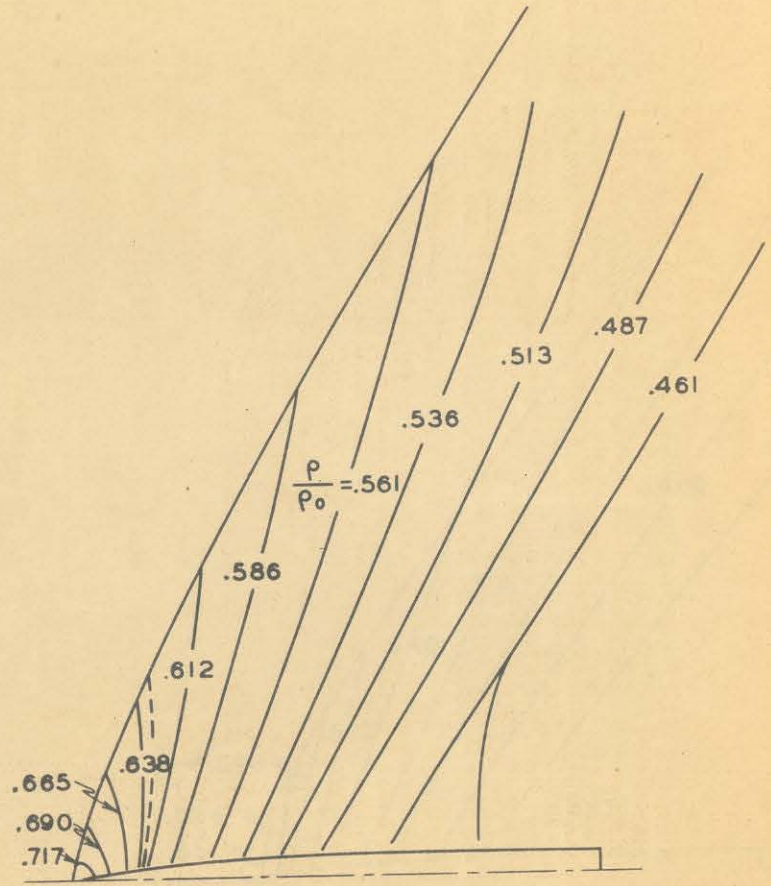

$M_\infty = 1.300$

$\frac{\rho_\infty}{\rho_0} = .483$

8.8% CIRCULAR ARC SECTION

FIG. 30

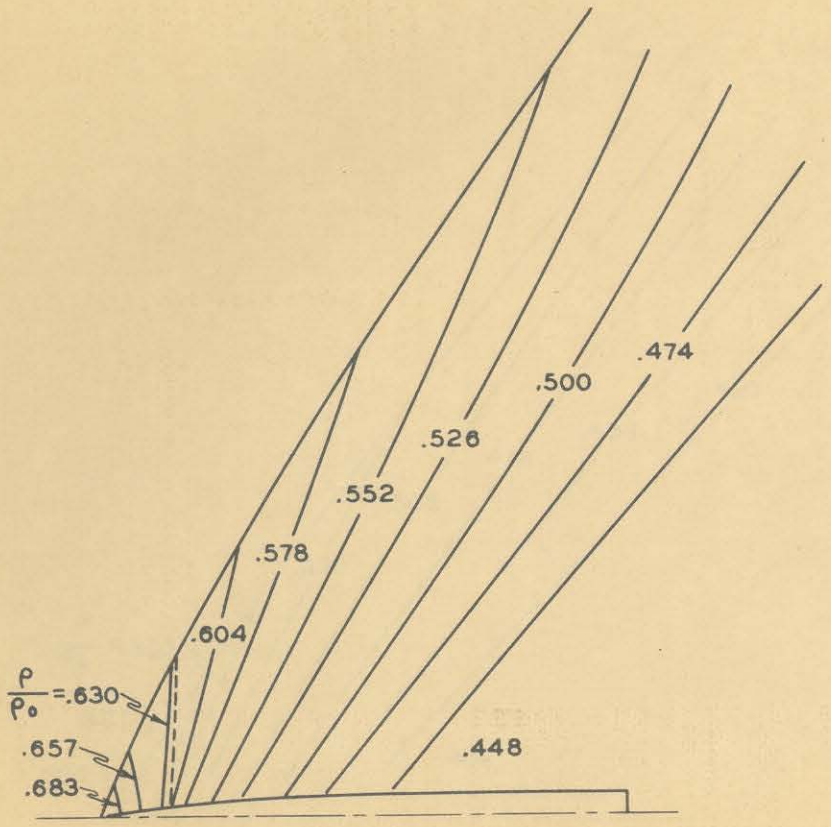

$M_\infty = 1.350$

$\frac{\rho_\infty}{\rho_0} = .460$

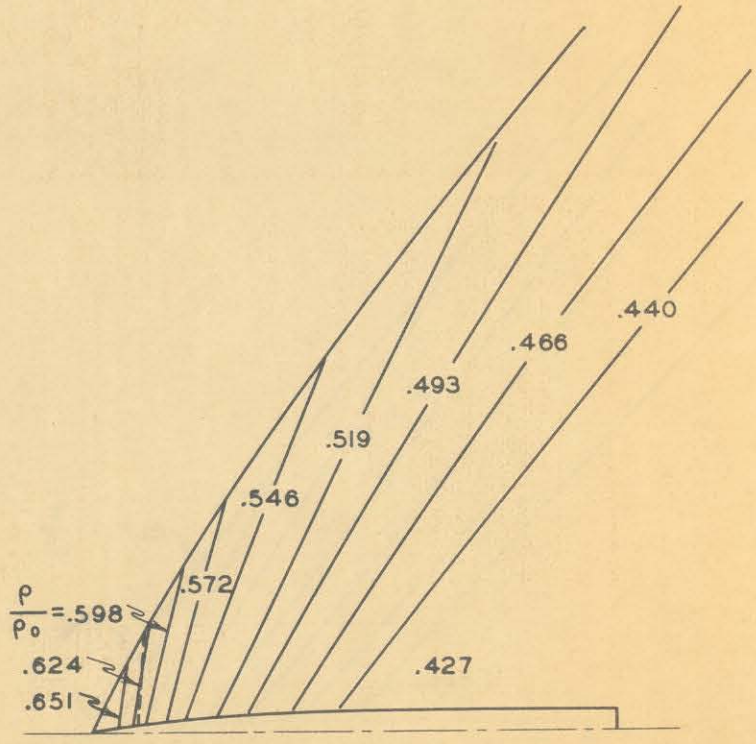

$M_\infty = 1.400$

$\frac{\rho_\infty}{\rho_0} = .437$

8.8% CIRCULAR ARC SECTION

FIG. 31

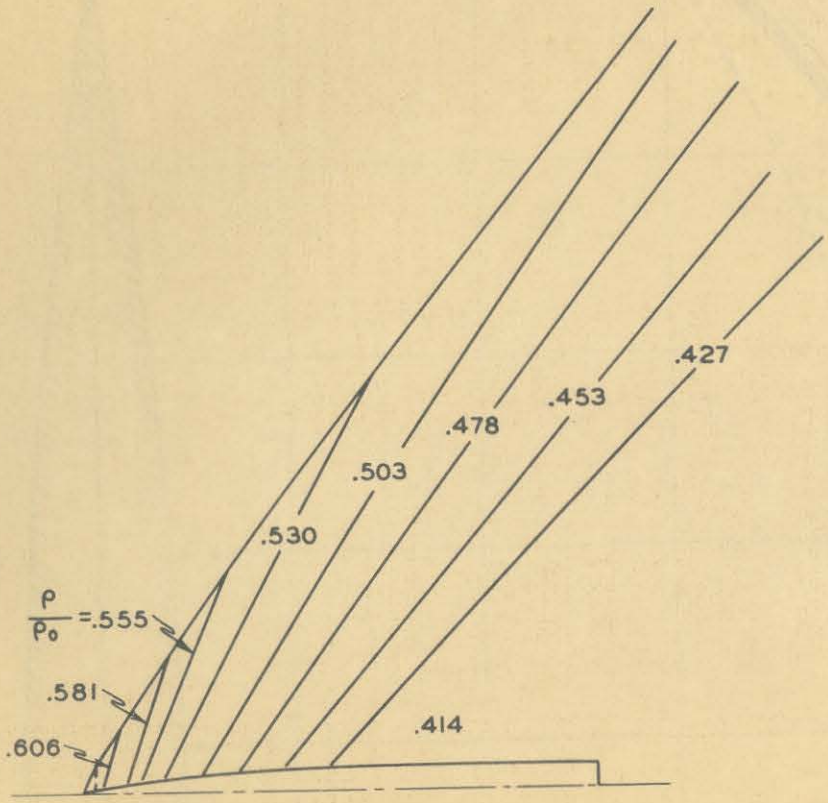

$M_\infty = 1.450$

$\frac{\rho_\infty}{\rho_0} = .416$

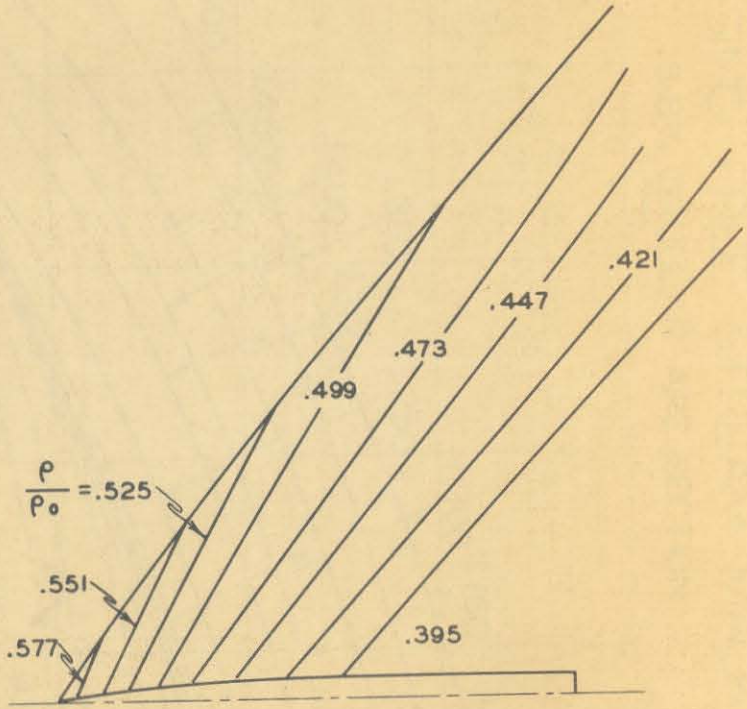

$M_\infty = 1.500$

$\frac{\rho_\infty}{\rho_0} = .395$

8.8% CIRCULAR ARC SECTION

FIG. 32

LOCAL MACH NUMBER VERSUS $\frac{x}{c}$ FOR INCREASING FREE STREAM MACH NUMBER

8.8% CIRCULAR ARC SECTION

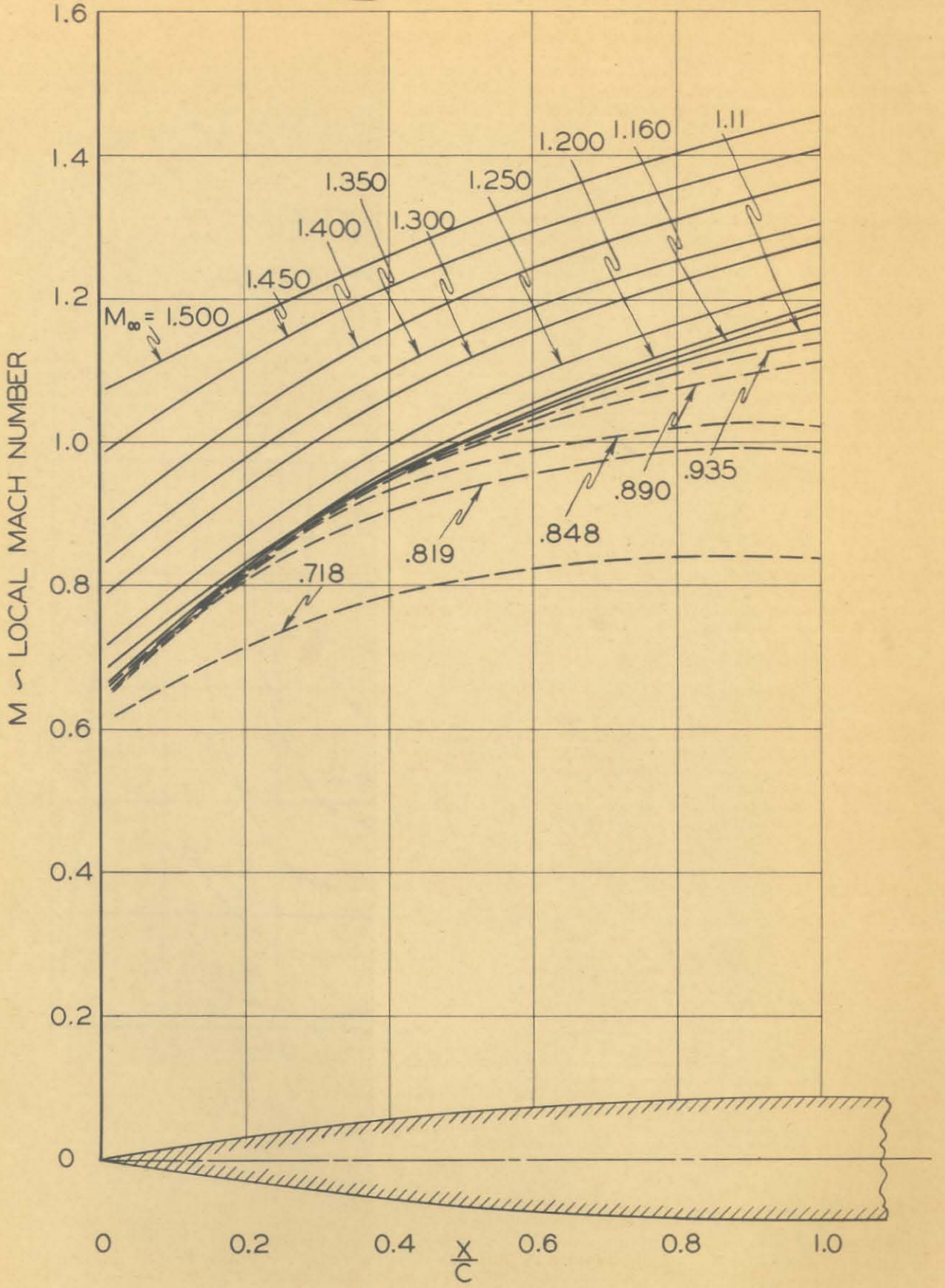

FIG. 33

REDUCED LOCAL MACH NUMBER DISTRIBUTIONS
VARIATION WITH REDUCED FREE STREAM MACH NUMBER

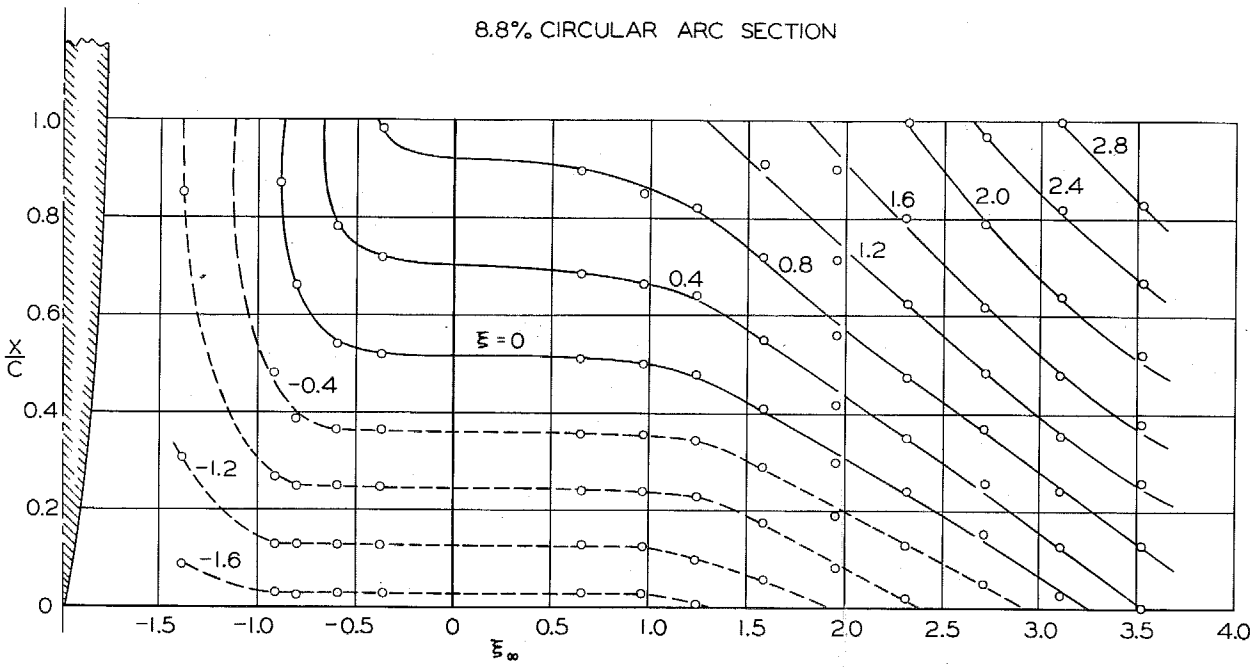

FIG. 34

PRESSURE DISTRIBUTIONS ON AN 8.8% CIRCULAR ARC SECTION

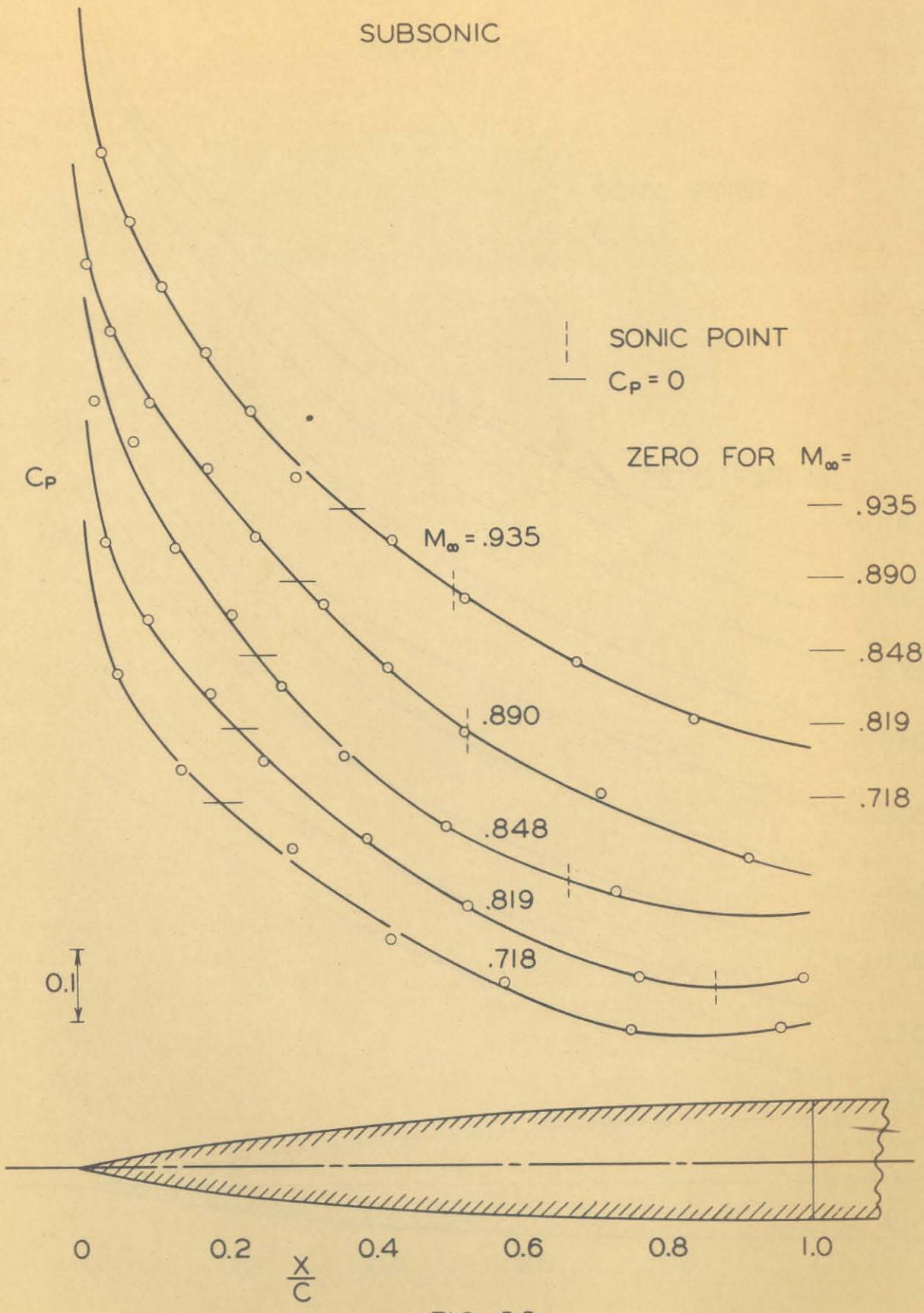

FIG. 35

PRESSURE DISTRIBUTIONS ON AN 8.8% CIRCULAR ARC SECTION

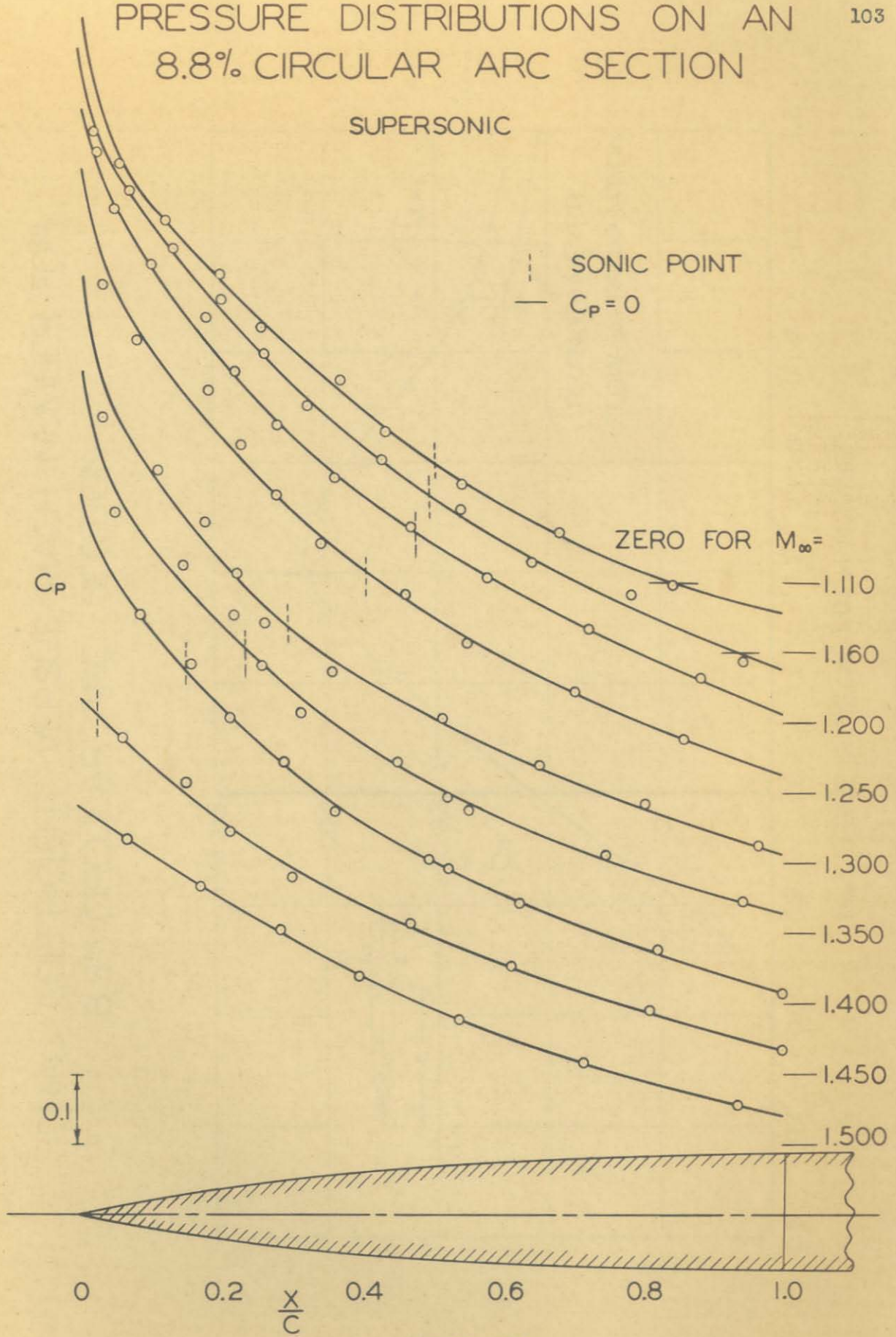

FIG. 36

DRAG COEFFICIENT VERSUS MACH NUMBER FOR 8.8% CIRCULAR ARC SECTION

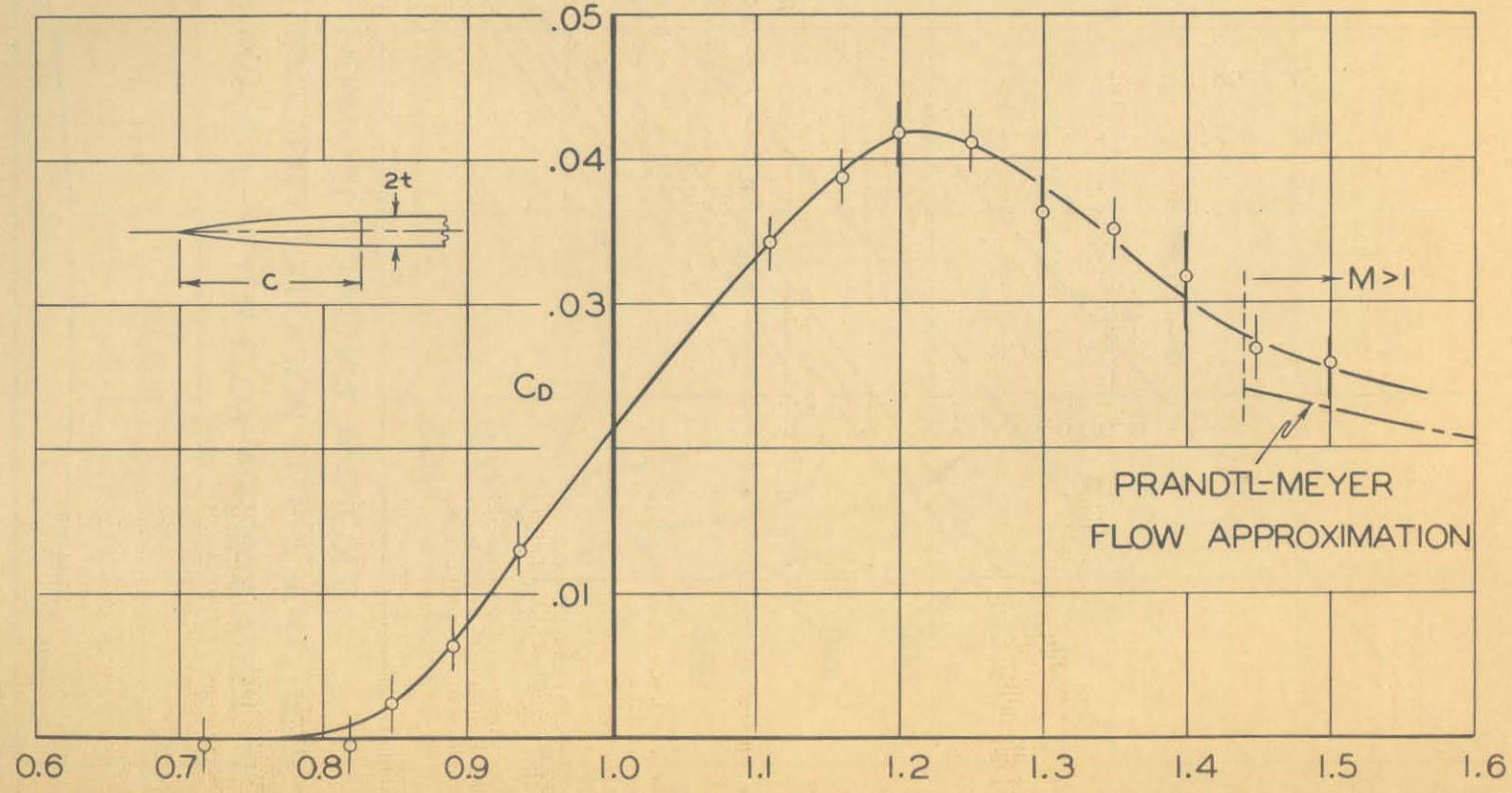

FIG. 37

LOCAL MACH NUMBER VERSUS $\frac{x}{c}$ FOR INCREASING FREE STREAM MACH NUMBER

12% BICONVEX CIRCULAR ARC AIRFOIL

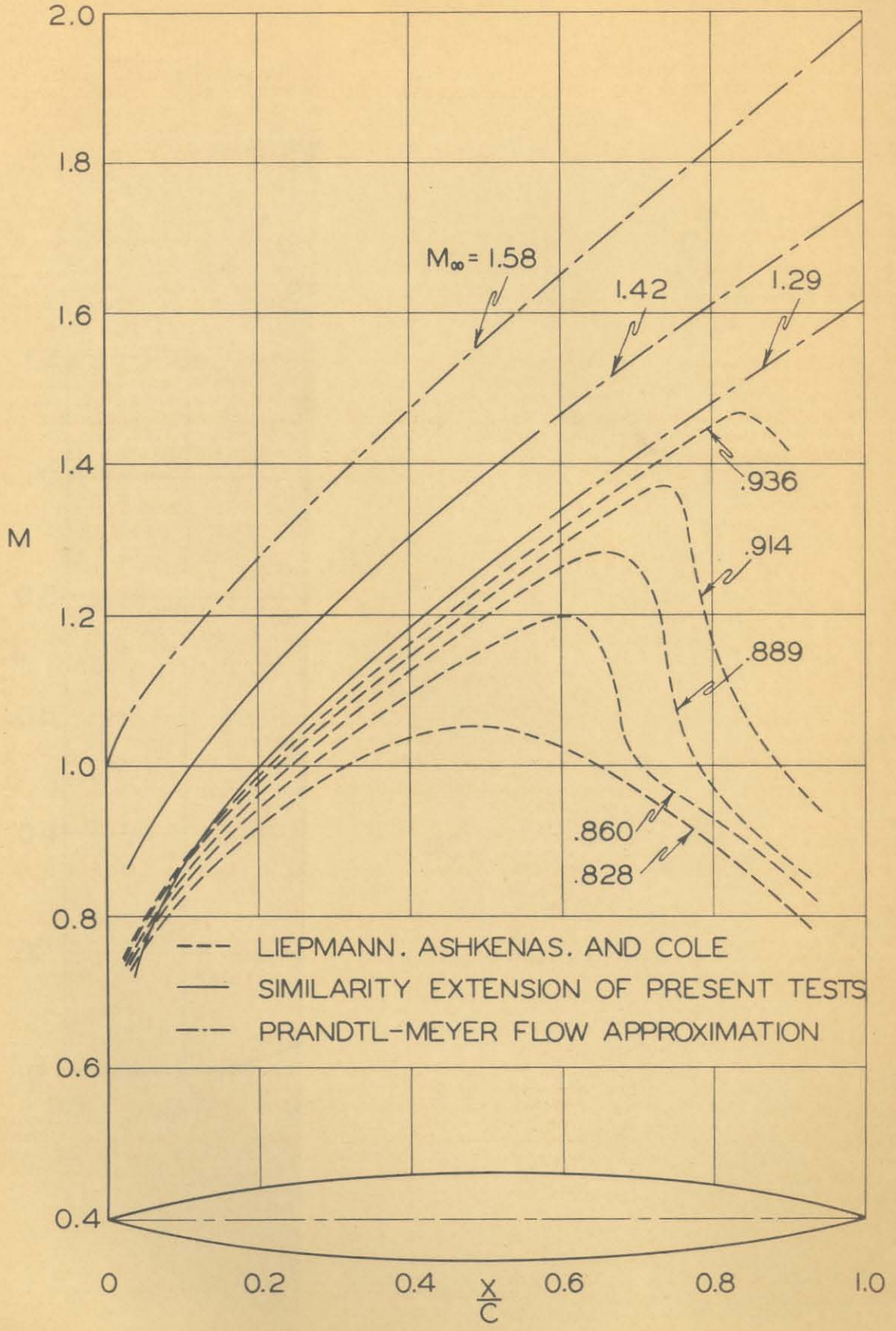

FIG. 38

DRAG COEFFICIENT VERSUS MACH NUMBER FOR 12% BICONVEX CIRCULAR ARC AIRFOIL

FROM DATA OF FIG. 38 ON BASIS OF CONSTANT MACH NUMBER DISTRIBUTION FROM $M_\infty = 0.96$ TO 1.20

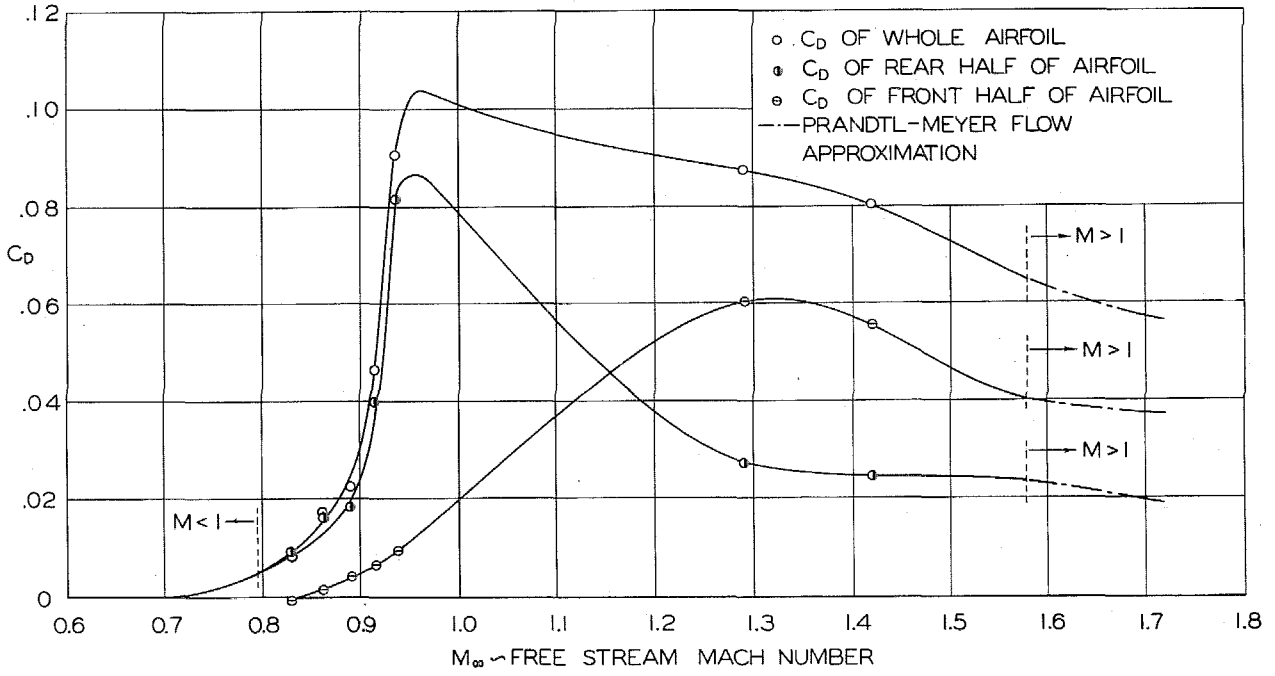

FIG. 39